Reconstruction of Acoustic Tissue Properties for Ultrasound Tissue Characterization

Natalia Ilyina

Dissertation presented in partial fulfilment of the requirements for the degree of Doctor in Biomedical Sciences

July 2017

KU Leuven
Biomedical Sciences Group
Faculty of Medicine
Department of Cardiovascular Sciences

KU LEUVEN

DOCTORAL SCHOOL
BIOMEDICAL SCIENCES

RECONSTRUCTION OF ACOUSTIC TISSUE PROPERTIES FOR ULTRASOUND TISSUE CHARACTERIZATION

Natalia ILYINA

Promoter:	Prof. dr. Jan D'hooge
Co-promoter:	Prof. dr. Koen Van Den Abeele
Co-promoter:	Dr. Jeroen Hermans
Chair:	Prof. dr. Werner Budts
Jury:	Prof. dr. Francois Varray
	Prof. dr. Massimo Mischi
	Dr. Filip Vanhavere
	Prof. dr. Johan Nuyts
	Prof. dr. Christ Glorieux
	Prof. dr. Dirk Vandermeulen

Dissertation presented in partial fulfilment of the requirements for the degree of Doctor in Biomedical Sciences

July 2017

To my family
for their love, support and encouragement

Aknowledgement

It seems it was only yesterday, when I first came to the Medical Research Center, where my PhD journey began. It has become a true adventure with its ups and downs, tears and joy, sleepless nights and vivid impressions. It has been a great experience and a serious challenge which I would not have coped with without the help of many people.

First of all, I would like to express my deepest gratitude to my supervisor, prof. Jan Dhooge, for giving me the chance to join his wonderful team and for guiding me through this intricate PhD path. Thank you for giving us the freedom to explore our own ideas and for backing us up when they did not succeed. Thank you for your soft critics, for your patience and encouragement, for the opportunity to present our work all over the world and for the numerous memorable moments, lab activities, summer and winter schools. I sincerely admire your approach and your passion for research. You have a true talent to explain complex terms in simple words and to find elegant solutions to seemingly unsolvable problems. This work would not have been possible without your guidance, and I am thankful for the opportunity to complete it.

I wish to thank my co-supervisors, Prof. Koen Van Den and Jeroen Hermans, for their assistance and contribution to this work. Koen, thank you for providing me with an experimental set-up that I used throughout this research, for sharing your expertise in acoustics and giving an extra touch to my manuscripts. Jeroen, thank you for your guidance and your input. I share every credit of this work with you. I owe sincere thanks to Emiliano DAgostino, SCK●CEN Academy and the whole RDC group headed by Filip Vanhavere for the invaluable opportunity to work on this project.

I wish to express my special thanks to the members of the examining committee, prof. Francois Varray, prof. Massimo Mischi, prof. Johan Nuyts, prof. Christ Glorieux, prof. Dirk Vandermeulen and Filip Vanhavere for the evaluation of this thesis and their constructive comments that allowed to improve the quality of this work. I would like to thank prof. Werner Budts for chairing the PhD Defence and prof. Maarten Naesens for managing the comments.

I would also like to thank Christel Huysmans for her patience and her help with countless administrative questions, Vincent Vandecaveye for his assistance with

Abstract

Reconstruction of acoustic tissue properties for ultrasound tissue characterization

Ultrasound imaging is an indispensable tool in medical diagnostics and offers several advantages over other imaging techniques. During last decades, ultrasound technology has achieved significant progress leading to improved image quality. However, conventional ultrasound envelope-detected images remain qualitative in nature and lack quantitative information on the tissue state and pathology. Therefore, there has been an increased interest in developing techniques that would enhance the diagnostic capabilities of ultrasound imaging. This field of study is referred to as ultrasound tissue characterization and aims to improve ultrasonic diagnostic capabilities by quantitatively measuring physical properties that can be linked to the tissue state.

Current state-of-the-art methods for ultrasound tissue characterization focus on one particular parameter, and attempt to estimate it directly from the backscattered RF signals. Other acoustic effects are being corrected for by means of additional measurements, or simply neglected. The significant number of underlying assumptions in this case makes application of the existing techniques difficult in clinical practice. Moreover, poor understanding of the interaction mechanisms of ultrasound with tissue remains the main challenge in ultrasound tissue characterization.

The aim of this thesis was to develop and validate a fundamentally different approach for reconstruction of the local acoustic properties, wherein the forward scattering problem is iteratively solved through computer simulations in order to match the synthetically generated ultrasound data to the experimentally observed ones. The advantage of such approach is that numerical modelling of the forward ultrasound wave propagation enables to study various ultrasound-tissue interactions as well as their combined effect in a controlled manner.

The developed approach was used for the reconstruction of an ultrasound attenuation coefficient and was extensively validated at increasing level of complexity of the considered problem. This work demonstrates the applicability

of the proposed model-based approach in the field of ultrasound tissue characterization and its ability to provide accurate attenuation estimates in various settings. Furthermore, a simulation tool was developed, that enables modelling of the forward ultrasound wave propagation and the spectral characteristics of the backscattered signals.

Reconstructie van akoestische weefseleigenschappen voor echografische weefsel karakterisering

Echografie is onmisbaar in de medische diagnostiek en heeft een aantal voordelen over andere beeldvormingstechnieken. In de laatste decennia heeft echografie een significante technologische vooruitgang gekend, wat leidde tot een verbetering van de beeldkwaliteit. Nochtans, conventionele echografische envelopgedetecteerde echobeelden hebben slechts een kwalitatief karakter en ontbreken kwantitatieve informatie over de weefselstatus en pathologie. Daarom is er een toegenomen interesse voor de ontwikkeling van technieken dat het diagnostisch vermogen van echografie verbetert. Dit vakgebied wordt echografische weefsel karakterisering genoemd en heeft als doel het echografische diagnostisch vermogen te verbeteren door middel van het kwantitatief meten van fysische eigenschappen geassocieerd met de weefselstatus.

In de huidige stand van de techniek op het gebied van weefsel karakterisering wordt er gefocust op een bepaalde parameter dat rechtstreeks wordt afgeleid van verstrooide radio-frequentie signalen. Bijkomstige akoestische effecten worden gecorrigeerd met behulp van additionele metingen. Een andere mogelijkheid is deze effecten buiten beschouwing te laten. Hierbij zijn er een groot aantal onderliggende assumpties dat de toepassing van de bestaande technieken in de klinische praktijk moeilijk maakt. Bovendien zijn de interactiemechanismen tussen de geluidsgolven en het weefsel nog onvoldoende gekend, wat een grote uitdaging blijft in echografische weefsel karakterisering.

Dit proefschrift had als doel het ontwikkeling en valideren van een fundamenteel verschillende benadering voor de reconstructie van lokale akoestische eigenschappen, waarbij het probleem van voorwaartse verstrooiing iteratief wordt verholpen door middel van computer simulaties dat synthetisch gegenereerde echografiedata koppelt aan experimenteel verkregen data. Het voordeel van deze benadering is dat de numerieke modellering van de voorwaartse geluidsgolf propagatie het mogelijk maakt de verscheidene interacties tussen de geluidsgolven en het weefsel te bestuderen, alsook het gecombineerde effect van beide op een gecontroleerde manier.

De ontwikkelde methodiek werd gebruikt voor de reconstructie van een geluidsgolf absorptie coefficient en werd uitvoerig gevalideerd tegen een stijgend niveau van complexiteit van het beschouwde probleem. Dit proefschrift toont aan dat

deze modelgebaseerde methode toepasbaar is in het gebied van echografische weefsel karakterisering en dat het mogelijk is om accurate absorptie schattingen te verkrijgen in verschillende settingen. Overigens werd een simulatieapplicatie ontwikkeld dat het mogelijk maakt om de voorwaartse geluidsgolf propagatie en de spectrale karakteristieken van de verstrooide signalen te modelleren.

Contents

List of Abbreviations

1-D	One-dimensional
2-D	Two-dimensional
3-D	Three-dimensional
ASA	Angular spectrum approach
FFT	Fast Fourier transform
GPU	Graphic processing unit
PMMA	Poly(methyl methacrylate), acrylic glass
PVA	Poly(vinyl alcohol)
RF	Radio-frequency
RMS	Root mean square
ROI	Region of interest
SDM	Spectral-difference method
SNR	Signal to noise ratio
SSM	Spectral-shift method
TGC	Time-gain compensation
UTC	Ultrasound tissue characterization

List of Symbols

α	Attenuation coefficient
γ	Inhomogeneity coefficient
$\delta(\boldsymbol{r} - \boldsymbol{r_0})$	Delta-function
ϵ	Correction coefficient
κ	Compressibility
λ	Wavelength
ξ	Sampling factor
ρ	Density
σ	Backscatter coefficient
ϕ	Velocity potential
ω	Angular frequency
∇	Gradient operator
J_0	Bessel function of first kind and zero order
$\mathcal{F}, \mathcal{F}^{-1}$	Forward and inverse Fourier transform
$\mathcal{P}$	Power spectrum
c_γ	Correlation coefficient
$\bar{n}$	Correlation coefficient
A	Angular spectrum
a_{eff}	Effective scatterer size
c	Speed of sound
D	Spectral distance
F	Form-factor

f	Frequency
$G(\boldsymbol{r}|\boldsymbol{r_0})$	Free-space Green's function
h	Impulse response
H	Transfer function
k	Wavenumber
k_x, k_y, k_z	Coordinates in the spatial-frequency space
p	Pressure
$\boldsymbol{r} = (x, y, z)$	Spatial coordinates in Cartesian space
t	Time
S	Fourier spectrum
V	Scattering volume
V_s	Effective scatterer volume
v_n	Normal velocity
w	Electro-mechanical transfer function of a transducer
Z	Acoustic impedance

4

Chapter 1

Introduction

1.1 Ultrasound imaging

The first practical application of ultrasound dates back to 1914 when the first working sonar system was designed and built for underwater navigation and ranging. The potential of ultrasound in medicine was realized in early 1940's when several groups of investigators around the world started exploring the diagnostic capabilities of ultrasound. However, because of a number of factors limiting the application of ultrasound imaging in practice, it was not until the 1970's that it became an accepted diagnostic modality. After the gray-scale ultrasonography was introduced followed by the development of real-time scanning systems, ultrasound has rapidly became a routine imaging modality. Unlike other imaging modalities, ultrasound does not produce ionizing radiation, it is compact, portable, relatively inexpensive and allows real-time imaging. Due to these unique characteristics, ultrasound has evolved into an indispensable tool in medical diagnostics and remains an active and rapidly-advancing area of research.

Nowadays, applications of medical ultrasound include but are not limited to diagnostics of the heart, blood vessels, abdominal organs, breast, eyes, thyroid, muscles and skin; prenatal diagnosis; functional measurements of the blood flow (color Doppler) and tissue stiffness (elastography). Moreover, ultrasound is often used as a guiding tool for interventional procedures and as a therapeutic tool (for heating and ablation).

Current research focuses on reduction in size of the ultrasound machines and transducer design, harmonic and multidimensional imaging, improvements in image acquisition rate and quality, advances in contrast imaging and ultrasonic

drug delivery, development of high frequency devices for imaging and tissue ablation, and, finally, on developing means to extract new diagnostic information that will be further discussed in this thesis.

1.1.1 Physical principles

Ultrasound is the name given to a sound wave of frequency exceeding the human auditory band (20 Hz - 20 kHz). In clinical ultrasound, frequencies in the range of 2 to 20 MHz and above are typically used. Ultrasound waves are generated and detected by piezoelectric crystals embedded within a transducer that vibrate in response to an applied electric current and conversely, are able to convert the mechanical motion into an electrical voltage. Propagation of the vibrational energy through a medium causes a local displacement of medium particles. In a liquid medium, ultrasound propagates as a longitudinal wave, i.e. along the direction of particle movement, and consists of successive zones of compression (high pressure region) and rarefaction (low pressure region) (Fig. 1.1).

As a wave process, ultrasound is characterized by its wavelength(λ), propagation speed (c) and frequency (f), which are related through the following expression:

$$\lambda = \frac{c}{f}.$$ (1.1)

The speed at which ultrasound wave travels depends on the physical properties of the medium, such as density and elasticity. Since the difference in the propagation speed among soft tissues is rather small, the wavelength, and hence the resolution of an ultrasound system, are mainly determined by the transmit frequency. The nominal frequency of the transducer is determined by the thickness of piezoelectric crystals, and only a limited band of frequencies can be generated and detected, which is referred to as bandwidth. Higher frequencies allow distinction between smaller features. However, the maximum usable frequency is limited by other properties of the medium that will be discussed below.

During its propagation, an ultrasound wave will encounter different types of tissue. The point at which the tissue type changes is where there is a change in acoustic impedance, defined as the product of the medium density and the speed of sound:

$$Z = \rho c.$$ (1.2)
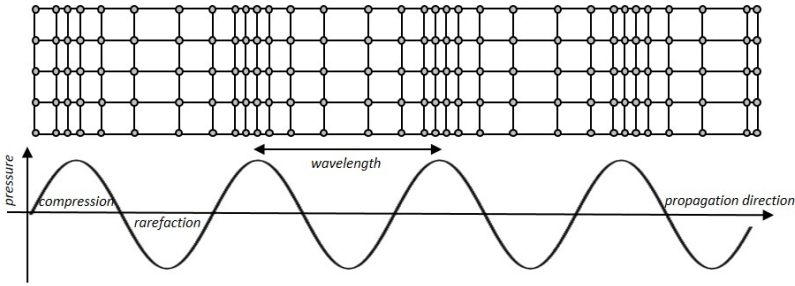
Figure 1.1: *Schematic view of particle displacement during longitudinal wave propagation, where the movement of the particles is along the direction of wave propagation.*

When the interface between two media with different acoustic impedances is met, part of the ultrasound wave is *reflected* back to the source, while the remainder travels on through the body, i.e. is *transmitted* (Fig. 1.2). When the propagation speed is different in the two media, the transmitted wave travels under an altered angle, i.e. is refracted. These phenomena are governed by the Snell's law:

$$\frac{sin\theta_i}{c_1} = \frac{sin\theta_r}{c_1} = \frac{sin\theta_t}{c_2}, \tag{1.3}$$

where θ_i, θ_r and θ_t are the angles of incidence, reflection and transmission, respectively.

The fraction of the reflected energy as well as the propagation direction of the refracted wave depends on the mismatch in acoustic impedances of the media and the direction of the incident wave. The greater the mismatch in acoustic impedance, the more energy is reflected at the interface. The reflected signals are referred to as specular reflections.

Another type of reflections occurs when the ultrasound wave encounters (irregular) interfaces smaller than the incident wavelength. These interfaces are local density and compressibility inhomogeneities inside the medium that are referred to as scatterers, and the above phenomenon is referred to as scatter reflections (or simply *scattering*). Scatterers retransmit the energy in different directions depending on the shape of the scatterer and its size relative to the ultrasound wavelength. Scatterers retransmitting energy uniformly in all directions are referred to as point scatterers. The portion of the scattered energy that is directed back to the source is referred to as *backscatter*. Constructive and destructive interference between scatterers forms the so-called ultrasound speckle - a granular pattern seen in ultrasound images.
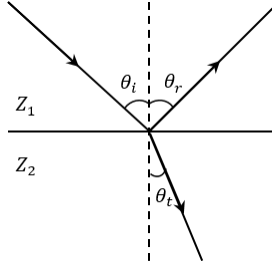
Figure 1.2: *Illustration of the reflection and refraction at the interface between two media with different impedances.*
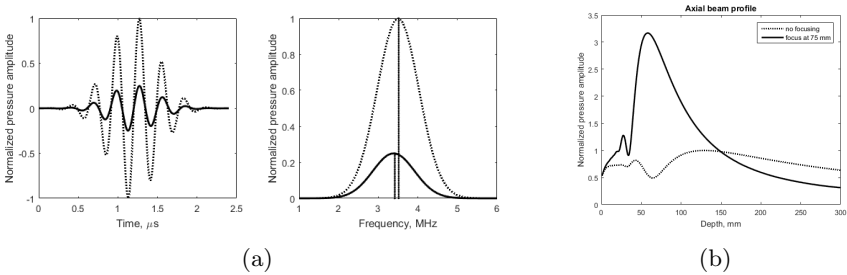
Figure 1.3: *Example of an attenuated waveform and its Fourier spectrum (a) and a diffration profile of an unfocused and focused transducers (b).*

Due to the above described phenomena, the energy of an ultrasound wave will be reduced during its propagation. However, an even greater fraction of ultrasound energy will be lost due to its conversion into heat. This effect is referred to as *absorption* and is caused by tissue viscosity. A collective term that describes the loss of ultrasonic energy is referred to as *attenuation*. This effect is frequency-dependent and causes a down-shift in the central frequency of the ultrasound wave. A good approximation for the frequency dependence of attenuation for most soft tissues is given by a power-law model:

$$\alpha = \alpha_0 |f|^n, \tag{1.4}$$

where the power n in soft tissue is typically between 0 and 2. Attenuation limits the penetration of ultrasonic waves and hence, the maximum depth at which tissues can be imaged. Because attenuation increases with frequency, ultrasonic waves of high frequencies have a shorter depth of penetration. Therefore, there is an inherent trade-off between the spatial resolution (which improves with increasing frequency) and penetration in ultrasonic imaging.
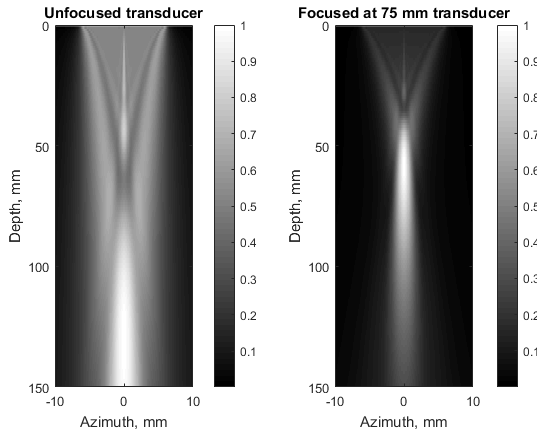
Figure 1.4: *Normalized transmit beam profiles of an unfocused (left) and focused (right) single-element transducer. Focusing is achieved through the spherical curvature of the transducer element.*

When absorption is present in tissue, the propagation velocity varies with frequency. This effect is known as *dispersion*. In media with strong absorption, the dispersion significantly alters the shape of the waveform and intensifies with propagation depth. However, in soft tissue, the effect of dispersion is rather small, and hence, a constant propagation speed is often assumed over the considered frequency range [1]. The shape of the waveform is also affected by *nonlinear distortion*. This effect arises due to the dependence of the sound velocity on tissue density: as the compression regions of the waveform travel faster than refraction regions, part of the waveform becomes steeper as the wave propagates. In the frequency domain nonlinear propagation results in the generation of higher harmonics. The amount of nonlinear distortion that occurs depends on the nature of the propagating medium. This effect is cumulative and is significant for high-amplitude waves but for waves with small amplitude a linear approximation is often made.

Until now, propagation of a single ultrasonic wave was discussed. However, the energy generated by an ultrasonic transducer does not originate from a single point but from a collection of many points (sources) along the surface of the piezoelectric element. Each point source generates a spherical wave front that spreads from the transducer surface. Together, these waves form an ultrasonic beam and the effect describing the spreading of the beam and interference of its individual components is referred to as *diffraction*. Ultrasound beam spreading also contributes to the overall acoustic energy loss during beam propagation. The diffraction is strongly dependent on the shape of the source and its size

9
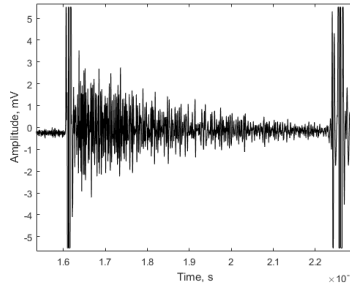
Figure 1.5: *Example of an RF signal recorded in water from an object with a homogeneous distribution of scatters. The exponential amplitude decay seen in the figure is due to attenuation. Strong reflections on the "water-object" and "object-water" interfaces are due to the impedance mismatch between these two media.*

relative to the ultrasound wavelength. For the purpose of obtaining higher lateral resolution, narrow ultrasound beams are preferable, and therefore, focused transducers are typically used in ultrasound imaging (Fig. 1.4). Focusing can be achieved geometrically through use of acoustic lenses or curved piezoelectric elements. For transducers composed of several piezoelectric elements (as will be discussed later) focusing can be done digitally by properly timing the elements during the transmit and receive events. During focusing, the acoustic energy is concentrated inside of a small area around the focal zone which yields increased intensity at the point of focus (Fig. 1.3b).

1.1.2 Pulse-echo principle

The name "pulse-echo" refers to a mode of signal acquisition, in which reflected ultrasound signals (echoes) are detected by the same transducer that was used for signal transmission. Ultrasound imaging instruments typically transmit short bursts of energy, commonly termed pulses. Short pulses are necessary to achieve good resolution in axial (beam) direction. After transmission, the piezoelectric-electric element of the transducer starts "listening" to the returning echoes. Upon receiving the reflected signals, transducer elements undergo a mechanical deformation which is converted to electrical signals that are digitized and stored for further analysis. The reflected ultrasound signals arrive at the transducer some time after the original signal was transmitted. This delay is equal to the time it takes an ultrasound signal to reach the scatterer or organ boundary and to return to the transducer site. Therefore, when the speed of propagation (c) is nearly constant, the depth of a scatterer/reflector

(d) can easily be calculated as:

$$d = \frac{ct}{2}, \tag{1.5}$$

where t is the time delay between the echo and signal transmission. The echoes detected by the transducer form the so-called radio-frequency (RF) signal (since the frequencies involved correspond to the frequencies of radio waves) (Fig. 1.5). By sequentially transmitting an receiving signals in different directions and combining the obtained RF lines, an ultrasound image can be created that displays internal body structures.

1.1.3 Data acquisition

Ultrasound data acquisition can be performed in different ways. The three general acquisition modes are the A- (Amplitude), M- (Motion) and B- (Brightness) modes (Fig. 1.6). While A-mode simply displays the raw RF signal over time (Fig. 1.6a), in M-mode, the RF signal is recorded successively over time in order to reconstruct a 2-D image that is used for analysis of moving organs. In this case, amplitudes of RF signals are encoded to grey scales and are displayed as pixels intensities (Fig. 1.6b). The B-mode imaging is most commonly used in clinical practice and consists of a combination of A-mode measurements performed along different directions. These directions typically form a sector in a plane of the body, and hence, B-mode images depict cross sections of the examined tissue structures. Just as during M-mode acquisition, the amplitude of the signals is converted to grey value, and the resulting image represents a 2-D grey-scale of the reflected intensity displayed as brightness (Fig. 1.6c).

2-D images can be produced by mechanically moving a single-element transducer across a scan plane. However, in modern ultrasound imaging, transducers are used that consist of multiple elements which can be excited independently allowing electronic scanning (Fig. 1.7). Most common in medical imaging are the linear-array and the phased-array transducers that consist of a 1-D array of crystals. Linear array transducers move the ultrasonic beam by sequentially firing subgroups of elements, and the resulting scan lines are parallel to each other. Alternatively, the aperture of a linear array can be curved to create a scan of a trapezoidal shape. Linear array transducers have a relatively broad aperture and are typically used for applications where the acoustic window is large, i.e. abdominal, vascular and obstetrics examinations. Phased array transducers have a smaller footprint enabling imaging within a small acoustic window (e.g.cardiology). By manipulating the timing of excitation of individual elements captured by the individual elements before summing, both electronic

| (a) A-mode | (b) M-mode | (c) B-mode |
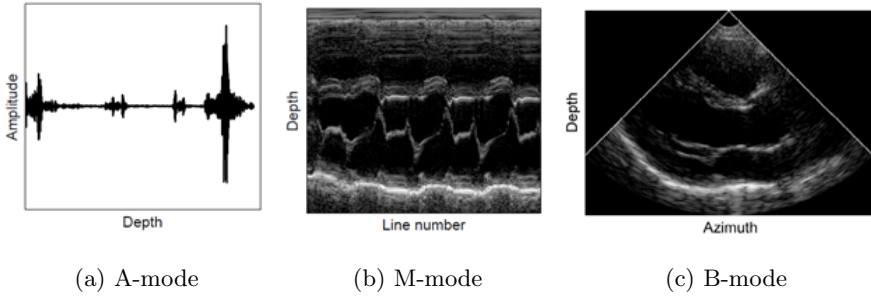
Figure 1.6: *Example images of (a) A-mode, (b) M-mode and (c) B-mode. Reproduced with permission from [2].*
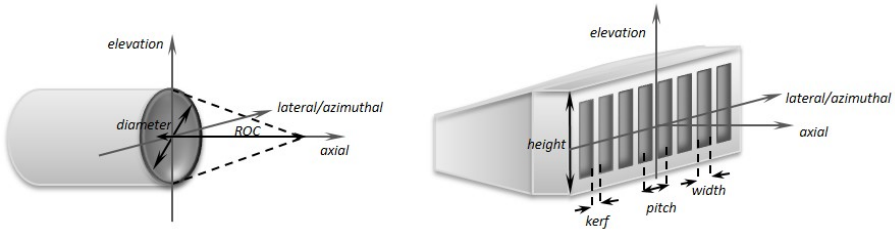
Figure 1.7: *Schematic illustration of ultrasonic transducers: single-element (left) and 1-D array transducer (right) and their geometrical description.*

focusing and steering of the beam can be achieved. Similarly, the transducer can be focused on receive by applying time delays on the reflected signals. By adjusting the delays of the received signals over time, dynamic receive focusing can be achieved, which significantly improves the lateral resolution. Phased array transducers produce a sector image. The number of lines in the sector and the line density can be adjusted depending on the application. However, since the scan lines diverge with depth, the scan line density is not uniform throughout the field of view.

1.1.4   Image formation

Reconstruction of a B-mode image from an acquired set of RF signals consists of several processing steps. First, the signals are amplified to compensate for tissue attenuation using the so-called *time-gain compensation*. Due to attenuation, echoes returning from deeper tissue regions are weaker than those arising close to the aperture. The attenuation is compensated for by increasing the
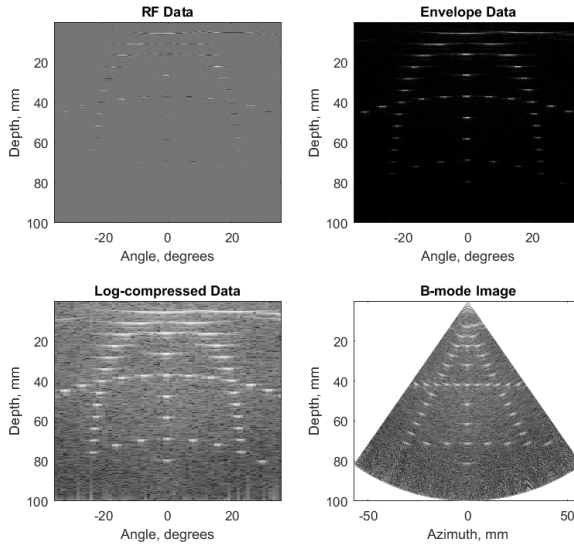
Figure 1.8: *Illustration of the processing steps for the formation of a sector B-mode image.*

amplification gain with increasing depth of the returning echoes. In this way, a balanced in brightness image is produced. As a next step, the signals undergo *filtering* to reduce noise outside frequencies of interest. Further, the *envelope* of RF signals is detected to remove high frequency information, which is typically done by means of a Hilbert transformation. The resulting signals are *log-compressed* to fit the dynamic range used for display. Finally, for sectorial acquisitions, *scan-conversion* is performed to transform the data from the polar space to Cartesian coordinates, which is done by means of interpolation (Fig. 1.8). The time required for an acquisition of one image, i.e. frame, is so small ($\sim$30 ms) that ultrasound imaging can be performed in real time. The temporal resolution can be further improved by decreasing the imaging depth or line density or by employing advanced acquisition techniques, which are constantly being developed.

1.2 Ultrasound tissue characterization

Conventional ultrasound B-mode imaging is extensively used in clinical practice in various applications. Ultrasound gray-scale images allow analysis of

	Speed of sound	Attenuation coefficient	Backscatter coefficient	Nonlinear parameter
Liver	[3–6]	[6–14]	[11, 13]	[3, 15]
Kidney		[16, 17]	[15]	
Breast	[18, 19]	[18, 20, 21]	[20, 22, 23]	
Myocardium	[24–26]	[27–30]	[29, 31]	
Aorta	[32]	[32]	[33]	
Eye		[34, 35]	[36]	
Lymph nodes			[37]	
Spleen				[15]
Prostate			[38]	

Table 1.1: *A list of acoustic parameters describing ultrasound-tissue interactions that showed potential for UTC.*

tissue function and morphology, but appear to be strongly dependent on the machine settings and are qualitative in nature. Therefore, there has been a growing interest in techniques that would provide quantitative information on the characteristics of the examined structures. This field of study is referred to as *ultrasound tissue characterization* (UTC) and aims to improve ultrasonic diagnostic capabilities by quantitatively measuring physical properties that can be linked to the tissue state. The central hypothesis of UTC is that tissue affected by a disease or medical treatment undergoes micro-structural changes that impact the way the ultrasound waves interact with the tissue and thus the reflected echo signals. UTC has traditionally used ultrasound modelling and signal analysis to derive physical parameters that can characterize and differentiate between healthy and diseased tissues. However, some descriptive parameters can only be extracted from RF signals before they undergo the process of the envelope detection. The following discussion will focus on the fundamental acoustic parameters describing ultrasound-tissue interactions that showed potential for UTC. A list of such parameters and their area of application are summarized in Table 1.1.

1.2.1 Inverse scattering methods

UTC is, in fact, an *inverse scattering problem*. Indeed, based on the scattered data from the tissue, UTC attempts to derive the tissue characteristics. Inverse methods employ an analytical model, which is used to derive the required parameters from the available data. However, due to the complexity of ultrasound-tissue interactions, a number of simplifying assumptions regarding the tissue structure and experimental settings have to be made. Conventional UTC methods typically focus on one particular parameter and consist of three

main steps: first, experimental data is corrected for any system-dependent effects (i.e. diffraction, mechanical and electrical properties of the transducer); next, an attempt is made to isolate the ultrasound-tissue interactions that are described by the parameter of interest, and finally, the reconstruction of this parameter is perfomed on the basis of the assumed model [39]. The main challenge of such approach consists in the need to correct for the system-related effects that are inherently spatially-variant.

1.2.2 Ultrasound spectrum analysis

The majority of UTC methods employ frequency-domain analysis of RF echo signals by computing their power spectral density. The procedure begins with the selection of the region of interest (ROI) on a reconstructed B-mode image (Fig. 1.9), that is further subdivided into a set of segments. The number of such segments depends on the application, while their size is determined by the number of adjacent scan lines on one side and the number of time windows along each scan line on the other. Time windows are gated using a particular window function (e.g. rectangular, Hann, Hamming window, etc.) and typically overlap. The RF echo spectrum in every window is then calculated uisng the fast Fourier transform algorithm (FFT), and the average power spectral density of a segment is computed as the mean of the squared spectral amlitudes from all windows within this segment [40].

Frequency-domain algorithms typically use a reference phantom method to correct for the system dependencies [41]. Namely, both the sample and a reference medium with known acoustic properties are scanned using the same transducer and system settings. The sample power spectral density at every depth inside the selected region of interest (ROI) is then divided by the power spectrum of the reference phantom estimated at the same depth, and the frequency dependence of the normalized power spectrum is further used to estimate the parameter of interest. Although this method presents a relatively straightforward procedure to correct for the system-related effects, its use in clinical practice is limited due to a number of constraints. First of all, it presents an additional measurement which has to be repeated every time the system settings (e.g. focal settings) are changed. Furthermore, this method relies on the assumption that the speed of sound in the sample and in the reference phantom are constant and identical, which is not always the case. Violation of this assumption results in a mismatch between the focal patterns in the sample and reference measurements which leads to inaccurate parameter estimates [42]. Moreover, these algorithms do not account for the interactions of an ultrasound beam with proximal tissue layers that may influence the spectral characteristics.

15
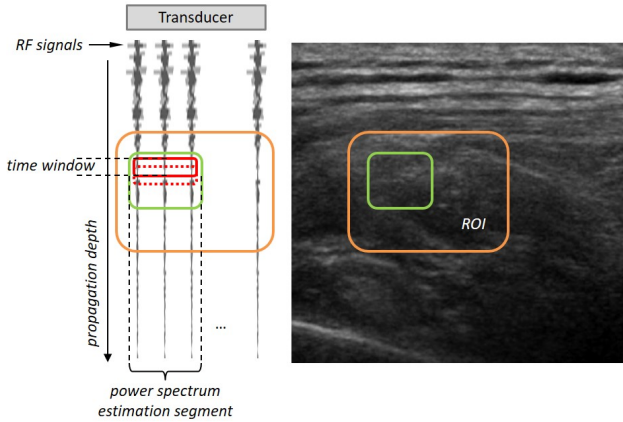
Figure 1.9: *Schematic illustration of the procedure for power spectral density estimation which is utilized by the spectral domain UTC methods.*

1.3   Objectives and outline of this thesis

The aim of this thesis was to develop and validate a fundamentally different approach for reconstruction of the local acoustic properties, wherein the *forward scattering problem* is iteratively solved through computer simulations in order to match the synthetically generated ultrasound data to the experimentally observed ones. The advantage of such approach is that numerical modelling of the forward ultrasound wave propagation enables to study various ultrasound-tissue interactions as well as their combined effect in a controlled manner. Moreover, diffraction effects do not need to be corrected for as they are intrinsically incorporated into the propagation model.

The proposed methodology can be divided in three main steps: 1) *simulation*, i.e. modelling of the forward ultrasound wave propagation assuming a set of acoustic properties of the medium and estimation of the spectral characteristics of the backscattered signal; 2) *comparison* of the spectral characteristics of the simulated and experimentally observed signals using a pre-defined similarity measure; and 3) *optimization* applied in order to retrieve tissue parameters corresponding to the highest similarity between the modelled and experimentally measured outputs. The proposed method can be modified or improved at all levels to better suit a particular task and can be potentially used in a variety of applications. In this manuscript, we focus on the effects of attenuation and employ the above approach to estimate the attenuation coefficient (Eq. 1.4) of soft tissue and tissue-mimicking materials.

For completeness, simulation of the forward ultrasound propagation should in-

clude all ultrasound propagation phenomena described in section 1. However, modelling the combined effect of all above mentioned phenomena is very complex as all effects impact each other. Besides, it would make it very difficult to validate the resulting model in an experimental setting. Therefore, the feasibility of the proposed approach was first tested in a simplified case. The complexity of the model was then gradually increased.

More specifically, the objectives of this thesis were:

- Investigate the feasibility of the proposed approach in the simplified case of plane wave propagation.

- Increase the complexity of the propagation model (i.e. include the system-dependent effects) and validate the novel approach on synthetic and experimental data.

- Adapt the propagation model to a clinical setting (i.e. array transducer, heterogeneous media) and perform the complete validation on synthetic and experimental data acquired in-vitro and in-vivo.

The manuscript is structured as follows. Chapter 2 investigates the feasibility of the proposed approach in a simplified case of 1-D, linear plane wave propagation. An overview of the existing methods for the attenuation estimation is provided and their limitations are discussed. The proposed approach is validated on synthetically generated data and experimental data recorded in tissue-mimicking phantoms and its performance is compared against the two reference methods commonly used in the literature. Given the promising results of the feasibility study, chapter 3 presents an extension of the underlying model to a case of 3-D wave propagation in a heterogeneous medium. The aim of this extension is to include diffraction effects that are modelled using the angular spectrum approach. The theoretical background for the improved model and its numerical implementation are discussed in detail, followed by the validation of the improved methodology for the attenuation estimation on synthetic and experimental phantom data presented in chapter 4. As a step towards in-vivo application, chapter 5 describes an extension of the model to a case of a linear array transducer as clinically used. The complete validation of the refined model including in-silico, in-vitro and in-vivo validation is the subject of chapter 6. In the latter case, the attenuation coefficient is estimated in the liver in healthy volunteers. Finally, in chapter 7 the most important conclusions of this work are summarized and some speculations are made regarding the future perspectives of this work and the potential of the developed approach in clinical practice.

Chapter 2

Attenuation estimation by repeatedly solving the forward scattering problem

Abstract

Estimation of the ultrasound attenuation in tissue is important in medical ultrasound not only for correct time-gain compensation but also for tissue characterization. In this chapter, the feasibility of a new method for attenuation estimation is evaluated. The proposed method estimates the attenuation by repeatedly solving the forward wave propagation problem and matching the simulated signals to the measured ones. This approach allows to avoid common assumptions made by other methodologies and potentially allows to account and correct for other acoustic effects that may bias the attenuation estimate. The performance of the method was validated on simulated data and on data recorded in tissue mimicking phantoms with known attenuation properties, and was compared to the spectral-shift and spectral-difference methods. Simulation results showed the different methods to have good accuracy when noise-free signals were considered (the average relative error of the attenuation estimation did not exceed 15 %). However, the accuracy of the conventional methods decreased rapidly in the presence of measurement noise and varying scatterer concentration, while the relative error of the proposed method remained below 15 %. Furthermore, the proposed method outperformed conventional attenuation estimators in the experimental phantom study, where its average error was 8 %, while the average error of the spectral-shift and spectral-difference methods was 26 % and 32 %, respectively. In summary, these findings demonstrate the feasibility of the proposed approach and motivate us to refine the method for solving more general problems.

2.1 Introduction

Ultrasound has been widely used in clinical practice as a diagnostic tool due to a number of advantages, such as portability, relative inexpensiveness, absence of ionizing radiation, and the possibility of real-time imaging. A critical step in ultrasound image reconstruction is attenuation correction which is typically performed by means of time-gain compensation (TGC). Automatic TGC is widely used and consists in increasing the gain of the reflected signals with increasing depth according to a predefined attenuation profile. However, this method does not account for shadowing and enhancement artefacts that may be induced by variations in local attenuation of the scanned region. Such artefacts can only be eliminated by proper attenuation correction [43, 44]. Therefore, a methodology that yields a reliable estimation of the local acoustic attenuation would be very helpful to improve TGC.

Moreover, quantitative assessment of the ultrasound attenuation coefficient and its frequency dependency can be used for tissue characterization. In liver di-

agnosis, for instance, the attenuation coefficient significantly increases in both fatty and fibrotic liver [7,12]. In breast tissue, the attenuation coefficient is low for fatty tissue and medullary carcinoma and high for fibrotic tissue and ductal carcinoma [20,21]. Several studies showed that attenuation increases in regions of myocardial infarction [27,30]. As an alternative for ultrasound attenuation, other acoustic parameters (such as the local backscatter coefficient, effective scatterer size, acoustic concentration or nonlinear parameter) could be used for the UTC purposes. However, for a reliable estimation of these parameters a correct TGC is required [45–47].

To accomplish this, a variety of techniques for attenuation estimation from reflected ultrasound signals has been developed over the last four decades. Most techniques solve the so-called "inverse scattering problem" by estimating the acoustic parameters directly from the recorded backscatter signals in either time or frequency domain. In the time-domain, an attenuation estimate can be obtained by analysing the noise-to-signal ratio of the echo envelope peaks [48]. A method based on the entropy difference between two adjacent envelope segments of the narrowband reflected signal was proposed by Jang [49]. Knipp & Zagzebski [50] developed a video-signal analysis technique for estimating the attenuation from B-mode images. Although time-domain methods are computationally fast and easy to implement, compensation for the diffraction effects is very difficult in time-domain.

In the frequency-domain, two main approaches for the attenuation estimation exist: the spectral-shift approach, which estimates the center frequency downshift of the power spectrum as a function of depth, and the spectral-difference approach, which measures the power spectrum amplitude decay with propagation depth. In the implementation of the spectral-shift algorithm, a Gaussian shape of the transmitted pulse and of the reflected echo is assumed, and the attenuation coefficient is estimated from the slope of the decay of the center frequency with depth [51]. A method for estimating the center frequency downshift using the short-time Fourier analysis has been described by Fink [52]. Baldeweck [53] used a parametric spectral analysis based on autoregressive modelling to estimate the center frequency along the propagation depth. Kim & Varghese [54] obtained the spectral shift from the position of the maximum of the cross-correlation function between successive power spectra. The center frequency downshift was also determined in the time-domain by measuring the density of zero-crossings of radio-frequency (RF) signals for the case of a linear [55] and nonlinear [7] frequency dependence of the attenuation coefficient.

A spectral difference approach, in which the attenuation coefficient was estimated as a function of frequency by measuring the decay of the power spectrum components with depths, was described by Parker [56, 57]. Kuc [58–60] proposed a log-spectral difference approach, where the attenuation coefficient was

estimated by analysing the ratio of the power spectra at two different depths (distal and proximal). Insana [61] improved this method by including the effects of the transducer diffraction pattern. Later, Yao [41] proposed a reference phantom method for the attenuation and backscatter coefficient estimation where a reference phantom was used to correct for the system and transducer dependencies. More recently a hybrid method was proposed that combines both the spectral shift and spectral difference techniques [62]. This method uses a reference phantom method to minimize the diffraction effects, whereupon the attenuation coefficient is estimated using the spectral cross-correlation algorithm mentioned above [54].

Despite the large variety in methodologies, application of the existing techniques is difficult in clinical practice. This is primarily due to a violation of their underlying assumptions. For spectral-shift methods, the violation concerns a non-Gaussian shape of the transmitted pulse, a nonlinear frequency dependent attenuation and the presence of diffraction effects due to the beam focusing [52,57,60,63], while spectral-difference methods experience difficulties in media with non-uniform scattering properties [61,62]. Although the hybrid method overcomes some limitations by combining both techniques, handling of the in-vivo data remains a problem due to the spectral amplitude variation caused by the random distribution of tissue scatterers and the presence of noise [55]. Finally, when the attenuation is estimated directly from the backscattered signal, other than diffraction acoustic effects may influence the attenuation estimate and have to be corrected for or neglected under certain assumptions.

Considering the shortcomings of the existing methods, the ultimate goal of our research is to quantitatively describe the influence of a combination of acoustic effects on the propagation of the acoustic wave, and to attempt to estimate several effects simultaneously from the recorded backscattered data. For this purpose, we propose an alternative approach where a computer model is used to solve the forward scattering problem. The input acoustic parameters of the model can be iteratively changed in order to have the model generate a synthetic signal that matches the experimentally observed signal. The acoustic parameters that result in the best match between the simulated and measured signals are considered to be the true parameters of the investigated medium. The complete model of the forward propagation should ideally include the effects of diffraction, attenuation, nonlinear distortion, dispersion, reflection and refraction. However, although each individual effect may be described by a relatively simple model, analysis of the combined effect of all above-mentioned phenomena is very complex. In this chapter, we present a feasibility study of the above approach in a substantially simplified setting. In particular, we focus on the attenuation estimation considering all other medium parameters to be known. Moreover, we assume linear plane wave propagation in a homo-

geneous dispersion-free medium avoiding the effects of diffraction, dispersion, nonlinear distortion, reflection and refraction (effectively reducing the problem to 1-D).

The present chapter is an extension of preliminary results that were described in [64]. The present version of the algorithm for attenuation estimation was improved; its performance was more thoroughly validated on both simulated and experimental data, and the results were compared with estimates obtained using the two traditional frequency-domain attenuation estimation methods: the spectral-shift method proposed by Fink [52] and the spectral-difference method proposed by Kuc [60].

The chapter is organized as follows: in section 2.2 the proposed method is described in detail; section 2.3 presents the simulation and experimental results and the comparison with traditional methods for attenuation estimation. The obtained results are discussed in section 2.4. Finally, the conclusion of this study is formulated in section 2.5.

2.2   Materials and methods

The proposed approach consists of three main steps. First, the forward wave propagation is modelled using the plane wave approximation assuming a set of acoustic properties of the medium, and the spectrum of the backscattered signal is estimated. Then, the spectra of the simulated and experimentally observed signals are compared using a pre-defined similarity measure. Finally, the first two steps are repeated for a series of values of a varying input attenuation coefficient, and the attenuation coefficient corresponding to the highest similarity between the spectra is determined.

2.2.1   Acoustic model

Considering a simplified model of plane wave propagation in an isotropic and homogeneous medium and using the Born approximation of weak scattering, the power spectral density, $\mathcal{P}(f, z)$, of the signal received at the ultrasound transducer from a thin slice of a scattering medium at a depth z, can be expressed as [44, 65]:

$$\mathcal{P}(f, z) = V^2(f)A^2(f, 2z)B^2(f, z), \tag{2.1}$$

where $V(f)$ embodies the combined effect of the electrical excitation and the electromechanical coupling of the transducer that can be experimentally determined through a pulse-echo reflector measurement, $A(f, z) = e^{-\alpha f z}$ is the

attenuation operator that is defined assuming propagation in a dispersion-free medium and a linear frequency dependence of the attenuation, and $B(f, z)$ stands for the frequency-dependent backscatter characteristics at depth z. The power spectral density can be calculated as a squared amplitude of the signal's Fourier spectrum, i.e. $\mathcal{P}(f, z) = |S(f, z)|^2$, so we can write:

$$|S(f, z)| = |V(f)A(f, 2z)B(f, z)|, \tag{2.2}$$

Further, the scattering characteristics can be considered constant with depth, and the scattering operator can be expressed as [44, 54]:

$$B(f, z) = B_0(z)f^l, \tag{2.3}$$

where we have chosen $l = 2$ [44] for Rayleigh scattering and $B_0(z) = B_0$ is assumed to be constant along the homogeneous medium.

2.2.2 Spectral comparison

The comparison of the spectrum of the backscattered signal obtained in the simulation to the spectrum of the experimentally observed backscattered signals was performed using a sliding window approach. The first window was used for calibration by equalizing the energies of the simulated and measured spectra. In this way, the amplitude coefficient B_0 in 2.3 can be eliminated. Similarity between the simulated and measured spectra in every subsequent window was analysed by calculating the least squares difference:

$$D(z, \alpha) = \sum_f \left(|S_{meas}(f, z)| - |S_{sim}(f, z)| \right)^2, \tag{2.4}$$

where $|S_{meas}(f, z)|$ is the amplitude of a measured spectrum in the window at depth z and $|S_{sim}(f, z)|$ is the amplitude of the simulated spectrum at the same position.

2.2.3 Optimization

In order to approximate the experimentally observed signals within reasonable accuracy, the above simulation procedure was repeated for different input values of the attenuation coefficient. The attenuation coefficient in the model was discretely changed in a chosen interval, and the coefficient corresponding to the highest similarity between the simulated and the measured signals in each analysis window was determined by means of an exhaustive search.

The global attenuation coefficient of the sample was finally estimated as the average of the coefficients determined for all windows:

$$\bar{\alpha} = \frac{\sum_{i=1}^{L} \arg\min_{\alpha} D(z_i, \alpha)}{L},$$ (2.5)

where z_i is the distance to the i$^{\text{th}}$ window and L is the number of all windows excluding the first one.

The performance of the proposed method was first evaluated on simulated signals that were also used to determine the optimal spectral window sizes for the proposed and reference methods. Subsequently experimental data was used for testing and validation.

2.2.4 Data generation

Synthetic Data: Simulated signals were obtained by modelling the forward plane wave propagation and backscatter of the input pulse in media with a-priori known acoustic characteristics. Scattering was modelled as a reflection from a distribution of scatterers in the far-field of a flat unfocused single-element transducer that were placed on the propagation axis. For this purpose, a number of 1-D random distributions of point scatterers were generated at a predefined density (150 scatterers per mm). The reflection from a single scatterer was calculated by attenuating the input pulse on its forward propagation to the scatterer location and on its backward propagation to the position of the source using the attenuation transfer function in Eq. 2.2 in the frequency domain. Herein, the frequency dependence of the scattering process was omitted. Finally, the signals from all scatterers were summed in the time-domain to obtain a single RF line:

$$RF(t) = \sum_{i=1}^{N_{sc}} \left[\mathcal{F}^{-1} \left\{ V(f) A(f, 2z_i) e^{-j2\pi f \Delta t_i} \right\} \right],$$ (2.6)

where N_{sc} is the total number of scatterers in the distribution, $\mathcal{F}^{-1}\{x\}$ represents the inverse Fourier transform of x and z_i is the depths of the i$^{\text{th}}$ scatterer in the distribution. The exponential term describes the delay of each scattered signal, where $\Delta t_i = 2z_i/c - t_p/2$ and t_p is the duration of the input pulse.

For this study, homogeneous tissue-like media with a speed of sound of 1500 m/s, mass density of 1100 kg/m^3, and three different attenuation coefficients: $\alpha = 0.3$, 0.5 and 0.7 dB/cm/MHz, were considered. The input pulse had a

Gaussian shaped spectrum, $V(f)$, with a 2.25 MHz center frequency and a 50 % fractional bandwidth. 50 RF signals of 40 mm length (˜60 wavelengths) were generated for different realizations of the positions of the scattering sites to allow for averaging as typically recommended for attenuation estimation. Additionally, the performance of the current method and of the two traditional spectral-shift and spectral-difference methods [52, 60] was tested for a decreasing number of RF lines. Hereto, a different number of signals was considered: 1, 5, 7, 10, 30 and 50 RF lines. Furthermore, the influence of the measurement noise was examined by adding white Gaussian noise (with signal to noise ratio (SNR) of 12 and 6 dB) to the simulated signals and by repeating the attenuation estimation for this set of noisy signals. Moreover, the performance of the considered methods was tested in media with weakly varying scattering concentrations, as often seen in practice. For this purpose, 10 RF signals were generated for media composed of three adjacent layers of 20, 10 and 10 mm with scattering concentrations of 150, 165 and 180 scatterers per mm, respectively (test 1) and 150, 180 and 195 scatterers per mm, respectively (test 2). Subsequently, white Gaussian noise (6 dB SNR) was added to these signals.

Experimental Data: The performance of the proposed method was also tested on experimental data. For this purpose, tissue mimicking phantoms with different attenuation characteristics were prepared. Three types of phantoms were built as described in [66–68] by mixing gelatin-, agarose- and PVA-based gels with different concentrations of graphite powder in order to modify the attenuation characteristics of the materials and to achieve sufficient scattering. Six homogeneous cylindrical phantoms (40-50 mm in length; 35 mm in diameter) were used in this study: three gelatin-based phantoms, named "Phantom A", "Phantom B" and "Phantom C"; one agarose-based, termed "Phantom D", and two PVA-based phantoms, labelled "Phantom E" and "Phantom F". The different phantom families were made by mixing dry powder of gelatin, 13.5% (AppliChem, Darmstadt, Germany), agar, 3.85% (Merck, Darmstadt, Germany) and PVA, 10% (Sigma-Aldrich Chemie, Steinheim, Germany), respectively, with deionized water. Graphite powder in concentration of 50-70 g/L (Acros Organics, Geel, Belgium) was used to alter the scattering and attenuation properties.

The acoustic parameters of the phantoms were first measured using a traditional through-transmission substitution method, and their values are listed in Table 2.1. The through-transmission substitution method consists in a comparison of signal amplitudes in a medium with known parameters (i.e. distilled water) with those obtained during the actual propagation through the sample [69, 70]. As such, a reference measurement was first made in a tank filled with distilled water using two transducers. Next, a phantom was placed in the water in-between the two transducers. All measurements were performed at

room temperature (22 ˚C).

Fig. 2.1a shows a schematic diagram of the through transmission setup used for these measurements. Flat unfocused single-element 0.5" transducers with 65% fractional bandwidth and 10 MHz center frequency (V311-SU, Panametrics NDT, Inc., Waltham, MA) were used. Successive sinusoidal bursts, produced by a waveform generator (AWG NI PXI 5412, National Instruments Corporation, Austin, TX) and PC-controlled by LabVIEW, were sent in the form of a discrete frequency sweep (from 0.5 till 20 MHz with 250 kHz step), such that, at each frequency, the waveform consisted of 120 cycles. This signal was amplified (150A100B Amplifier Research, Souderton, PA) and sent to the emitting transducer. 64 transmitted signals, recorded at the receiving transducer, were digitized by means of a data acquisition card (DAQ PXI NI 5122, 14 bit, 100 MHz sampling rate, National Instruments Corporation, Austin, TX), and the averaged signal was stored on the PC.

The speed of sound of the phantom was determined using a cross-correlation calculation involving the first echoes of the signals received with and without the phantom placed in-between the transducers. For the reference medium a speed of sound of 1483 m/s was used for these calculations (sound speed in distilled water at 22 ˚C). The determined speed of sound for each phantom was constant with frequency and its value was used as an input in the simulations. The attenuation coefficient of the phantom was calculated from the ratio of the fundamental pressure amplitudes between the reference signal and the sample signals assuming an exponential law. The determined attenuation coefficients for each phantom showed a linear dependence on frequency. Its values were considered as ground-truth and were used for the verification of the attenuation estimates obtained from the backscattered signals.

	Ph. A	Ph. B	Ph. C	Ph. D	Ph. E	Ph. F
Density, kg/m ^{3}	1305	1086	1000	1100	1276	1198
Speed of sound, m/s	1518	1546	1552	1520	1587	1596
Attenuation coefficient, dB/cm/MHz	0.74	0.61	0.63	0.84	0.39	0.63

Table 2.1: *Acoustic properties of the tissue mimicking phantoms.*

The backscattered signals were recorded in pulse-echo mode. The schematic diagram of the experimental setup used for these measurements is shown in Fig. 2.1b. A single transducer operated as emitter as well as receiver. Depending on the availability at the time of the experiment, three different types of transducers were used for the backscatter measurements. All transducers were flat unfocused single-element, 0.5" (13 mm) transducers: a V306-SU with a 2.25 MHz center frequency and 60% bandwidth, an A306-SU with 2.25 MHz center

frequency and 50% bandwidth and a V309-SU with 5 MHz center frequency and 65% bandwidth (Panametrics NDT, Inc., Waltham, MA). A phantom was placed in the water tank in the far-field of the emitting/receiving transducer in order to avoid near-field diffraction effects and to approximately satisfy the plane-wave assumption. The far-field distance for the transducers was calculated as:

$$z_{far-field} = \frac{a^2}{4\lambda},$$ (2.7)

where a is the transducer diameter (in this case 13 mm) and λ is the wavelength. Thus, using a speed of sound in distilled water at room temperature (1483 m/s), the far-field distance for the 2.25 MHz transducer was $d = z_{far-field} = 70$ mm and $d = 140$ mm for the 5 MHz transducer.

A negative impulse was generated on a Pulser/Receiver (5058PR, Panametrics Canada NDT, Quebec) and sent to the emitting/receiving transducer. At a fixed transducer-phantom distance, 16 received signals were averaged, digitized on a data acquisition card and stored on the PC for further analysis. For each phantom, 10 signals were acquired, slightly moving the transducer in the plane parallel to the surface of the phantom with steps of 2 mm. The movement was done by linear motion stages (Velmex Bislides, Velmex Inc., Bloomfield, NY) controlled by a stepper motor drive (NI MID-7604) connected to a motion controller (NI PXI 7334, National Instruments Corporation, Austin, TX).

Since the waveform of the actually transmitted pulse is required for the simulations used in our approach, reflections of the emitted pulses from a metal needle were measured. Hereto, a 0.04 mm needle was placed at the same distance from the transducer as the phantoms. The recorded pulses were used as input for the simulations. It should be noted that the needle acts as a point scatterer and the spectrum of the recorded reflections contains the frequency dependence of f^2. Hence, when a needle reflection is used as an input pulse in Eq. 2.1, the frequency dependence of $B(f,z)$ can be further omitted as it has then intrinsically been accounted for.

2.2.5   RF data processing

In both the synthetic and real experiments, the observed RF signals were compared with the simulated ones using a sliding window analysis. A size of the sliding window of 20 mm (~30 wavelengths) and a 75% window overlap were chosen as the optimal parameters for robust attenuation estimation. In every window, the average of 10 Fourier spectra, acquired at different positions from the central axis in the same plane, was used for comparison with the simulated spectrum. Because the attenuation coefficient of soft tissue in general,
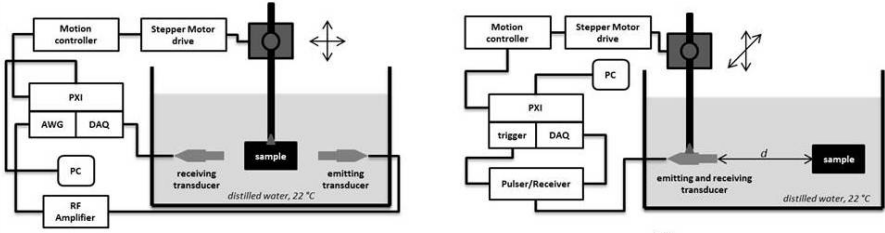
Figure 2.1: *A schematic diagram of the experimental setup for (a) through-transmission insert-substitution experiment and for (b) the pulse-echo setup, where d is the distance between the sample and transducer (7 cm for 2.25 MHz transducer and 14 cm for 5 MHz transducer).*

as well as the value for the tissue-mimicking phantoms under consideration, is not expected to exceed 2 dB/cm/MHz [71], the input attenuation coefficient in the simulation was discretely changed in the interval between 0 and 2 dB/cm/MHz with a step of 0.01 dB/cm/MHz. The distance between the spectra of the windowed signals was calculated for every input value using Eq. 2.3. A -20 dB frequency range of all spectra was selected for the comparison in order to operate above the noise floor (Fig. 2.2) [63, 72].

The results of the proposed method were compared to the estimates obtained using two state-of-the-art methods for attenuation assessment: a spectral-shift method based on the short-time Fourier analysis developed by Fink [52] and a spectral-difference method proposed by Kuc [60].

The spectral-shift method computes the spectrum of the signal using short-time Fourier analysis at each position of the sliding window. The center frequency downshift is obtained by computing the spectral moments of the 0th, 1st and 2nd order. The spectral-difference method estimates the attenuation coefficient from the log-spectral difference of two windows at the proximal and distal surfaces of the medium [73]. The size of the spectral window for each method was chosen as the one corresponding to the lowest error of this method in the simulation study. The optimal spectral window size for the spectral-shift method was 18 mm (27 wavelengths) with 50% overlap, while the optimal window size for the spectral-difference method appeared to be 8 mm (12 wavelengths). The proximal segment was positioned in the beginning of the backscattered signal (0 mm) and the distal segment at the end of the signal (at 30 mm or 45 wavelengths). Again -20 dB bandwidth of the signal spectra was selected in order to operate above the noise level.
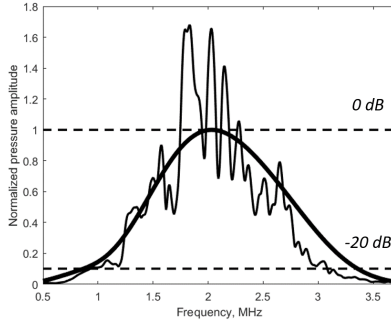
Figure 2.2: *The fit of the simulated spectral curve to the spectrum of the windowed measured signal.*

2.3 Results

The results of the attenuation estimation on the first set of synthetic data using all three methods are presented in Fig. 2.3. The average error of the attenuation estimation with all three methods did not exceed 15 %. The best accuracy was achieved with the spectral-difference method. In Fig. 2.4, the influence of measurement noise on the performance of all three methods is presented as well as the effect of using a different number of RF lines for spectral averaging. Two aspects can be appreciated: 1) while the average estimates only slightly improve when the number of RF lines increases, the standard deviation of the estimates decreases substantially for all three methods when increasing the number of RF lines, 2) in the presence of noise, the spectral-shift method was unable to provide realistic estimates (the error exceeded 100 %). In contrast, the error of the proposed and spectral-difference methods did not change markedly in the presence of noise; both methods showed stable performance when 10 or more RF lines were used for spectral averaging. The spectral-difference method once again showed the best accuracy. Fig. 2.5 presents the results of the attenuation estimation in 2 media with depth-dependent scatterer concentrations. It can be noticed, that the accuracy of the spectral-difference method decreased with increasing degree of heterogeneity, while the performance of the proposed and spectral-shift methods was not influenced by the weak variations in scatterer density. However, the spectral-shift method once again failed to provide accurate attenuation estimates in the presence of measurement noise, while the performance of the proposed method remained stable.

For the experimental data, the estimates of the attenuation coefficients computed from the backscattered signals with all three methods were compared with the "ground-truth" attenuation coefficients that were measured using the

Figure 2.3: *Comparison of the performance of the proposed method with the spectral-shift method (SSM) and the spectral-difference method (SDM) on synthetic data: estimated attenuation coefficients (a) and average relative error of the obtained attenuation estimates (b).*

insert-substitution method as mentioned above (Table 2.2). The results are presented in Fig. 2.6. The average error of the attenuation estimation with the proposed method was 8%, while the average error of the spectral-shift and spectral-difference methods amount to 26% and 32%, respectively.

	Ph. A a	Ph. B a	Ph. B b	Ph. C b	Ph. D a	Ph. D c	Ph. E a	Ph. E b	Ph. F b
"Ground truth"	0.71	0.61	0.61	0.63	0.84	0.84	0.39	0.39	0.63
SSM [52]	1.12	0.18	0.50	0.57	0.79	1.14	0.41	0.48	0.66
SDM [60]	1.00	0.42	0.24	0.36	0.63	0.99	0.39	0.30	0.35
Proposed Method	0.85	0.67	0.52	0.66	0.82	0.88	0.38	0.38	0.59

Table 2.2: *Comparison of the estimated attenuation coefficients (dB/cm/MHz) of the tissue-mimicking phantoms obtained with the three methods (spectral-shift method, spectral-difference methods and currently proposed method) to the "ground truth" values of the attenuation coefficients measured using the insert-substitution method. The small letters "a", "b" and "c" refer to the results obtained with the three different transducers used in the experiments: V306 (2.25 MHz), V309 (5 MHz) and A306 (2.25 MHz) respectively.*
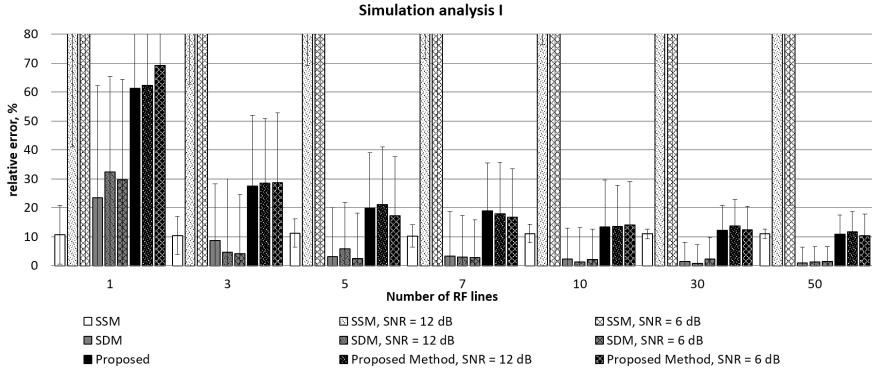
Figure 2.4: *Analysis of the performance of the spectral-shift method (SSM), the spectral-difference method (SDM) and the proposed method depending on the number of the recorded RF lines and presence of noise in the signal (SNR = 6 and 12 dB).*

2.4 Discussion

As can be seen from the simulation study, the most accurate attenuation estimates were obtained with the spectral-difference method in the absence of noise. When white Gaussian noise (12 and 6 dB SNR) was applied to the signals, the accuracy of the spectral-shift method substantially decreased. The results clearly showed that the spectral-shift method in its current implementation is unable to produce reliable results in the presence of noise. On the contrary, the proposed and spectral-difference methods have a much lower sensitivity to noise and did not show a substantial change in performance. Furthermore, spectral attenuation estimation methods are known to perform better when a high number of RF lines is available for obtaining a stable spectral estimate. Typically, spectral methods use at least 25 RF signals to obtain a stable power spectrum even when a homogeneous medium is considered [63, 72, 74]. Indeed, the results of the simulation study showed that even though an increase in the number of RF lines did not lead to a substantial improvement in the accuracy of the conventional methods, their standard deviation decreased considerably. The proposed method showed a competitive performance when the number of RF lines available in the simulation study was equal or higher than 10. As expected, the error of the spectral-difference method increased in media with depth-dependent scatterer concentrations. However, these weak variations did not influence the performance of the proposed and spectral-shift methods. Overall, the results of the simulation study are in a good agreement
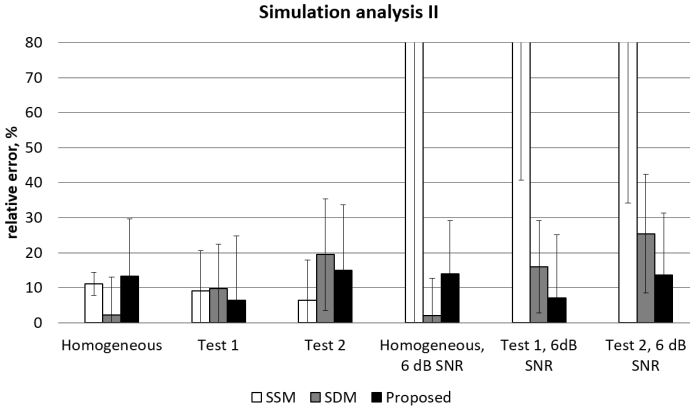
Figure 2.5: *Analysis of the performance of the spectral-shift method (SSM), the spectral-difference method (SDM) and the proposed method in media with depth-dependent scatterer concentrations and in the presence of measurement noise. Test 1: 3 layers of 20, 10 and 10 mm with 150, 165 and 180 scatterers per mm, respectively. Test 2: 3 layers of 20, 10 and 10 mm with 150, 180 and 195 scatterers per mm, respectively.*

with the previous studies that also reported on 1) the poor performance of the spectral-shift method in noisy media due to the distortion of the spectral shape and the associated problems with the center frequency estimation [62], and 2) difficulties of the spectral-difference method in media with non-uniform scattering properties [41, 62, 74]. On the contrary, the proposed method does not rely on the assumption of the Gaussian shape of the signal spectrum and appears less sensitive to scattering variations due to the averaging of the attenuation estimates obtained in successive overlapping gated windows.

In the experimental phantom study, the error on the attenuation estimation of the conventional methods was found to be substantially higher than that of the proposed method. There are several possible reasons for this. First of all, the decrease in accuracy of the spectral-shift method could be explained by the presence of noise in the measurements that already showed to be critical in the simulation study. Further, in the conducted experimental study, only 10 RF lines were available, while the conventional spectral-shift and spectral-difference methods were previously validated using 32 and 25 RF signals, respectively [52, 61]. Again based on the simulation study, one can expect relatively high standard deviations for the attenuation estimates in this case. However, increasing the number of RF lines implies increasing the lateral size of the ROI which is not always practical in a clinical setting [63, 74]. Fur-
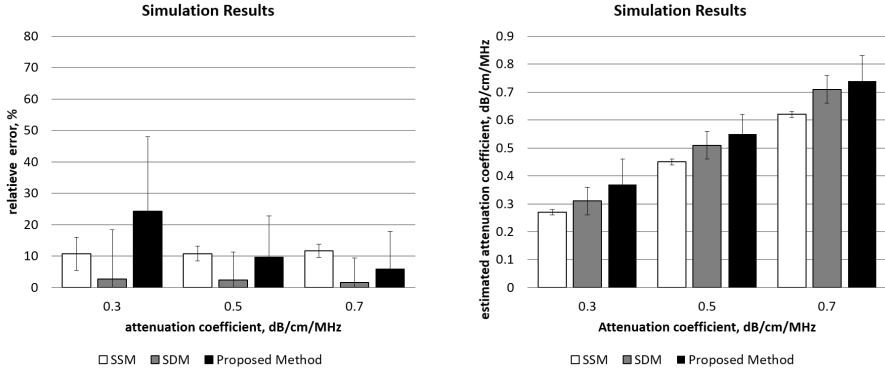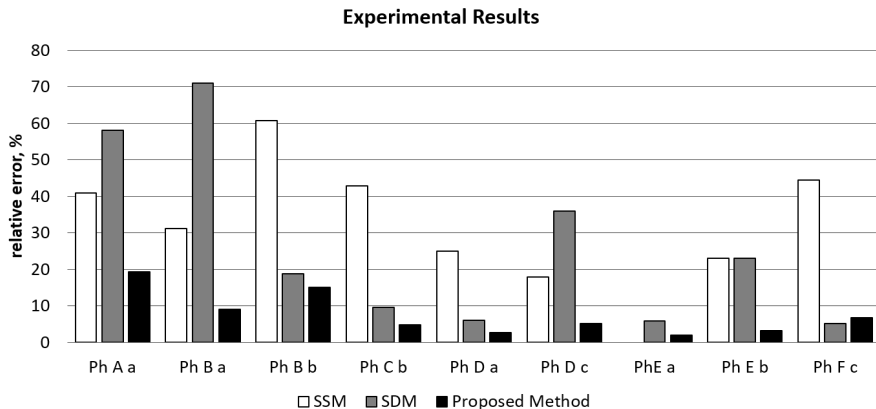
Figure 2.6: *Comparison of the performance of the proposed method with the spectral-shift method (SSM) and the log-spectral-difference method (SDM) on experimental phantom data. The small letters "a","b" and "c" refer to the three different transducers used in the experiments: V306, V309 and A306, respectively.*

thermore, distributions of scatterers in the tissue-mimicking phantoms made for this study were perhaps not perfectly uniform, which, as discussed above, would affect the performance of the spectral-difference method. On the contrary, the proposed method showed a stable performance with an error not exceeding 20% for all phantoms.

High errors of the attenuation estimates obtained with the spectral-shift and spectral-difference methods have been previously reported. Kim & Varghese [62] used 10 echo lines and a ROI of 120 mm by 100 mm in their simulation study, wherein homogeneous numerical phantoms were considered, and obtained a 30% error with the spectral-difference method. Hasan et al. [74] used 25 echo lines but considered a substantially smaller ROI of 4.7 mm by 7.8 mm inside of a tissue-mimicking phantom. The authors obtained very high errors with the spectral-difference method when selecting the ROI close to the transducer surface (38% and 26%) and showed that the spectral-shift method fails to estimate the attenuation coefficient when a ROI was selected at a depth of 30-50 mm from the transducer with the error above 50%. It should be also noted, that the reference methods considered in this study were implemented in their original version. A number of improvements to these methods has been discussed in the literature. However, the suggested advancements (e. g. spectral frequency smoothing [54]) are strongly dependent on the parameters defining them, the analysis of which was outside of the scope of this study.

In the present study, reference attenuation coefficients were available in both simulation and experimental studies, and the accuracy of the proposed method was assessed by calculating the relative error of the obtained estimates. However, in clinical practice, reference attenuation values are not always known, and a reliability measure may be required to assess the accuracy of the obtained estimates. In principle, the sum of squared differences between the simulated spectrum that corresponds to the estimated attenuation coefficient and the measured spectrum could be used as a measure of a goodness of fit. This aspect will be further investigated in future studies. Furthermore, even though in the present study a linear frequency dependence of the attenuation was considered, a general power law exponent αf^m can easily be accounted for in the model by including an additional parameter in the optimization process.

Overall, in this study, the goal was to demonstrate the feasibility of the proposed method for attenuation estimation in the simplified setting of plane wave propagation in a homogeneous medium with known scattering properties. The currently proposed approach clearly showed a good performance on both simulated and phantom data. The method also holds the advantage to be relatively insensitive to measurement noise and weak scattering variations.

As previously mentioned, the acoustic effects that may influence the attenuation estimation do not need to be corrected for post factum, as they can be included in the forward simulation model where they are intrinsically accounted for. In the future, the proposed method will be refined by including the diffraction effects in order to avoid the plane wave approximation. While currently a simplifying assumption of point scatterers was employed, a more accurate scattering model will be required for the estimation of attenuation in-vivo. Future work will also involve extension of the attenuation estimation to heterogeneous media with varying acoustic properties.

2.5   Conclusion

A new method for the estimation of the ultrasonic attenuation characteristic of a tissue mimicking medium from reflected signals was proposed. Hereto, computer simulations were used to solve the forward scattering problem for a varying input attenuation coefficient. The synthetically generated backscattered signals were then matched to the experimentally observed ones, and the attenuation coefficient was determined from the best fit between the signals. The performance of the proposed method was validated on synthetic and experimental data. The new method showed a performance comparable to conventional methods on the synthetic data, and the average error of the attenuation estimation did not exceed 15%. In the experimental study on tissue-mimicking

phantoms, the error of the newly proposed method did not exceed 20% and was substantially lower than those achievable by the conventional methods.

This chapter presents the results of the initial validation of the proposed methodology in a simplified case of linear plane wave propagation. In future studies, this methodology will be extended for the case of three-dimensional wave propagation by inclusion of diffraction effects, and will be further applied to estimate several additional acoustic parameters simultaneously (e.g. nonlinearity, dispersion, scattering, etc.).

Chapter 3

Three-dimensional simulation of ultrasonic wave propagation using angular spectrum approach

Abstract

Given the limitations of the proposed method discussed in the previous chapter, this chapter focuses on the improvement of the underlying model and its numerical implementation. We begin considering linear acoustic wave propagation in a homogeneous medium and recall the elements of the linear acoustic theory that form the basis for the improved model. We describe in detail the procedure for numerical modelling of acoustic wave propagation which is based on the angular spectrum approach (ASA). Application of the ASA is demonstrated using the example of a focused single-element transducer having a spherically-curved aperture, as will be used during the validation of the improved model. The pressure fields computed using ASA are compared to those obtained with Field II. Further, linear waves are considered in media with weak heterogeneities and a modified form of the linear equation is employed. Finally, applying linear systems theory to a consideration of an ultrasonic transducer, an expression for the spectrum of the backscattered signal detected by the transducer is obtained, which will be used in a model-based attenuation estimation algorithm described in the next chapter.

3.1 Acoustic pressure field in a homogeneous medium

When considering acoustic wave propagation in soft tissue, the propagation medium is typically treated as a fluid. Furthermore, the propagation medium is assumed to be homogeneous, isotropic and non-viscous. Moreover, small signal amplitudes are assumed allowing to neglect second order effects. An ideal fluid (i.e. uniform at rest) is characterized by elasticity (compressibility κ) and inertia (mass density ρ). Due to the property of elasticity, the fluid tends to return to its original state when there is a changing pressure working upon it, while due to inertia, the fluid tends to resist the compression. These basic properties allow acoustic wave propagation in fluid media. A vibratory motion applied to the fluid will generate a pressure wave, which, we assume, spreads spherically in all directions. The wave equation in this case is given by [75]:

$$\nabla^2 p(\boldsymbol{r}, t) - \frac{1}{c^2}\frac{\partial^2 p(\boldsymbol{r}, t)}{\partial t^2} = 0, \qquad (3.1)$$

in which t stand for the time, $c = {}^1/\sqrt{\kappa\rho}$ is the speed of wave propagation, ρ and κ are the equilibrium characteristics of the medium and $\boldsymbol{r} = (x, y, z)$ is the measurement point.

Within the linear first order approximation, the pressure field and the velocity potential field are related by [75]:

$$p(\boldsymbol{r}, t) = \rho \frac{\partial \phi(\boldsymbol{r}, t)}{\partial t}. \tag{3.2}$$

So that Eq. 3.1 can be rewritten in terms of the velocity potential field:

$$\nabla^2 \phi(\boldsymbol{r}, t) - \frac{1}{c^2} \frac{\partial^2 \phi(\boldsymbol{r}, t)}{\partial t^2} = 0, \tag{3.3}$$

Hereinafter, we will focus on the velocity potential field, from which the pressure can easily be derived using the above expression. Furthermore, throughout this chapter, acoustic wave propagation will be described using a frequency-domain representation, in which the following definition of the Fourier transform pair is used:

$$p(t) = \frac{1}{2\pi} \int\limits_{-\infty}^{\infty} P(\omega) e^{j\omega t} d\omega$$

$$P(\omega) = \int\limits_{-\infty}^{\infty} p(t) e^{-j\omega t} dt, \tag{3.4}$$

in which $\omega = 2\pi f$ and f are the angular and the ordinary frequencies, respectively.

Using the temporal Fourier transform of Eq. 3.3 we obtain the well-known Helmholtz equation:

$$\left(\nabla^2 + k^2 \right) \Phi(\boldsymbol{r} : \omega) = 0, \tag{3.5}$$

where $k = \frac{\omega}{c}$ is the harmonic wavenumber and $\Phi(\boldsymbol{r} : \omega)$ is the Fourier transform of $\phi(\boldsymbol{r}, t)$.

In the presence of harmonic sources in the volume of interest V, Eq. 3.5 receives an additional term describing the harmonic source distribution in space [75] (ch. 7, p. 320):

$$\left(\nabla^2 + k^2 \right) \Phi(\boldsymbol{r} : \omega) = -F(\boldsymbol{r} : \omega). \tag{3.6}$$

A solution to this equation can be found using the Green's function $G(\boldsymbol{r}|\boldsymbol{r_0})$ which describes the velocity potential field when the external source function

is a Dirac impulse $\delta(\boldsymbol{r} - \boldsymbol{r_0})$ in the point $\boldsymbol{r_0}$ and is a solution of the following differential equation:

$$\left(\nabla^2 + k^2\right)G(\boldsymbol{r}|\boldsymbol{r_0} : \omega) = -\delta(\boldsymbol{r} - \boldsymbol{r_0}), \tag{3.7}$$

The free medium Green's function for an outgoing wave is given by [75]:

$$G(\boldsymbol{r}|\boldsymbol{r_0} : \omega) = \frac{e^{-jk|\boldsymbol{r}-\boldsymbol{r_0}|}}{4\pi|\boldsymbol{r} - \boldsymbol{r_0}|}. \tag{3.8}$$

Multiplying Eq. 3.6 with $G(\boldsymbol{r}|\boldsymbol{r_0} : \omega)$ and Eq. 3.7 with $\Phi(\boldsymbol{r_0} : \omega)$, interchanging $\boldsymbol{r}$ and $\boldsymbol{r_0}$ using the reciprocity properties of $G(\boldsymbol{r}|\boldsymbol{r_0} : \omega)$ and $\delta(\boldsymbol{r} - \boldsymbol{r_0})$ and subtracting one equation from the other yields:

$$
\begin{aligned}
G(\boldsymbol{r}|\boldsymbol{r_0} : \omega)\nabla_0^2\Phi(\boldsymbol{r_0} : \omega) &- \Phi(\boldsymbol{r_0} : \omega)\nabla_0^2 G(\boldsymbol{r}|\boldsymbol{r_0} : \omega) = \\
&= \Phi(\boldsymbol{r_0} : \omega)\delta(\boldsymbol{r} - \boldsymbol{r_0}) - F(\boldsymbol{r_0} : \omega)G(\boldsymbol{r}|\boldsymbol{r_0} : \omega).
\end{aligned}
\tag{3.9}
$$

Integrating the above expression over the volume of interest V we obtain the velocity potential field within this volume:

$$
\begin{aligned}
\Phi(\boldsymbol{r} : \omega) = \int\limits_V F(\boldsymbol{r_0} : \omega)G(\boldsymbol{r}|\boldsymbol{r_0} : \omega)d\boldsymbol{r_0} + \\
+ \int\limits_V \left[G(\boldsymbol{r}|\boldsymbol{r_0} : \omega)\nabla_0^2\Phi(\boldsymbol{r_0} : \omega) - \Phi(\boldsymbol{r_0} : \omega)\nabla_0^2 G(\boldsymbol{r}|\boldsymbol{r_0} : \omega)\right]d\boldsymbol{r_0}.
\end{aligned}
\tag{3.10}
$$

Further, making use of the Green's theorem, the second integral in the above expression can be rewritten as a surface integral over the surface S enclosing the volume:

$$
\begin{aligned}
\Phi(\boldsymbol{r} : \omega) = \int\limits_V F(\boldsymbol{r_0} : \omega)G(\boldsymbol{r}|\boldsymbol{r_0} : \omega)d\boldsymbol{r_0} + \\
+ \int\limits_S \left[G(\boldsymbol{r}|\boldsymbol{r_0} : \omega)\frac{\partial\Phi(\boldsymbol{r_0} : \omega)}{\partial n} - \Phi(\boldsymbol{r_0} : \omega)\frac{\partial G(\boldsymbol{r}|\boldsymbol{r_0} : \omega)}{\partial n}\right]d\boldsymbol{r_0},
\end{aligned}
\tag{3.11}
$$

$\frac{\partial}{\partial n}$ denotes a partial derivative in the outward normal direction in the point $\boldsymbol{r_0}$ on the surface S. While the first integral in the above expression accounts for the source contributions within the volume V, the second one describes the pressure waves entering the volume.

Now, if we consider an ultrasound transducer positioned in a plane T in front of a homogeneous medium which is free of external sources, the transducer activity

can be regarded as a flux across the boundaries of the volume of interest. Furthermore, we define the volume of interest V to be an infinitely extending area bounded by the source plane T and a half-sphere of infinite radius with its center in the origin. In this case, the volume of interest does not contain any external sources and the first integral in Eq. 3.11 equals zero. To further simplify the above expression, we select the Green's function that satisfies the Neumann boundary conditions and has a zero-valued derivative, and assuming a perfectly baffled transducer, use its solution for a plane surface given by [75] (ch. 7, p. 366):

$$\acute{G}(\boldsymbol{r}|\boldsymbol{r_0}:\omega) = 2G(\boldsymbol{r}|\boldsymbol{r_0}:\omega) = \frac{e^{-jk|\boldsymbol{r}-\boldsymbol{r_0}|}}{2\pi|\boldsymbol{r}-\boldsymbol{r_0}|}, \tag{3.12}$$

$$\frac{\partial \acute{G}(\boldsymbol{r}|\boldsymbol{r_0}:\omega)}{\partial n} = 0. \tag{3.13}$$

Substituting the selected Green's function in the second integral in Eq. 3.11 and noticing that the normal outward velocity on the transducer surface $\mathcal{V}_n = \frac{\partial \Phi}{\partial t}$, Eq. 3.11 reduces to the Rayleigh integral over the transducer surface T:

$$\Phi(\boldsymbol{r}:\omega) = \int\limits_T \mathcal{V}_n(\boldsymbol{r_T}:\omega)\frac{e^{-jk|\boldsymbol{r}-\boldsymbol{r_T}|}}{2\pi|\boldsymbol{r}-\boldsymbol{r_T}|}d\boldsymbol{r_T}, \tag{3.14}$$

which relates the normal velocity profile generated by the transducer $\mathcal{V}_n(\boldsymbol{r_T}:\omega)$ to the resulting velocity potential field and can be rewritten in terms of the pressure field:

$$P(\boldsymbol{r}:\omega) = j\omega\rho \int\limits_T \mathcal{V}_n(\boldsymbol{r_T}:\omega)\frac{e^{-jk|\boldsymbol{r}-\boldsymbol{r_T}|}}{2\pi|\boldsymbol{r}-\boldsymbol{r_T}|}d\boldsymbol{r_T}. \tag{3.15}$$

The above equation is referred to as the Rayleigh integral. So far, we were considering wave propagation in lossless media. However, for media whose attenuation obeyes a power law frequency dependence, it can be introduced using a complex-valued wavenumber that is defined as [76]:

$$\tilde{k} = \frac{\omega}{c(\omega)} - j\alpha(\omega), \tag{3.16}$$

where $c(\omega)$ is the phase speed and $\alpha(\omega) = \alpha_0(\omega/2\pi)^n$ is the frequency-dependent attenuation coefficient. It should be noted that the power n in soft tissue is typically between 0 and 2. Furthermore, we assume that the dispersion effects are negligible over the considered frequency range, and thus the speed of sound

41

is presumed to be constant. This assumption simplifies the above complex-valued wavenumber expression to the following form:

$$\tilde{k} = \frac{\omega}{c} - j\alpha(\omega) = k - j\alpha(\omega). \tag{3.17}$$

Consequently, the incident pressure field in a medium with power-law attenuation effects can be described using a modified Green's function that is obtained by substituting the above expression for the wavenumber in Eq. 3.8 and can be written as:

$$\tilde{G}(\boldsymbol{r}|\boldsymbol{r_T}:\omega) = \acute{G}(\boldsymbol{r}|\boldsymbol{r_T}:\omega)e^{-\alpha(\omega)|\boldsymbol{r}-\boldsymbol{r_T}|}. \tag{3.18}$$

Finally, assuming the separability of the time and space variables of the vibration of the transducer surface, the normal velocity profile can be represented as a product of the transducer's spatial distribution function and the Fourier transform of the temporal component of the normal velocity, i.e. $\mathcal{V}_n(\boldsymbol{r_T}:\omega) = a_{Tx}(\boldsymbol{r_T}:\omega)\mathcal{V}_{n_0}(\omega)$. Defining the transmit impulse response function relating the harmonic normal velocity across the transducer surface to a resulting harmonic velocity potential field in any point in space as:

$$h_{Tx}(\boldsymbol{r}:\omega) = \int_T a_{Tx}(\boldsymbol{r_T}:\omega)\tilde{G}(\boldsymbol{r_T}|\boldsymbol{r}:\omega)d\boldsymbol{r_T}, \tag{3.19}$$

the expression for the incident harmonic pressure can be rewritten as:

$$\begin{aligned} P(\boldsymbol{r}:\omega) &= j\omega\rho\mathcal{V}_{n_0}(\omega)\int_T a_{Tx}(\boldsymbol{r_T}:\omega)\tilde{G}(\boldsymbol{r_T}|\boldsymbol{r}:\omega)d\boldsymbol{r_T} = \\ &= j\omega\rho\mathcal{V}_{n_0}(\omega)h_{Tx}(\boldsymbol{r}:\omega). \end{aligned} \tag{3.20}$$

3.2 Angular spectrum approach

The Rayleigh integral (Eq. 3.15) can be directly used to compute the pressure field, but requires dense spatial sampling which results in long computation times. Alternatively, wave propagation can be modeled by equivalent spatial impulse response methods(Eq. 3.20) [77]. However, the spatial impulse response method intrinsically assumes linear wave propagation in an acoustically homogeneous medium and would, therefore, limit the applicability of the proposed approach. As third option, the angular spectrum approach (ASA) can be used which can be extended to include nonlinear effects and to model pressure fields in layered (i.e. inhomogeneous) media [78–81]. This method makes
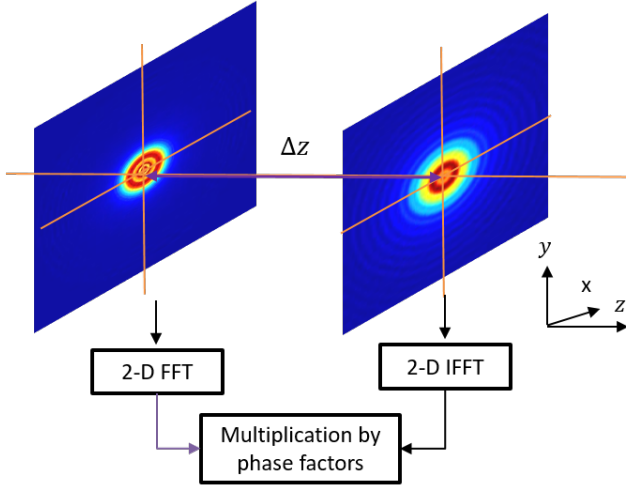
Figure 3.1: *Illustration of the principle of the ASA.*

use of a two-dimensional Fourier transform that decomposes the pressure field across the source plane into a spectrum of plane waves travelling in different directions away from the source. By means of a multiplication with an appropriate transfer function, each plane wave is propagated to a plane parallel to the source plane wherein they are recombined through the inverse Fourier transformation (Fig. 3.1).

In order to explain the concept of the ASA, we rewrite the expression for the incident pressure field (Eq. 3.20) in Cartesian coordinates, as:

$$P(x, y, z : \omega) = j\omega\rho\mathcal{V}_{n_0}(\omega)h_{Tx}(x, y, z : \omega). \qquad (3.21)$$

where z is the propagation direction.

The impulse response function h_T describes the forward propagation of the incident pressure field, which can be also modelled in the spatial frequency domain using the (ASA) [82]. Thereby, Eq. 3.21 can be rewritten as:

$$P(x, y, z : \omega) = j\omega\rho\mathcal{V}_{n_0}(\omega)\mathcal{F}_{2D}^{-1}\left\{H_{Tx}(k_x, k_y, z : \omega)\right\}, \qquad (3.22)$$

where $\mathcal{F}_{2D}^{-1}\{H\}$ denotes the inverse spatial 2-D Fourier transform of H, k_x and k_y are the spatial frequencies and H_{Tx} is the transmit transfer function that combines the spatial variance of the vibration profile of the transducer surface and the propagation effects and can be calculated as:

$$H_{Tx}(k_x, k_y, z) =$$
$$= A_{Tx}(k_x, k_y, : \omega) H_{Diffr}^{v_n \to \phi}(k_x, k_y, z : \omega) H_{Att}^{p \to p}(k_x, k_y, z : \omega). \tag{3.23}$$

The transmit aperture distribution function $A_{Tx}(k_x, k_y : \omega)$ is defined in a plane at $z = 0$, depends on the transducer type, geometry and transmit focal settings and can be determined by taking the 2-D Fourier transform of $a_{Tx}(x, y, z : \omega)$. The next two terms on the right side of the above equation model the effects of diffraction and attenuation, respectively, over a distance z and are given by [78, 80, 82]:

$$H_{Diffr}^{v_n \to \phi}(k_x, k_y, z : \omega) = \left(\frac{je^{jzk_z}}{k_z} \right)^*, \tag{3.24}$$

$$H_{Att}^{p \to p}(k_x, k_y, z : \omega) = e^{-\alpha \left(\frac{\omega}{2\pi} \right)^n z \frac{k}{k_z}}, \tag{3.25}$$

where "$*$" stands for the complex conjugate operator, and $k_z = \sqrt{k^2 - (k_x^2 + k_y^2)}$ can take complex values. The superscript "$v_n \to \phi$" specifies that the transfer function accounts for the conversion from the normal velocity to the velocity potential field, while the superscript "$p \to p$" indicates that the effect is modelled in terms of the pressure field.

3.2.1 Angular spectrum of a focused single-element transducer

The above method can be readily applied to compute the pressure field of a flat source. However, in clinical practice, transducers with curved apertures are often used to improve focusing. Modelling pressure fields from such sources requires additional procedures. At first, the transducer aperture is divided into a set of small nearly-planar sub-elements. The angular spectrum of each of these segments is calculated separately and is propagated to a preselected intermediate plane by means of a corresponding transfer function. Contributions from all sub-elements are added at the intermediate plane, forming a source angular spectrum that can be further propagated in a considered medium using conventional ASA.

As an example, we are considering the pressure field of a single-element focused transducer having a spherically curved aperture. The method for calculating the angular spectrum of such transducer was proposed by Vyas & Christensen in [83]. The procedure consists of dividing the transducer surface into a set of thin planar rings with a radius R_i and an arc width ΔR that fills the entire
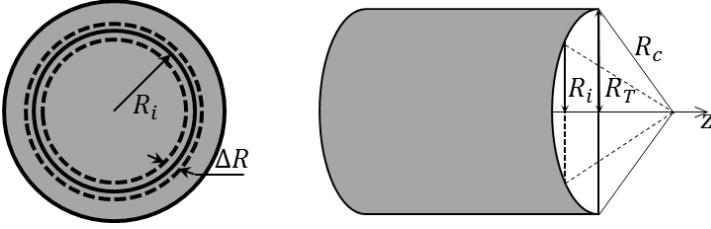
Figure 3.2: *Representation of a circular focused single-element transducer by a set of planar rings: top view (left) and cross-sectional view (right).*

transducer surface (Fig. 3.2). Each ring is contained within a plane parallel to a selected intermediate plane in front of the transducer. The angular spectrum of each ring is calculated separately as [83]:

$$A_i(k_x, k_y) = \int\limits_{S_i} a_i(x, y)e^{-j2\pi(k_x x + k_y y)}dxdy, \qquad (3.26)$$

or in spatial frequency polar coordinates:

$$A_i(\rho, \varphi) = \int\limits_{R_i - \frac{\Delta R}{2}}^{R_i + \frac{\Delta R}{2}} \int\limits_{0}^{2\pi} a_i(r, \theta)e^{-j2\pi\rho r cos(\theta - \varphi)}rdrd\theta. \qquad (3.27)$$

Assuming a uniform normal velocity distribution over the transducer surface and a very small width of the ring ($\Delta R \to 0$) we obtain [83]:

$$A_i(\rho, \varphi) = 2\pi R_i \Delta R J_0(2\pi\rho R_i), \qquad (3.28)$$

where J_0 is the Bessel function of first kind and zero order.

The angular spectrum of each ring is then propagated to the intermediate plane by multiplication with a corresponding transfer function:

$$H_i = \left(e^{j\Delta z_i k_z}\right)^*, \qquad (3.29)$$

where $\Delta z_i = \sqrt{R_c^2 - R_i^2} - \sqrt{R_c^2 - R_T^2}$ is the distance from the i$^{\text{th}}$ ring to the intermediate plane (Fig. 3.2b). The angular spectrum of the source in the intermediate plane ($z = 0$) is calculated by adding the contributions from all rings:
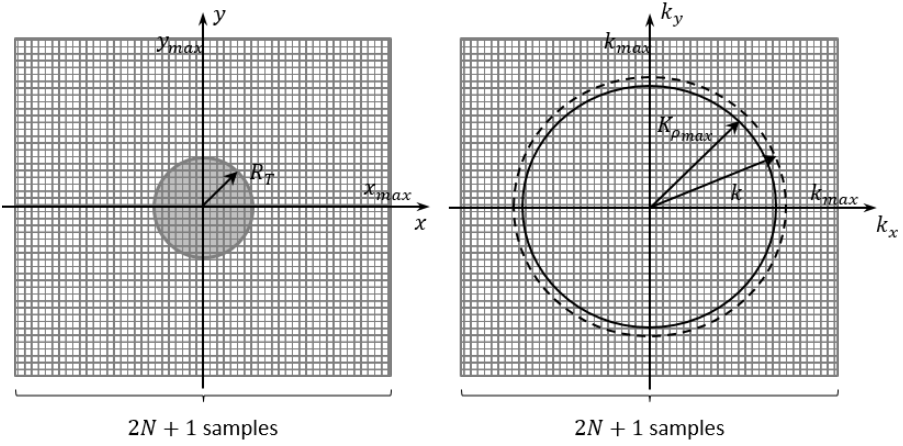
Figure 3.3: *Discretization of the intermediate plane in the spatial (left) and spatial-frequency domain (right).*

$$A_{Tx}(k_x, k_y : \omega) = \sum_{i=1}^{N_{rings}} A_i H_i, \qquad (3.30)$$

and the pressure distribution in any plane parallel to the intermediate plane can be calculated by substituting the above expression in Eq. 3.22 and 3.23.

3.2.2 Implementation details

Numerical implementation of the above described method begins with the selection of an appropriate spatial grid. The intermediate plane is discretized into a $(2N+1) \times (2N+1)$ grid with the same spatial sampling interval in both directions (Fig. 3.3):

$$\Delta x = \Delta y = \frac{\lambda}{2\xi} \qquad (3.31)$$

where λ is the wavelength of a particular harmonic and $\xi \geq 1$ is a sampling factor that guarantees respecting the Nyquist theorem.

The number of samples N should be chosen such that the maximal spatial coordinates $x_{max} = y_{max} = \lambda N/2\xi$, are several times larger than the dimensions of the transducer aperture. The size of the discretization grid N is kept constant for every harmonic frequency, while the size of the sampling interval, as can be
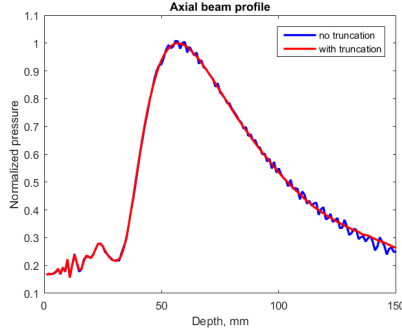
Figure 3.4: *Axial pressure beam profiles computed using the ASA with and without spatial frequency truncation.*

seen from Eq. 3.31, varies with frequency. The corresponding sampling interval in the spatial-frequency domain for a certain harmonic equals:

$$\Delta k = \frac{2\pi}{\Delta x(2N+1)} = \frac{2\xi k}{2N+1} \tag{3.32}$$

It should be noted that the real and imaginary part of the transfer function in Eq. 3.24 oscillates rapidly when $K_\rho = \sqrt{k_x^2 + k_y^2}$ approaches k, which leads to severe aliasing. In order to avoid aliasing due to inadequate sampling of the transfer function in this region, a so-called "spatial frequency truncation" was applied to the field at every propagation step [78,84,85]. This technique allows to reduce the aliasing without increasing the size of the computational grid. Truncation of the spatial frequency pressure distribution implies its multiplication with a two-dimensional radially-symmetric window. The radius of this window can be determined by considering the transfer function in Eq. 3.24 as a signal of K_ρ. In that case, the "instantaneous frequency" f_i of this signal is, by definition, the derivative of its phase, which equals zk_z and is given by [84]:

$$f_i = \frac{1}{2\pi} \frac{d}{dK_\rho} \left(z\sqrt{k^2 - K_\rho^2} \right) = -\frac{zK_\rho}{2\pi\sqrt{k^2 - K_\rho^2}}. \tag{3.33}$$

To meet the Nyquist criterion, the sampling frequency has to be at least two times higher than the frequency of the signal, i.e. $1/\Delta K_\rho \geq 2f_i$, so that:

$$\Delta K_\rho \leq \frac{\pi\sqrt{k^2 - K_\rho^2}}{zK_\rho}, \tag{3.34}$$

from which the radius of the truncation window can be determined as:

$$K_\rho \leq \frac{k}{\sqrt{1 + \left(\frac{z\Delta K_\rho}{\pi}\right)^2}}, \qquad (3.35)$$

where $\Delta K_\rho = \Delta\left(\sqrt{k_x^2 + k_y^2}\right) = \sqrt{2}\Delta k$ is the same when sampling in azimuthal and elevation directions. As can be seen from Eq. 3.33 and Eq. 3.35, when the distance z from the intermediate plane increases, the frequency of oscillation also increases and the truncation window becomes smaller. Fig. 3.4 presents the comparison of the axial pressure beam profiles computed with and without spatial frequency truncation.

3.2.3 Validation of the ASA implementation

The above described method was implemented in MATLAB (The MathWorks Inc., Natick, MA) and was validated through comparsion with Field II (freely-available simulation software based on the spatial impulse response method) [86]. Based on the linear systems theory, this simulation approach computes the emitted ultrasound field at a given spatial point as function of time using a convolution of the spatial impulse response with the excitation function. In pulse echo mode, the received signal is determined by convolving the transducer excitation function with the spatial impulse responses of the emitting and receiving apertures and the electromechanical impulse response of the transducer. Simulations can be performed for a wide range of transducer geometries and for any focal settings and apodization. However, Field II is limited to linear simulations in homogeneous media containing point scatterers.

For the comparison, the pressure field was modelled in a homogeneous medium with a speed of sound of 1540 m/s. A single-element transducer with a diameter of 12.7 mm, center frequency of 5 MHz and a radius of curvature of 75 mm was considered. In Field II, the "xdc-concave" function was used with a mathematical element size equal to half of the wavelength (0.15 mm). For the angular spectrum simulation, the surface of the transducer was divided into 42 planar rings of equal width (˜0.15 mm). A Gaussian-modulated sinusoidal pulse of 1.5 periods, 5 MHz center frequency and 80% relative bandwidth was generated in Field II and was used as an input for the angular spectrum simulations. Further, RMS pressure fields were compared between the simulators up to a depth of 150 mm with a 1 mm step. For both simulators, a sampling frequency of 100 MHz and a dense measurement grid of 1001×1001 samples with a sampling factor $\xi = 2$ were used (Eq. 3.31, 3.32). For the ASA simulations, a 1024-point fast Fourier transform was applied to a time-domain
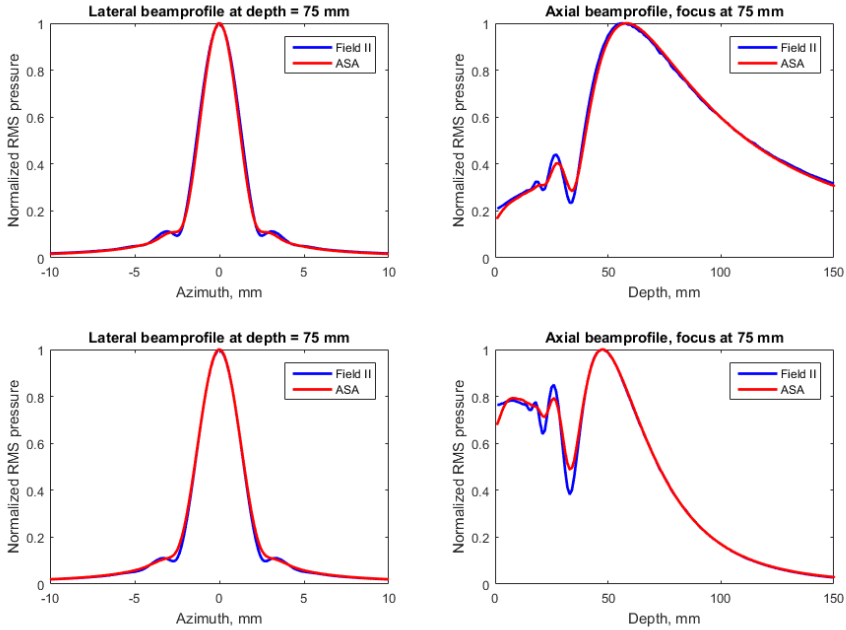
Figure 3.5: *Comparison of the simulated transmit beam profiles of a focused single-element transducer obtained with ASA and Field II: lateral (left) and axial (right). Upper row presents the beam profiles in a lossless medium, while the bottom row presents the beam profiles in a medium with attenuation (α =0.5 dB/cm/MHz). Transducer diameter 12.7 mm, focal depth 75 mm, center frequency 5 MHz, measurement depth 75 mm.*

pulse; the pressure field was simulated for non-zero frequency components of the spectrum and the spatial frequency truncation was applied as described in the previous subsection to avoid aliasing effects.

Comparison of the lateral and axial RMS beam profiles, wherein the former was simulated at the focal depth of the transducer, is presented in Fig. 3.5 (upper row). A very good agreement between the simulators can be observed, except for small discrepancies in the near-field of the transducer. The comparison of the (normalized) transmit RMS pressure fields is presented in Fig. 3.6 (upper row). Overall, the simulated pressure fields look very similar with a maximal percentage difference of normalized patterns below 6 %. Further, the simulated pressure fields were compared in the case when the effect of the frequency dependent attenuation was included in both simulators (Fig. 3.5 and Fig.

49
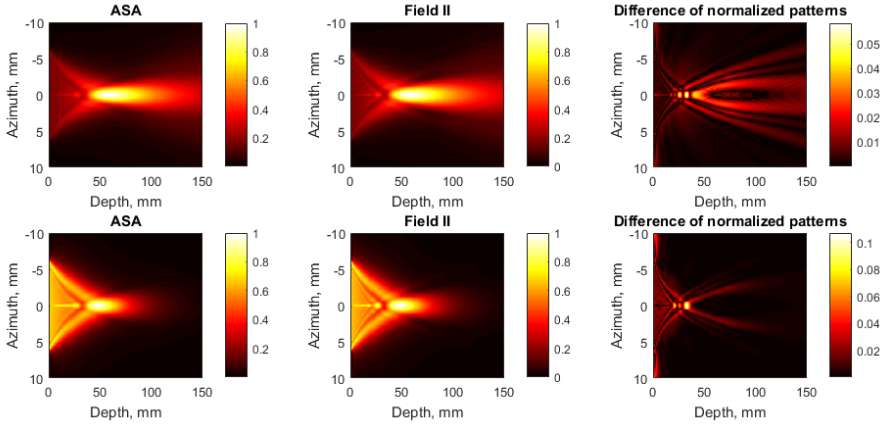
Figure 3.6: *Comparison of the simulated transmit pressure fields of a circular single-element focused transducer obtained with ASA and Field II in lossless (upper row) and attenuating (bottom row, α = 0.5 dB/cm/MHz) media. Transducer diameter 12.7 mm, focal depth 75 mm, center frequency 5 MHz, measurement range 1-150 mm.*

3.6 (lower row)). In Field II, this is done by modifying the impulse response function as described in [87]. An attenuation coefficient of 0.5 dB/cm/MHz was set in both simulators. Again, the simulated pressure fields look very similar except for an slightly increased difference in the near field around 10 %.

3.3 Acoustic scattering from tissue inhomogeneities

In this section, we will extend the above described theoretical formulations to consider scattering of acoustic waves in soft tissue. Similar to section 3.1, soft tissue is modelled as a fluid, however now it contains inhomogeneities with a density and compressibility differing from the background, i.e. scatterers. We assume that the size of such scatterers is small compared to the entire scattering volume and that the differences in the acoustic properties are small, so that the scattered waves are of small amplitude. In a medium with spatially varying density $\rho(\boldsymbol{r})$ and compressibility $\kappa(\boldsymbol{r})$, the wave equation for the total pressure field is given by [1] (ch. 4, p. 90):

$$\nabla^2 p - \frac{1}{c^2}\frac{\partial^2 p}{\partial t^2} = \gamma_\kappa(\boldsymbol{r})\frac{1}{c^2}\frac{\partial^2 p}{\partial t^2} + \nabla(\gamma_\rho(\boldsymbol{r})\nabla p), \qquad (3.36)$$

where

$$\gamma_\kappa(\boldsymbol{r}) = \frac{\kappa(\boldsymbol{r}) - \kappa_0}{\kappa_0},$$

$$\gamma_\rho(\boldsymbol{r}) = \frac{\rho(\boldsymbol{r}) - \rho_0}{\rho(\boldsymbol{r})},$$

(3.37)

and κ_0 and ρ_0 are the characteristics of the background medium, $c = \sqrt{1/\rho_0\kappa_0}$. After temporal Fourier transform, Eq. 3.36 becomes:

$$(\nabla^2 + k^2)P(\boldsymbol{r} : \omega) = -F(\boldsymbol{r} : \omega), \qquad (3.38)$$

which is the inhomogeneous Helmholtz equation, where the term on right side describes scattering due to fluctuations in compressibility and density:

$$F(\boldsymbol{r} : \omega) = k^2 \gamma_\kappa(\boldsymbol{r}) p(\boldsymbol{r} : \omega) - \nabla[\gamma_\rho(\boldsymbol{r}) \nabla P(\boldsymbol{r} : \omega)]. \qquad (3.39)$$

Noticing that in the frequency domain the pressure and velocity potential fields are related as:

$$P(\boldsymbol{r} : \omega) = j\omega\rho\Phi(\boldsymbol{r} : \omega), \qquad (3.40)$$

and taking the same steps as in section 1.1 (Eq. 3.6-3.10), we obtain an expression for the pressure field similar to that in Eq. 3.11:

$$P(\boldsymbol{r} : \omega) = \int_V F(\boldsymbol{r_0} : \omega)G(\boldsymbol{r}|\boldsymbol{r_0} : \omega)d\boldsymbol{r_0} +$$

$$+ \int_S \left[G(\boldsymbol{r}|\boldsymbol{r_0} : \omega)\frac{\partial P(\boldsymbol{r_0} : \omega)}{\partial n} - P(\boldsymbol{r_0} : \omega)\frac{\partial G(\boldsymbol{r}|\boldsymbol{r_0} : \omega)}{\partial n} \right] d\boldsymbol{r_0},$$

(3.41)

with S a surface enclosing the scattering volume and $\frac{\partial}{\partial n}$ denotes a partial derivative in the outward normal direction in the point $\boldsymbol{r_0}$ on the surface S.

Assuming that the background medium is unbounded, i.e. considering the surface volume to be a sphere of a very large radius, it can be shown that the surface integral equals the incident pressure wave P_i [1, 71], and noticing the the total pressure at a given location $\boldsymbol{r}$ is the sum of the incident and the scattered pressure fields: $P = P_s + P_i$, the scattered pressure field can be expressed as:

$$P_s(\boldsymbol{r} : \omega) = \int\limits_V F(\boldsymbol{r_0} : \omega) G(\boldsymbol{r}|\boldsymbol{r_0} : \omega) d\boldsymbol{r} =$$

$$= \int\limits_V \Big[k^2 \gamma_\kappa(\boldsymbol{r_0}) P(\boldsymbol{r_0} : \omega) + \nabla_0 (\gamma_\rho(\boldsymbol{r_0}) \nabla P(\boldsymbol{r_0} : \omega)) \Big] G(\boldsymbol{r}|\boldsymbol{r_0} : \omega) d\boldsymbol{r_0},$$

(3.42)

where ∇_0 is the gradient in $\boldsymbol{r_0}$. The second term in this integral can be rewritten as:

$$\int\limits_V G(\boldsymbol{r}|\boldsymbol{r_0} : \omega) \nabla_0 \Big[\gamma_\rho \nabla_0 P(\boldsymbol{r_0} : \omega) \Big] d\boldsymbol{r_0} =$$

$$= \int\limits_V \nabla_0 \Big[G(\boldsymbol{r}|\boldsymbol{r_0} : \omega) \gamma_\rho \nabla_0 P(\boldsymbol{r_0} : \omega)) \Big] d\boldsymbol{r_0} -$$

(3.43)

$$- \int\limits_V \gamma_\rho \nabla_0 P(\boldsymbol{r_0} : \omega) \nabla_0 G(\boldsymbol{r}|\boldsymbol{r_0} : \omega) d\boldsymbol{r_0},$$

wherein the first volume integral on the right hand side of the above expression can be converted to a surface integral using the Gauss theorem [1] (ch. 4, p. 93). However, since the volume of interest V was chosen large enough to neglect the pressure flux across its boundary S, the surface integral vanishes and the scattered pressure field can be written as:

$$P_s(\boldsymbol{r} : \omega) = \int\limits_V \Big(k^2 \gamma_\kappa(\boldsymbol{r_0}) P(\boldsymbol{r_0} : \omega) G(\boldsymbol{r}|\boldsymbol{r_0} : \omega) +$$

$$+ \gamma_\rho(\boldsymbol{r_0}) \nabla_0 P(\boldsymbol{r_0} : \omega) \nabla_0 G(\boldsymbol{r}|\boldsymbol{r_0} : \omega) \Big) d\boldsymbol{r_0}.$$

(3.44)

The above expression is often referred to as "scattering equation" [71] (ch. 5, p. 287). It can be noticed, that the scattered pressure field is expressed in terms of the total pressure field P which is not known, and therefore, some simplifying assumptions have to be made to evaluate the above integral. First of all, we assume that the scattering in tissue is weak (Born approximation). This implies that the incident wave does not significantly decrease in amplitude during its propagation ($P \approx P_i$). Thus, the total pressure in above equation can be replaced by the incident pressure field. Further, using Eq. 3.40, the gradient of the incident pressure can be expressed as:

$$\nabla P_i(\boldsymbol{r} : \omega) = j\omega\rho\nabla\Phi_i(\boldsymbol{r} : \omega) = -j\omega\rho\mathbf{V_i}(\boldsymbol{r} : \omega) = -jk\rho c\mathbf{V_i}(\boldsymbol{r} : \omega), \quad (3.45)$$

with $\mathbf{V}_i(\boldsymbol{r}:\omega)$ - the harmonic particle velocity vector field.

The gradient of the Green's function can be expressed as:

$$\nabla_0 G(\boldsymbol{r}|\boldsymbol{r_0}:\omega) = G(\boldsymbol{r}|\boldsymbol{r_0}:\omega)\frac{1+jk|\boldsymbol{r}-\boldsymbol{r_0}|}{|\boldsymbol{r}-\boldsymbol{r_0}|}\boldsymbol{e_s}(\boldsymbol{r_0},\boldsymbol{r}), \tag{3.46}$$

where $\boldsymbol{e_s}(\boldsymbol{r_0},\boldsymbol{r})$ is a unit vector pointing from the scattering point $\boldsymbol{r_0}$ to the receiver point $\boldsymbol{r}$. When the receiver point is far from the scattering point with regard to the wave number ($|\boldsymbol{r}-\boldsymbol{r_0}| \gg k$) Eq. 3.46 is reduced to:

$$\nabla_0 G(\boldsymbol{r}|\boldsymbol{r_0}:\omega) = jkG(\boldsymbol{r}|\boldsymbol{r_0}:\omega)\boldsymbol{e_s}(\boldsymbol{r_0},\boldsymbol{r}). \tag{3.47}$$

Substituting Eq. 3.45 and 3.47 in Eq. 3.44, we obtain:

$$P_s(\boldsymbol{r}:\omega) = k^2 \int\limits_V \Big(\gamma_\kappa(\boldsymbol{r_0})\times$$
$$\times P_i(\boldsymbol{r_0}:\omega) + \rho c\gamma_\rho(\boldsymbol{r_0})\mathbf{V}_i(\boldsymbol{r}:\omega)\boldsymbol{e_s}(\boldsymbol{r_0},\boldsymbol{r})\Big)G(\boldsymbol{r}|\boldsymbol{r_0}:\omega)d\boldsymbol{r_0}. \tag{3.48}$$

This equation can be further simplified assuming a planar incoming wave with a propagation direction $\boldsymbol{e_I}$, thus obtaining:

$$P_i(\boldsymbol{r}:\omega) = P_i(\omega)e^{-jk\boldsymbol{e_I}\boldsymbol{r}}, \tag{3.49}$$

$$\nabla P_i(\boldsymbol{r}:\omega) = -jkP_i(\boldsymbol{r}:\omega)\boldsymbol{e_I}, \tag{3.50}$$

and Eq. 3.48 reduces to:

$$P_s(\boldsymbol{r}:\omega) = k^2 \int\limits_V \gamma(\boldsymbol{r_0},\boldsymbol{r})p_i(\boldsymbol{r_0}:\omega)G(\boldsymbol{r}|\boldsymbol{r_0}:\omega)d\boldsymbol{r_0}, \tag{3.51}$$

where $\gamma(\boldsymbol{r_0},\boldsymbol{r}) = \gamma_\kappa(\boldsymbol{r_0}) + \gamma_\rho(\boldsymbol{r_0})\boldsymbol{e_I}\boldsymbol{e_s}(\boldsymbol{r_0},\boldsymbol{r})$ can be seen as an inhomogeneity coefficient in $\boldsymbol{r_0}$ experienced by the point in $\boldsymbol{r}$. As in the previous subsection, the Green's function can be replaced by its modified form (Eq. 3.18) to account for attenuation.

3.4   Detected echo signal

Considering the receiving transducer as a linear temporal-spatial filter the temporal spectrum of the detected electrical signal by the transducer can be approximated as:

$$S_{Rx}(\omega) = \text{w}_{Rx}(\omega) \int\limits_T a_{Rx}(\boldsymbol{r_T} : \omega) P_s(\boldsymbol{r_T} : \omega) d\boldsymbol{r_T}, \qquad (3.52)$$

where w_{Rx} is electromechanical transfer function of the receiving transducer and a_{Rx} - its spatial distribution function and the integration is done over the transducer surface T.

Substituting Eq. 3.51 in Eq. 3.52, we obtain:

$$S_{Rx}(\omega) = \text{w}_{Rx}(\omega) k^2 \int\limits_V P_i(\boldsymbol{r_0} : \omega) \times$$

$$\int\limits_T \gamma(\boldsymbol{r_0}, \boldsymbol{r_T}) a_{Rx}(\boldsymbol{r_T} : \omega) \tilde{G}(\boldsymbol{r_T} | \boldsymbol{r_0} : \omega) d\boldsymbol{r_T} d\boldsymbol{r_0}. \qquad (3.53)$$

When the transducer radius is small compared to its distance to the scattering site $(\boldsymbol{r_0} \gg \boldsymbol{r_T})$, the receive unit vector $\boldsymbol{e_s}(\boldsymbol{r_0}, \boldsymbol{r_T})$ is approximately the same for all points $\boldsymbol{r_T}$ on the transducer surface: $\boldsymbol{e_s}(\boldsymbol{r_0}, \boldsymbol{r_T}) = \boldsymbol{e_s}(\boldsymbol{r_0})$ and therefore: $\gamma(\boldsymbol{r_0}, \boldsymbol{r_T}) = \gamma(\boldsymbol{r_0})$.

Similar to Eq. 3.19, we define the receive impulse response function as:

$$h_{Rx}(\boldsymbol{r_0} : \omega) = \int\limits_T a_{Rx}(\boldsymbol{r_T} : \omega) \tilde{G}(\boldsymbol{r_T} | \boldsymbol{r_0} : \omega) d\boldsymbol{r_T}, \qquad (3.54)$$

yielding:

$$S_{Rx}(\omega) = \text{w}_{Rx}(\omega) k^2 \int\limits_V \gamma(\boldsymbol{r_0}) P_i(\boldsymbol{r_0} : \omega) h_{Rx}(\boldsymbol{r_0} : \omega) d\boldsymbol{r_0}. \qquad (3.55)$$

Finally, combining Eq. 3.55 with Eq. 3.20 and assuming a planar incoming wave, we obtain the expression for the received signal spectrum:

$$S_{Rx}(\omega) = j\rho c \mathcal{V}_{n_0}(\omega) k^3 \int\limits_V \gamma(\boldsymbol{r_0}) h_{Tx}(\boldsymbol{r_0} : \omega) h_{Rx}(\boldsymbol{r_0} : \omega) d\boldsymbol{r_0}, \qquad (3.56)$$

where the temporal component of the normal velocity $\mathcal{V}_{n_0}$ on the surface of the transmitting transducer can also be expressed as a product of the electrical excitation $S_{Tx}(\omega)$ of the transmitting transducer and its electro-mechanical transfer function $\mathrm{w}_{Tx}(\omega)$. Defining

$$S_{Tx,Rx}(\omega) = S_{Tx}(\omega)\mathrm{w}_{Tx}(\omega)\mathrm{w}_{Rx}(\omega), \tag{3.57}$$

we obtain the final expression for the spectrum of the scattered signal detected by the transducer:

$$S_{Rx}(\omega) = j\rho c S_{Tx,Rx}(\omega)k^3 \int\limits_{V} \gamma(\boldsymbol{r_0})h_{Tx}(\boldsymbol{r_0}:\omega)h_{Rx}(\boldsymbol{r_0}:\omega)d\boldsymbol{r_0}. \tag{3.58}$$

3.5   Power spectrum

The average power spectrum of the echo scattered by the medium containing a random distribution of scatterers is defined as [88]:

$$\mathcal{P}(\omega) = \langle |S_{Rx}(\omega)|^2 \rangle = \rho^2 c^2 |S_{Tx,Rx}(\omega)|^2 k^6 \times$$

$$\times \int\limits_{V} \int\limits_{V(\boldsymbol{r_0})} \langle \gamma(\boldsymbol{r_0})\gamma(\boldsymbol{r_0}+\Delta\boldsymbol{r}) \rangle h_{Tx}(\boldsymbol{r_0}:\omega)h_{Tx}^*(\boldsymbol{r_0}+\Delta\boldsymbol{r}:\omega)\times \tag{3.59}$$

$$\times h_{Rx}(\boldsymbol{r_0}:\omega)h_{Rx}^*(\boldsymbol{r_0}+\Delta\boldsymbol{r}:\omega)d\boldsymbol{r_0}d\Delta\boldsymbol{r},$$

where $\langle \cdot \rangle$ represents the ensemble average and "$*$" denotes the complex conjugate and $V(\boldsymbol{r_0}) = V - \boldsymbol{r_0}$. The inhomogeneity coefficient $\gamma(\boldsymbol{r_0})$ describing the distribution of scatterers is a random function of position $\boldsymbol{r_0}$, while the transmit and receive impulse response functions h_{Tx} and h_{Rx} are deterministic, and therefore were taken outside of the ensemble averaging operation. It should be noted that the ensemble average $\langle \gamma(\boldsymbol{r_0})\gamma(\boldsymbol{r_0}+\Delta\boldsymbol{r}) \rangle$ differs from zero only in a small area around $\boldsymbol{r_0}$. Thus, we can go from integrating over the volume $V(\boldsymbol{r_0})$ to integrating over the entire space. Furthermore, in a first-order approximation, we can express $h_{Tx}(\boldsymbol{r_0}+\Delta\boldsymbol{r}:\omega) \approx h(\boldsymbol{r_0}:\omega)\epsilon(\Delta r,\omega)$, where $\epsilon(\Delta r,\omega)$ is a frequency-dependent correction coefficient. Thereby, Eq. 3.59 reduces to:

$$\mathcal{P}(\omega) = \rho^2 c^2 |S_{Tx,Rx}(\omega)|^2 k^6 \int\limits_{V} \int\limits_{-\infty}^{\infty} \langle \gamma(\boldsymbol{r_0})\gamma(\boldsymbol{r_0}+\Delta\boldsymbol{r}) \rangle \times \tag{3.60}$$

$$\times \epsilon(\Delta r,\omega)h_{Tx}^2(\boldsymbol{r_0}:\omega)h_{Rx}^2(\boldsymbol{r_0}:\omega)d\boldsymbol{r_0}d\Delta\boldsymbol{r}.$$

Further, we assume that the scattering process is weakly stationary over space, i.e. the average value $\langle \gamma(\boldsymbol{r_0}) \gamma(\boldsymbol{r_0} + \Delta \boldsymbol{r}) \rangle$ does not depend on the spatial locations from which the signal is recorded but only on the distance between these spatial points $\Delta \boldsymbol{r}$ [1, 89]. Therefore, we can rewrite the above expression as:

$$
\mathcal{P}(\omega) = \rho^2 c^2 |S_{Tx,Rx}(\omega)|^2 k^6 \int\limits_V h_{Tx}^2(\boldsymbol{r_0} : \omega) h_{Rx}^2(\boldsymbol{r_0} : \omega) \times
$$

$$
\times \int\limits_{-\infty}^{\infty} R_\gamma(\Delta \boldsymbol{r}) \epsilon(\Delta r, \omega) d\Delta r d\boldsymbol{r_0}, \tag{3.61}
$$

where $R_\gamma(\Delta \boldsymbol{r}) = \langle \gamma(\boldsymbol{r_0}) \gamma(\boldsymbol{r_0} + \Delta \boldsymbol{r}) \rangle$ is the autocorrelation functions of the scattering process, which can be further expanded to its average and fluctuating components [89].

$$
R_\gamma(\Delta \boldsymbol{r}) = |\langle \gamma \rangle|^2 + \langle |\gamma - \langle \gamma \rangle|^2 \rangle c_\gamma(\Delta \boldsymbol{r}), \tag{3.62}
$$

with $c_\gamma(\Delta \boldsymbol{r})$ - the correlation coefficient that describes the similarity of the acoustic properties at 2 locations inside of the scattering volume which are separated by the distance Δr [1]. The form of the correlation coefficient is determined by the size, geometry and elastic properties of the inhomogeneities [1]. The first term on the right side of the above expression corresponds to the coherent scattering component, which is negligible under the assumption of random and isotopic scattering [1, 88, 89]. The second term describes the incoherent scattering, which will be considered in the following discussion. Assuming independent scatterers, the variance of the scattering process can be rewritten as: $\langle |\gamma - \langle \gamma \rangle|^2 \rangle = \gamma_0^2 \bar{n} V_s$, with γ_0^2 - the mean-square inhomogeneity coefficient, $\bar{n}$ - the average number of scatterers per unit volume, and V_s - the effective scatterer volume [1, 89]. Therefore, the average power spectrum of an incoherent scattered signal can be expressed as:

$$
\mathcal{P}(\omega) = \gamma_0^2 \bar{n} V_s \rho^2 c^2 |S_{Tx,Rx}(\omega)|^2 k^6 \times
$$

$$
\times \int\limits_V h_{Tx}^2(\boldsymbol{r_0} : \omega) h_{Rx}^2(\boldsymbol{r_0} : \omega) \int\limits_{-\infty}^{\infty} c_\gamma(\Delta \boldsymbol{r}) \epsilon(\Delta r, \omega) d\Delta r d\boldsymbol{r_0}. \tag{3.63}
$$

As can be seen from the above expression, the correction coefficient $\epsilon(\Delta r, \omega)$ defines the frequency-dependence of the scattering process. This frequency dependence vanishes in the case of point scatterers. However, for the scatterers

of finite size, the correction coefficient is decreasing with frequency for $ka \leq 1$ (with a - the size of the scatterer).

As an example, a homogeneous lossless medium will be considered, where the correction coefficient can be expressed as $\epsilon(\Delta r, \omega) = e^{-j2k\Delta r}$ and accounts solely for the effect of diffraction. It should be noted, that even if the assumption of a lossless medium is neglected, the effect of attenuation would be negligible at such small scale Δr. In the special case of Rayleigh scattering ($ka \ll 1$), the factor $e^{-j2k\Delta r} \approx 1$ for small Δr, and the integral $\int c_\gamma(\Delta \boldsymbol{r}) e^{-j2k\Delta r} d\Delta \boldsymbol{r}$ reduces to $\int c_\gamma(\Delta \boldsymbol{r}) d\Delta \boldsymbol{r} = V_s$, yielding:

$$\mathcal{P}_{Rayl}(\omega) = \gamma_0^2 \bar{n} V_s^2 \rho^2 c^2 |S_{Tx,Rx}(\omega)|^2 k^6 \int_V h_{Tx}^2(\boldsymbol{r_0} : \omega) h_{Rx}^2(\boldsymbol{r_0} : \omega) d\boldsymbol{r_0}. \quad (3.64)$$

The frequency dependence for scatterers of finite-size can be introduced using the so-called form-factor. Essentially, the form-factor is an analogue of the correlation coefficient in the spatial-frequency domain and is defined as the ratio of the backscatter coefficient of a considered medium to that of a medium containing point scatterers [89]:

$$F(\omega) = \frac{\sigma}{\sigma_{Rayl}} = \frac{\mathcal{P}(\omega)}{\mathcal{P}_{Rayl}(\omega)}. \quad (3.65)$$

Therefore, Eq. 3.63 can be rewritten as:

$$\mathcal{P}(\omega) = \gamma_0^2 \bar{n} V_s \rho^2 c^2 |S_{Tx,Rx}(\omega)|^2 k^6 F(\omega) \int_V h_{Tx}^2(\boldsymbol{r_0} : \omega) h_{Rx}^2(\boldsymbol{r_0} : \omega) d\boldsymbol{r_0}. \quad (3.66)$$

The form factors for three simple scatterer models that are widely used in the literature are given in [89].

3.5.1 Comparison with Field II

The validity of the derived expression for the power spectrum of the scattered signal can be demonstrated through comparison with Field II. For this purpose a set of scattered signals was generated for the same characteristics of the transducer and the input signal as in section 3.2.3. The dataset consisted of 20 RF lines that were generated from blocks of 40 mm × 40 mm × 40 mm with random distribution of point scatterers. The signals were gated with a 4 mm long Hanning window at thee different depths: at 40 mm (near-field), at
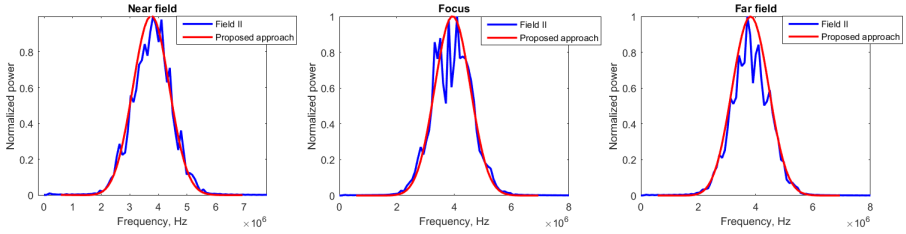
Figure 3.7: *Comparison of power spectra predicted using Eq. 3.64 to those calculated for the signals generated in Field II assuming a lossless medium. The signals were gated around 40 mm (left), 75 mm (middle) and 110 mm (right). Transducer diameter 12.7 mm, focal depth 75 mm, center frequency 3.5 MHz.*

75 mm (focus) and at 110 mm (far-field). The power spectrum of each gated segment was calculated by averaging 20 Fourier transformed windowed signals of each data set:

$$\mathcal{P}_{FieldII}(\omega) = \frac{1}{20} \sum_{i=1}^{20} \left| \mathcal{F} \left\{ RF(t) \mid_{t_1 \le t \ge t_2} \right\} \right|^2. \qquad (3.67)$$

where $RF(t)$ is the signal generated in Field II and $t_1 \le t \ge t_2$ is the gated time interval corresponding to the above described window. Further, a power spectrum of the scattered signals gated around the 3 specified depths was simulated according to Eq. 3.64 using the parameters of the Field II simulations as an input. Fig. 3.7 presents the comparison of the power spectra of the signals generated in Field II and those estimated using Eq. 3.64 at 40 mm, 75 mm and 110 mm. An excellent agreement between Field II and the proposed model can be observed.

Chapter 4

Diffraction - independent ultrasound attenuation estimation. Part I

This work was submitted for a publication in a peer-reviewed journal.

Abstract

The ultrasound attenuation coefficient has shown potential to provide quantitative information on the pathological state of soft tissues. However, its estimation in practice is limited by a number of factors. The main difficulty consists in the need for diffraction correction which is currently done by means of a reference measurement. In this chapter, we present an alternative attenuation estimation algorithm that accounts for the effects of diffraction and only requires a single transducer calibration. The proposed method estimates the attenuation by repeatedly solving the forward wave propagation problem and by iteratively matching the simulated signals to the measured ones. The simulation procedure encompasses explicit modelling of the diffraction effects and allows to avoid several assumptions made by conventional methods. The performance of the attenuation reconstruction method was validated on both synthetic and experimental data. In the simulation study, the proposed method allowed estimating the true attenuation coefficient of the generated authentic signals regardless of the position of the phantom with respect to the transducer focus. In the experimental study, the method provided attenuation estimates close to the "ground-truth" attenuation values both in the focal zone of the transducer as well as in the far-field with an average relative error of about 10 %. The obtained results demonstrate the ability of the method to provide diffraction-independent attenuation estimates.

4.1   Introduction

Estimation of the acoustic attenuation is of great interest in ultrasound tissue characterization. The potential of this parameter to provide information about the pathological state of tissues has been shown by many authors [6, 12, 14, 21, 90, 91]. Moreover, correct attenuation compensation is very important in the process of B-mode image formation as well as for the estimation of other acoustic parameters (e.g. backscatter coefficient) [43–45, 92]. A variety of techniques have been proposed for attenuation estimation from reflected ultrasound signals. Most of these techniques solve the so-called "inverse scattering problem" by estimating the attenuation characteristics directly from the recorded backscatter signals. This implies that other acoustic effects that may influence the attenuation estimate have to be corrected for, or otherwise neglected under certain assumptions. A critical step in determining the attenuation coefficient is diffraction correction. Without diffraction correction, biased attenuation estimates are obtained in different parts of the ultrasound beam [54]. In order to minimize the bias in the estimation of the acoustic attenuation, researchers have been performing measurements in the focal zone of the

sound beam where diffraction effects on attenuation estimates are negligible, or have attempted to determine a correction factor experimentally.

The most common approach for diffraction correction is a reference phantom technique, as proposed by Yao et al. [41, 93], that consists in comparing backscattered signals from a sample to those of a reference tissue-mimicking phantom with known acoustic properties. Although this method presents a relatively straightforward procedure to correct for diffraction effects, its use in clinical practice is limited due to a number of constraints. First of all, the reference measurement has to be repeated every time the system settings (e.g. focal settings) are changed. Furthermore, it is assumed that the expected speed of sound in tissue is approximately the same as in the reference phantom, and that it is constant, which is not always the case [94].

In chapter 2, we described an alternative approach for attenuation estimation, wherein the forward scattering problem was repeatedly solved through computer simulations for a varying input attenuation coefficient in order to match synthetically generated backscattered signals to experimentally observed ones. The attenuation coefficient corresponding to the highest similarity between the simulated and the measured signals was considered to be the true parameter of the investigated medium. Feasibility of the proposed method was tested assuming plane wave propagation. In the present chapter, we overcome this limitation by including diffraction effects into the simulation procedure and validate the method on both simulated data and on data recorded in tissue-mimicking phantoms. To demonstrate that the method provides attenuation estimates independent of diffraction effects, its performance is tested at different depths along a focused ultrasound beam. The influence of diffraction effects is also investigated by comparing the attenuation estimates obtained with and without diffraction correction.

4.2   Methods

In this section, we will use the expression for the power spectrum of the scattered signal which was derived in the previous chapter. Estimation of the power spectrum requires modelling of the forward and backward propagation of the acoustic waveform between the source and the scattering site, which can be accomplished using the angular spectrum approach. Further, a power spectrum of the scattered signal is estimated for a varying attenuation input and is compared to the power spectra determined for the experimentally observed signals at different depths.

4.2.1 Power spectrum of the echo signal

Consider the expression for the power spectrum obtained in the previous chapter under the assumption of Rayleigh scattering:

$$\mathcal{P}_{Rayl}(\omega) = \gamma_0^2 \bar{n} V_s^2 \rho^2 c^2 |S_{Tx,Rx}(\omega)|^2 k^6 \int\limits_V h_{Tx}^2(\boldsymbol{r_0} : \omega) h_{Rx}^2(\boldsymbol{r_0} : \omega) d\boldsymbol{r_0}. \quad (4.1)$$

where γ^2 is the mean-square inhomogeneity coefficient, $\bar{n}$ is the average number of scatterers per unit volume, V_s - is the effective scatterer volume, $k = \omega/c$ is the wavenumber and ρ and c are the density and speed of sound, respectively. $S_{Tx,Rx}(\omega)$ is defined by Eq. 3.58 and h_{Tx} and h_{Rx} are the transmit and receive impulse response functions defined in Eq. 3.19 and Eq. 3.54, and the integral is taken over the scattering volume V. For simplicity, the subscript "*Rayl*" is further omitted. The product of the constants in Eq. 4.1 can be replaced by the factor $C = \gamma_0^2 \bar{n} V_s^2 \rho^2/c^4$, yielding:

$$\mathcal{P}(\omega) = C |S_{Tx,Rx}(\omega)|^2 \omega^6 \int\limits_V h_{Tx}^2(\boldsymbol{r_0} : \omega) h_{Rx}^2(\boldsymbol{r_0} : \omega) d\boldsymbol{r_0}. \quad (4.2)$$

4.2.2 Numerical implementation

The impulse response functions h_{Tx} and h_{Rx} in the above equation describe the forward and backward propagation of the pressure field between the source and the scattering site and will further be modelled using the angular spectrum approach (ASA). The resulting field is usually computed in the spatial-frequency domain by means of the transfer functions H_{Tx} and H_{Rx} that can be obtained through a spatial 2-D Fourier transform of the impulse response functions [78, 80].

Provided that the pressure or normal velocity distribution is defined in the initial plane (at $z = 0$), ASA computes pressure fields in successive parallel planes. Further, we assume that the dimensions of a scattering medium are significantly larger than transducer aperture, (i.e. no reflections coming from edges of the scattering medium), and, instead of considering the entire scattering volume, we examine scattering contributions from thin sub-volumes parallel to the initial plane (Fig. 4.1). In this way, the power spectrum of the scattered signal, corresponding to a gated region around depth z can be computed as:

$$\mathcal{P}(\omega, z) = C|S_{Tx,Rx}(\omega)|^2 \omega^6 \int\limits_{S} \left[\mathcal{F}_{2D}^{-1}\left\{H_{Tx}(k_x, k_y, z : \omega)\right\}\right]^2 \times$$

$$\times \left[\mathcal{F}_{2D}^{-1}\left\{H_{Rx}(k_x, k_y, z : \omega)\right\}\right]^2 dx dy, \tag{4.3}$$

where the integration to be performed over a plane parallel to the transducer at depth z. In Eq. 4.3, k_x and k_y are the spatial frequencies, whereas H_{Tx} and H_{Rx} are the transmit and receive transfer functions defined in the spatial-frequency domain. $\mathcal{F}_{2D}^{-1}\{H\}$ denotes the inverse spatial 2-D Fourier transform of H.

For a homogeneous medium, the transmit and receive transfer functions in Eq. 4.3 are defined as:

$$H_{Tx/Rx}(k_x, k_y, z : \omega) = A_{Tx/Rx}(k_x, k_y : \omega) H_{Diffr}^{v_n \to \varphi}(k_x, k_y, z : \omega) \times$$

$$\times H_{Att}^{p \to p}(k_x, k_y, z : \omega). \tag{4.4}$$

The first factor on the right side of Eq. 4.4 represents the transducer's spatial weighting function that is defined in a plane at $z = 0$ and which depends on the transducer type, geometry and focal settings. In the present study, we consider a focused single-element transducer, both for transmission and reception. A procedure for calculating the weighting function of this type of source was described in chapter 3 (Eq. 3.30). Since the focal depth of this transducer is determined by its curvature and is the same for both transmission and reception, the transmit and receive weighting functions and are identical in the present case. The second and third factors on the right side model the effects of diffraction and attenuation over a distance z, respectively, that were defined in Eq. 3.24 and Eq. 3.25 of chapter 3, respectively.

When considering multilayered media, the effects of diffraction and attenuation are computed separately in every layer using the corresponding sub-functions. In addition, at the interface between subsequent layers (indexed "i" and "i+1"), the following transmission coefficient is introduced [71]:

$$T_{i|i+1}^{p \to p} = \frac{2Z_{i+1}cos(\theta_i)}{Z_i cos(\theta_{i+1}) + Z_{i+1}cos(\theta_i)}, \tag{4.5}$$

where $Z = \rho c$ is the acoustic impedance and θ_i and θ_{i+1} are the incident angles of each plane wave in the angular spectrum with the normal to the interface between the layers above and beneath the interface:

$$\theta_i = sin^{-1}\left(\frac{\sqrt{k_x^2 + k_y^2}}{k_i}\right),$$

$$\theta_{i+1} = sin^{-1}\left(\frac{\sqrt{k_x^2 + k_y^2}}{k_{i+1}}\right). \tag{4.6}$$

It should be noted that the normal velocity to velocity potential conversion is required only once, in the first propagation layer, while in subsequent layers diffraction can be modelled in terms of pressure using the following subfunction:

$$H_{Diffr}^{p \to p}(k_x, k_y, z : \omega) = \left(e^{jk_z z}\right)^*, \tag{4.7}$$

where, we recall, $k_z = \sqrt{k^2 - (k_x^2 + k_y^2)}$.

The above formulas allow to compute the power spectrum of a signal scattered from a region around a certain depth. The input acoustic parameters required for the simulations such as density, speed of sound and thickness of each layer are assumed to be known, whereas the attenuation coefficient in the model can be varied within acceptable bounds to match the experimentally observed signals as will be described below. If the electrical excitation of the transducer as well as its transmit and receive transfer functions are known, the temporal function $|S_{Tx,Rx}|$ can be simply calculated as their product. In the other case, $|S_{Tx,Rx}|$ can be determined experimentally through a reflector measurement as described in App. B.

4.2.3 Attenuation estimation algorithm

The proposed algorithm for the attenuation estimation consists of three main steps. First, the power spectrum of the signal received at the transducer site is calculated using Eq. 4.3 for an initial estimate of the attenuation coefficient and with known acoustic parameters and transducer characteristics. Next, the simulated power spectra and power spectra determined for the experimentally observed signals gated in the region of interest (ROI) are compared using a pre-defined similarity measure. Finally, the first two steps are repeated for a series of values of a varying input attenuation coefficient, considering all other input parameters to be constant, and the attenuation coefficient corresponding to the highest similarity between the spectra is determined.

The simulated power spectra are compared to the power spectra of the experimentally observed backscattered signals using a sliding window approach. The
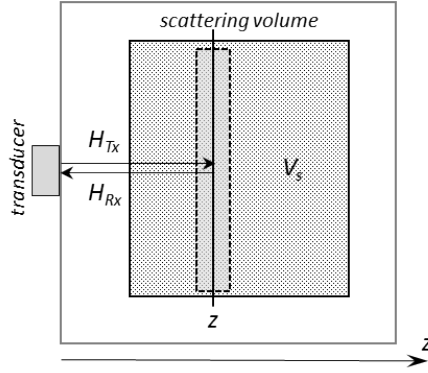
Figure 4.1: *Schematic representation of the simulation set-up.*

first window is used for calibration, wherein the energies of the simulated and measured spectra are equalized. In this way, the unknown amplitude coefficient C in Eq. 4.3 can be eliminated. After the calibration, the similarity between the simulated and measured power spectra in every window is assessed using the least squares difference of the spectra centered at depth z. In order to reduce the amplitude variations of the compared spectra, the spectral distance is computed for the square root of power spectra:

$$D(z, \alpha) = \sum_{\omega} \left(\sqrt{\mathcal{P}_{meas}(z, \omega)} - \sqrt{\mathcal{P}_{sim}(z, \omega; \alpha)} \right)^2 , \qquad (4.8)$$

where $\mathcal{P}_{meas}(z, \omega)$ is the power spectrum of the measured signal gated with a Hanning window around depth z inside of the ROI and $\mathcal{P}_{sim}(z, \omega; \alpha)$ is the estimated power spectrum at the same depth and for an input attenuation coefficient α.

In order to approximate the experimentally observed signals, the signal power spectrum is estimated for different input values of the attenuation coefficient α. The value corresponding to the highest similarity between the simulated and the measured signals in each analysis window is determined by means of an exhaustive search in the range between 0 and 2 dB/cm/MHz. The total attenuation coefficient of the sample is chosen as the one corresponding to the smallest difference between the spectra along the considered windows:

$$\bar{\alpha} = \arg \min_{\alpha} \left(\sum_{i=2}^{L} D(z_i, \alpha) \right), \qquad (4.9)$$

where z_i is the distance to the ith window and L is the number of windows.

4.3 Experiments

The above described method was validated on both simulated and experimentally acquired radio-frequency (RF) data. At first, the attenuation coefficient of the numerical and real phantoms was estimated using the above described method, and the result was compared to the "ground-truth" value. Next, in order to demonstrate the accuracy of the proposed approach and to analyse the bias introduced by the diffraction effects, the propagation model used in the reconstruction procedure was simplified to the case of plane-wave propagation to mimic the situation where diffraction effects are not being corrected for, as described in App. A, and the reconstruction procedure was repeated. In both cases, the attenuation estimation was performed for different phantom positions in front of the transducer, more specifically in the transducer's near- and far-field and around its focal zone.

4.3.1 RF data simulation

RF signals backscattered from homogeneous phantoms with different attenuation characteristics were generated using the ultrasound simulation software Field II [86]. A single-element focused concave transducer with a center frequency of 5 MHz, a diameter of 12.7 mm and focal depth at 75 mm was modelled using the function "xdc_ concave". A Gaussian-modulated sinusoidal transducer impulse response w_t with a relative bandwidth of 80% was considered together with a 1.5-cycle excitation. A phantom with dimensions of 40 mm × 40 mm × 50 mm consisting of a dense distribution of point scatterers was placed in front of the transducer at three different positions: first, in the near-field of the transducer ("transducer-phantom" distance $d_1 = 1$ mm), next, in its focal zone ($d_2 = 50$ mm) and finally in its far-field ($d_3 = 75$ mm). 20 RF lines of the scattered signals were generated for each phantom position considering different realizations of the positions of the scattering sites. The speed of sound in the background and phantom media was set to 1540 m/s. At each phantom position, a set of RF signals was generated with three different attenuation coefficients: 0.3, 0.5 and 0.7 dB/cm/MHz.

In order to define the function $S_{Tx,Rx}(\omega)$ which is used in Eq. 4.3, a temporal Fourier transform was calculated of the double convolution of the electrical excitation $S_{t,Tx}(t)$ used in the Field II simulation with the temporal impulse response of the selected transducer:

	Speed of sound, m/s	Density, kg/m^3	Attenuation coefficient, dB/cm/MHz	Water distance, z_m, mm	
				position 1	position 2
Ph. A	1551	1080	0.38	53.8	11.7
Ph. B	1550	1129	0.35	57.4	11.7
Ph. C	1542	1087	0.65	46.2	10.5
Ph. D	1546	1000	0.62	46.0	10.5
Ph. E	1545	1051	0.69	44.6	10.4
Ph. F	1554	1088	0.70	56.7	11.7
Ph. G	1552	1099	0.72	57.2	11.7
Ph. H	1581	1265	0.77	59.6	11.8
Ph. I	1568	1322	0.61	60.4	11.8

Table 4.1: *Acoustic properties of the tissue-mimicking phantoms (determined from through-transmission substitution experiments) and the transducer-phantom distance in the experiments.*

$$S_{Tx,Rx}(\omega) = \mathcal{F}\left\{(S_{t,Tx}(t) \otimes \mathrm{w}_t(t)) \otimes \mathrm{w}_t(t)\right\} =$$
$$= \mathcal{F}\left\{S_{t,Tx}(t)\right\}\left(\mathcal{F}\left\{\mathrm{w}_t(t)\right\}\right)^2. \tag{4.10}$$

4.3.2 Experimental data acquisition

The performance of the proposed method was also tested on experimental data using tissue-mimicking phantoms with different attenuation characteristics. 7 gelatin and 2 PVA phantoms were prepared as described in [66, 68] by mixing dry gel powders - 13.5% gelatin (AppliChem, Darmstadt, Germany) or 10% PVA (Sigma-Aldrich Chemie, Steinheim, Germany), - with deionized water. Graphite powder in a concentration of 30-70 g/L (Acros Organics, Geel, Belgium) was used to alter the scattering and attenuation properties. In this way, 9 homogeneous cylindrical phantoms (50 mm in length; 35 mm in diameter) were created and labelled with alphabetic letters from "A" to "I".

The acoustic parameters of the phantoms were first measured using a traditional through-transmission substitution method at room temperature (22 ℃), as described in [64]. Their values are listed in Table 4.1. The determined attenuation coefficients for each phantom showed a linear dependence on fre-
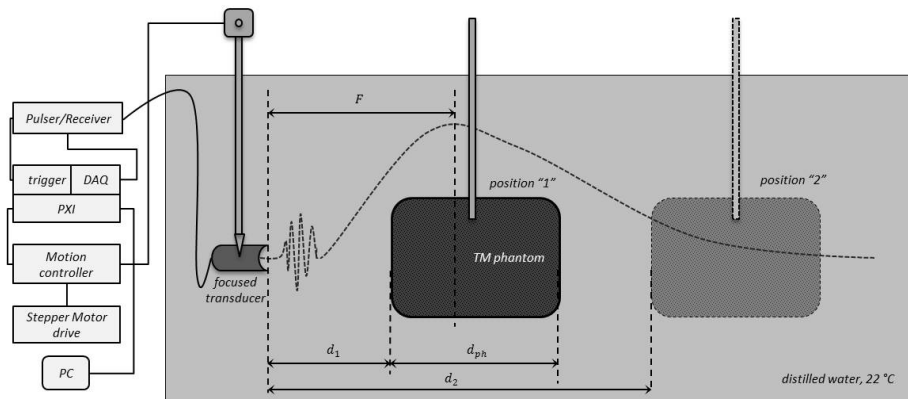
Figure 4.2: *Schematic diagram of the experimental setup for pulse-echo measurements.*

quency. Their values were considered as "ground-truth" and were used for the verification of the attenuation estimates that were later obtained from the backscattered signals. It was also verified that the speed of sound for each phantom was constant with frequency; its value was used as an input for the simulations.

The backscattered signals were recorded in pulse-echo mode using a single transducer operating as emitter as well as receiver. A schematic diagram of the experimental setup used for these measurements is shown in Fig. 4.2. A focused single element transducer was used: V306 (Panametrics NDT, Inc., Waltham, MA) with 0.5" (13 mm) diameter, 2.25 MHz center frequency, 60% bandwidth and a radius of curvature of 0.88" (75 mm). First, a phantom was placed in the water tank approximately around the focal zone of the operating transducer (position "1" at distance d_1 in Fig. 4.2) and then in its far-field (position "2" at distance d_2).

A negative impulse was generated on a Pulser/Receiver (5058PR, Panametrics Canada NDT, Quebec) and sent to the emitting/receiving transducer. At each fixed transducer-phantom distance, 16 received signals were averaged, digitized on a data acquisition card and stored on a PC for further analysis. For each phantom and position, 20 independent RF lines were acquired, slightly moving the transducer in the plane parallel to the surface of the phantom in steps of 1 mm. The movement was realized by a linear motion stage (Velmex Bislides, Velmex Inc., Bloomfield, NY) controlled by a stepper motor drive (NI MID-7604) connected to a motion controller (NI PXI 7334, National Instruments Corporation, Austin, TX). The synchronisation, data acquisition and motion control were automated using the graphical programming software LabView
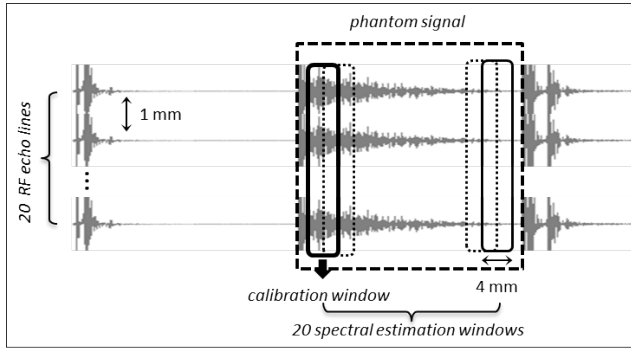
Figure 4.3: *Schematic diagram of the data processing approach for the estimation of the spectrum of the measured data.*

(National Instruments Corporation, Austin, TX).

In the present setup, the source and the scattering volume were separated by a layer of distilled water, which was taken into account when computing the transfer functions in Eq. 4.3. All measurements were performed at 22 °C and the following values for the density, speed of sound and attenuation of distilled water were taken from literature as input for the simulations: $\rho_w = 1000^{kg}/m^3, c_w = 1483^m/s, \alpha_w = 0.0022^{dB}/cm \cdot MHz$.

Finally, the required input spectrum $S_{Tx,Rx}(\omega)$ for the simulations in the reconstruction procedure was determined from the plate reflections measurements as described in App. B.

4.3.3 Data processing

In every simulated and experimental data set, the recorded RF echo lines were gated with a rectangular window to select the proper section of the signal corresponding to the scattering from the phantom. Each gated signal was further portioned into overlapping windows of 4 mm (~13 wavelengths for the speed of sound of 1540 m/s and 5 MHz frequency) with 50% overlap (Fig. 4.3). The ROI in every phantom that was used for the attenuation estimation consisted of 20 RF echo lines with 20 overlapping windows each, and had a size of 19 and 42 mm in lateral and axial directions, respectively (~62 and 136 wavelengths). In each window, the signal was gated using a Hanning window and a Fourier transform of the gated signal was evaluated. The Fourier spectra of the windows corresponding to the same depth from different RF lines in the ROI were averaged to obtain a power spectrum estimate.

Further, the received spectra were estimated at every window position for a

varying attenuation coefficient as input to Eq. 4.3. The attenuation of the phantoms used in this study was modelled assuming a linear dependence on frequency ($n = 1$ in Eq. 3.25). Because the attenuation coefficient of soft tissue as well as of the currently studied tissue-mimicking phantoms is not expected to exceed 2 dB/cm/MHz [71], the input attenuation coefficient in the simulation was discretely changed in the interval between 0 and 2 dB/cm/MHz with a step of 0.05 dB/cm/MHz. The resulting estimated spectra were compared to the simulated or real experimental spectra obtained at the corresponding depth using the above outlined sliding window approach after a calibration in the first window. An example of the spectral comparison for both simulated and experimental data can be seen in Fig. 4.4. A -20 dB frequency range of all spectra was selected for the comparison in order to operate above the noise level. The distance between the spectra of the windowed signals at every depth and for every attenuation input was calculated using Eq. 4.8, and, finally, the global attenuation coefficient of the phantom was determined using Eq. 4.9.

In this way, the attenuation coefficient of each phantom was estimated using data sets recorded at different "transducer-phantom" distances, namely in the near-field, focal zone and far-field for the simulation study and in the focal zone and far-field for the experimental study. As mentioned before, the reconstruction was performed considering two conditions. First, the attenuation estimates were obtained under the assumption of the joint action of diffraction and attenuation, and afterwards under the assumption of plane-wave propagation neglecting the diffraction effects.

Some additional analysis were performed to verify the accuracy and the variance of the local attenuation estimates and to check the feasibility of increasing the spatial resolution of the proposed method by decreasing the number of windows used during the spectral comparison. For this purpose, local attenuation estimates were determined in every window as:

$$\alpha(z_i) = \arg\min_{\alpha} D(z_i, \alpha). \tag{4.11}$$

4.4 Results

The total attenuation estimates obtained in the simulation study are presented in Table 4.2 and visualized in Fig. 4.5a. When the effects of diffraction were incorporated in the model, the method allowed to retrieve the exact attenuation coefficient of the generated signals regardless of the position of the phantom with respect to the transducer focus. As expected, when the effects of diffraction are not accounted for, the attenuation coefficient is underestimated in
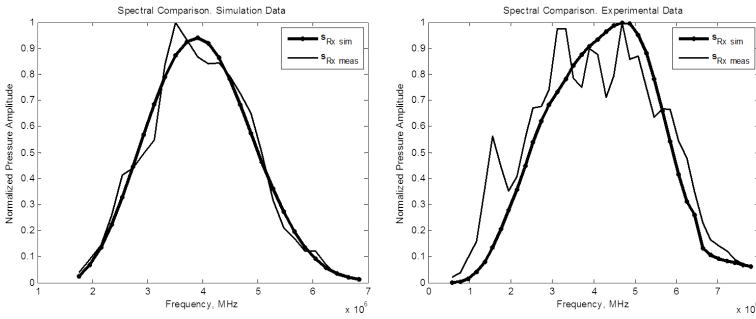
Figure 4.4: *Example of the spectral fit between the measured and simulated Fourier spectra in the simulation study (on the left) and in the experimental phantom study (on the right).*

the near-field of the transducer, where the amplitude of the ultrasound beam experiences increase due to the focusing of the beam, and is overestimated in the far-field region, where its amplitude decreases due to diffraction. Fig. 4.5b presents the average of local estimates obtained for every data set. It can be seen that the average local estimates do not significantly deviate from the total attenuation estimates in Fig. 4.5a. When the diffraction was taken into account, the standard deviation of the local estimates did not exceed 0.05 dB/cm/MHz. In Fig. 4.6a, the local attenuation estimates are shown as a function of depth of the estimation window. It can be seen that the estimates start converging to a certain value after the first 15- 20 mm inside of the ROI. Finally, Fig. 4.6b presents the distance measure of Eq. 4.8 computed in the focal zone of the transducer, which appears to have a clear minimum for all three data sets.

	Estimated attenuation coefficient, dB/cm/MHz (relative error, %)					
	With diffraction correction			Without diffraction correction		
"Ground truth"	Near-field	Focal zone	Far-field	Near-field	Focal zone	Far-field
0.3	0.30 (0)	0.30 (0)	0.30 (0)	0.20 (33)	0.40 (33)	0.45 (50)
0.5	0.50 (0)	0.50 (0)	0.50 (0)	0.35 (30)	0.60 (20)	0.65 (30)
0.7	0.70 (0)	0.70 (0)	0.70 (0)	0.60 (14)	0.85 (21)	0.85 (21)

Table 4.2: *Attenuation estimates obtained in the simulation study, with and without diffraction correction at different positions along the transducer beam.*
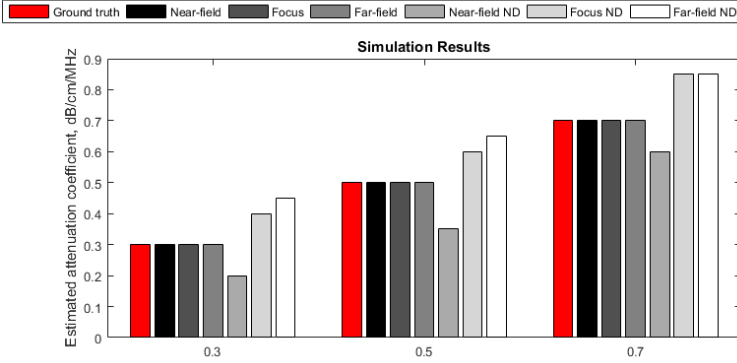
(a)
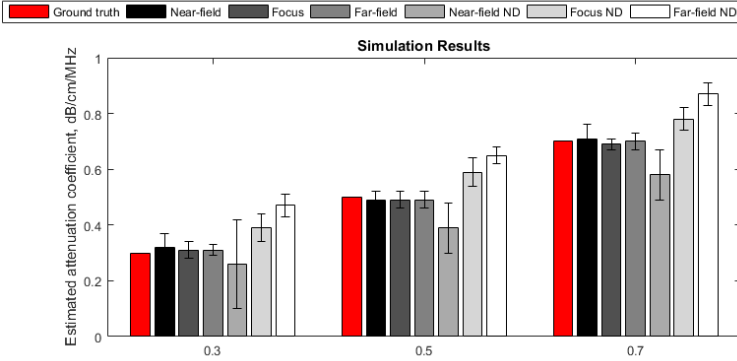
(b)

Figure 4.5: *Total (a) and averaged local (a) attenuation estimation results in the simulation study based on three data sets with attenuation coefficients equal to 0.3, 0.5 and 0.7 dB/cm/MHz. "ND" denotes the estimates obtained without diffraction correction (plane-wave propagation model).*
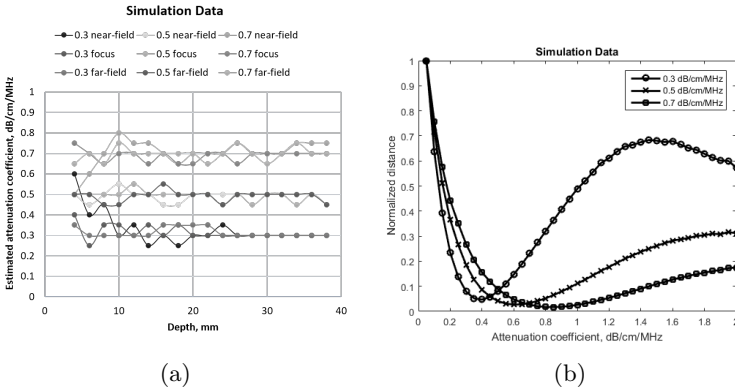
(a)

(b)

Figure 4.6: *(a) Local attenuation estimates obtained at different depths for three data sets with attenuation coefficients equal to 0.3, 0.5 and 0.7 dB/cm/MHz generated in the near-field, focal zone and far-field of the transducer. (b) Distance measure (Eq. 4.8) versus the input attenuation coefficient values of the exhaustive search for the three data sets computed at the focal zone of the transducer.*

The results of the experimental phantom study are presented in Table 4.3 and visualized in Fig. 4.7a. The proposed method provided close to the "ground-truth" attenuation estimates both in the focal zone of the transducer as well as in the far-field with average relative errors of 9.2% and 10.0%, respectively. As expected, upon neglecting diffraction effects, the attenuation estimate in the focal zone were acceptable (average relative error of 7.2%). However, the attenuation estimates in the far-field were considerably overestimated (average relative error of 41.3%). Although the average error of the attenuation estimates obtained in the focal zone with the diffraction correction is slightly higher than the error obtained when the diffraction effects were not accounted for, these results are not statistically different. On the contrary, the average estimates obtained in the far-field of the transducer under the plane wave approximation are statistically different from those obtained with the diffraction correction (p-value < 0.001). Fig. 4.7b presents the averaged local attenuation estimates for the same data sets. Again, it can be seen that these values do not significantly differ from the total attenuation estimates. However, for some data sets high values of the standard deviation can be noticed. In Fig. 4.8, the local attenuation estimates are shown with depth inside the ROI obtained in the focal zone (a) and in the far-field (b) of the transducer. Again, the estimates seem to converge to a particular value at a depth of 15 - 20 mm. However, it can be noticed that the far-field estimates possess a higher vari-

73

ance. Finally, Fig. 4.8c presents the distance measure of Eq. 4.8 computed for all 9 considered phantoms in the zone. The distance shows a clear global minimum for all data sets.

		Estimated attenuation coefficient, dB/cm/MHz (rel. error, %)			
		With diffraction correction		Without diffraction correction	
	"Ground truth"	Focal zone	Far-field	Focal zone	Far-field
Ph. A	0.38	0.35 (7.9)	0.30 (21.0)	0.40 (5.3)	0.55 (44.7)
Ph. B	0.35	0.35 (0.0)	0.30 (14.3)	0.45 (28.6)	0.60 (71.4)
Ph. C	0.65	0.70 (7.7)	0.70 (7.7)	0.65 (0.0)	0.95 (46.2)
Ph. D	0.62	0.65 (4.8)	0.70 (12.9)	0.65 (4.8)	0.90 (45.2)
Ph. E	0.69	0.70 (1.5)	0.70 (1.5)	0.70 (1.5)	1.05 (52.2)
Ph. F	0.70	0.65 (7.2)	0.70 (0.0)	0.70 (0.0)	0.95 (35.7)
Ph. G	0.72	0.65 (9.7)	0.80 (11.0)	0.70 (2.8)	1.10 (52.8)
Ph. H	0.77	0.70 (9.0)	0.80 (3.9)	0.80 (3.9)	0.90 (16.9)
Ph. I	0.61	0.40 (34.4)	0.50 (18.0)	0.50 (18.0)	0.65 (6.6)
average error:		9.2	10.0	7.2	41.3

Table 4.3: *Total attenuation estimates along the propagation path obtained in the experimental phantom study, with and without diffraction correction at different positions along the transducer beam.*

4.5   Discussion and conclusion

In the present study, we improved the previously proposed model-based attenuation estimation algorithm, described in chapter 2, which in its original implementation was limited to a case of plane wave propagation. In the current adaptation of the method, diffraction effects are explicitly accounted for, and the attenuation coefficient is reconstructed by comparing the spectra of the recorded scattered signals from the tissue with theoretically predicted spectra computed using a numerical model of ultrasound wave propagation that properly mimics the experimental setting and the finite transducer characteristics. In this way, acoustical effects such as diffraction which may bias the attenuation estimates do not need to be corrected for as they are intrinsically incorporated into the propagation model. Moreover, in the future, the numerical model
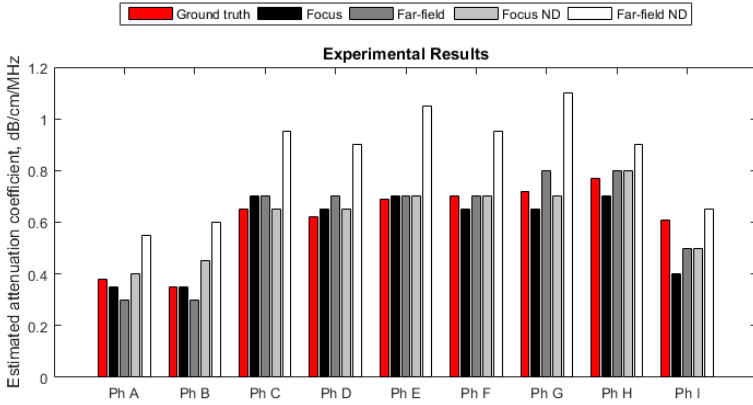
(a)
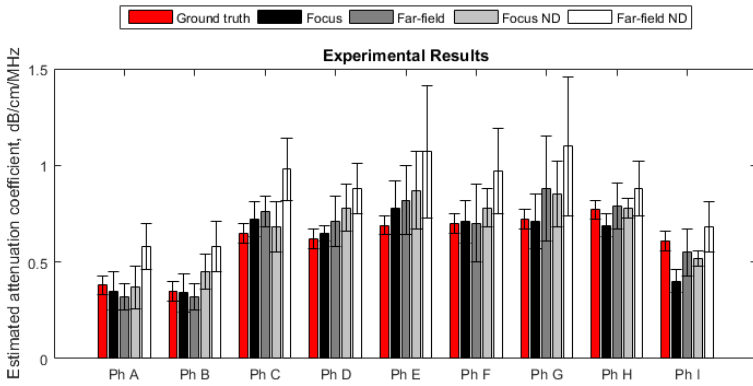
(b)

Figure 4.7: *Total (a) and averaged local (b) attenuation estimation results in the experimental phantom study based on eleven TM phantoms (labeled A to I) with "ground-truth" attenuation coefficient values determined using an insertion-substitution method. "ND" denotes the estimates obtained without diffraction correction (plane-wave propagation model).*

can be gradually improved to provide more realistic attenuation estimates in specific set-ups and conditions, for instance by including nonlinearity.

As a first step, the propagation model was extended to 3-D through the inclusion of diffraction effects. The ultrasonic wave propagation was modelled using the angular spectrum approach due to its ability to easily account for layered media. During the spectrum estimation, a point scattering model was adopted as it is considered to be the most suitable model for describing the scattering effect from graphite particles (which are frequently used in validation and calibration experiments to produce scattering in phantoms). The scattering model can be easily modified to describe other common scatterer types using the form-factors given in [1, 89]. However, it should be noted that only one type of scatterers can be considered at a time, which can be a limiting factor in some applications.

Further, the frequency dependence of the attenuation, which was presently assumed to be linear based on experimental observations, can easily be adjusted in the model. Moreover, the current assumption of linear wave propagation could also potentially be surpassed by adapting the wave equation and including nonlinear effects into the angular spectrum simulation procedure [80]. It is important to note that in the present study, all acoustic parameters required for the model, apart from the attenuation of the sample, were supposed to be known. In clinical practice, where the acoustic properties of the tissue cannot be simply measured using the insert-substitution method, tables with average values for characteristics such as speed of sound and density of soft tissues can be found in the literature [71].

Finally, even though the present study was limited to the consideration of a single-element transducer, any other transducer type can be incorporated into the propagation model by modifying the transducer's weighting function. As such, an extension to a phased array transducer will be the topic of future work. While the proposed method still requires an additional measurement to determine the spectrum of an input pulse, this measurement has to be performed only once, unless the ultrasound probe or its excitation is changed, and, in contrast with reference phantom techniques, does not have to be repeated every time the focal settings are updated.

Two other possible improvements concern the size of the estimation data block and the optimization process. In this study, the entire ROI was used during the attenuation estimation process, whose dimensions were ~ 20 mm $\times 40$ mm. However, as can be seen from Fig. 4.6a and Fig. 4.8a and Fig. 4.8b, the size of the ROI could be possibly decreased by a factor of 2. These figures clearly illustrate the accumulative nature of the attenuation, i.e. the fact the effect becomes more apparent with depth, and the aforementioned offset of 15 - 20 mm is therefore, required for the method to produce realistic results. Increased

variances of the attenuation estimates obtained in the far-field of the transducer in the experimental study compared to those in the focal zone, can be probably explained by the decreasing SNR at larger depths. Concerning the optimization process, the apparent global minima of the cost-functions in both simulation and experimental studies suggest that the exhaustive search procedure could be likely replaced by a more efficient gradient descent method.

Overall, in its current version, the proposed method provided accurate attenuation estimation results on both synthetic and experimental phantom data, largely independent of the diffraction effects. Furthermore, the proposed approach has the potential to be applied in more complex cases by means of a comprehensive improvement of the underlying model. This feature will be investigated and reported on in the future.
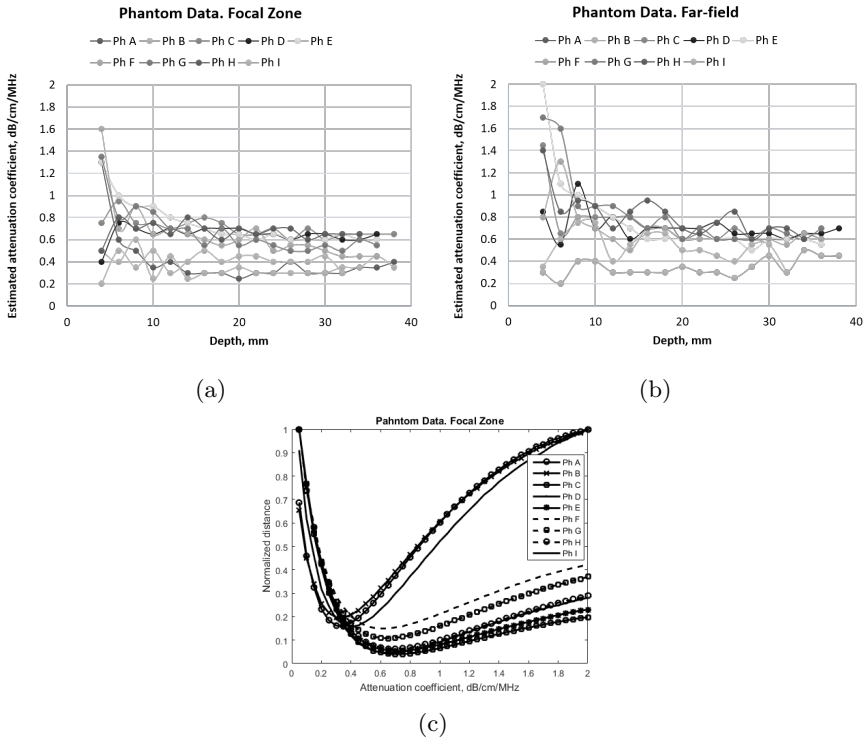
Figure 4.8: *Local attenuation estimates obtained at different depths in the experimental phantom study based on eleven TM phantoms (labeled A to I) in the focal zone (a) and far-field (b) of the transducer. (c) The distance measure (Eq. 4.8) versus the input attenuation coefficient values of the exhaustive search computed in the experimental phantom study at the focal zone of the transducer.*

Chapter 5

Extension of the angular spectrum method to model the pressure field of a cylindrically curved array transducer

Abstract

An extension to the angular spectrum approach for modelling pressure fields of a cylindrically-curved array transducer is described in this chapter. The proposed technique is based on representing the curved transducer surface as a set of planar elements whose contributions are combined at a selected intermediate plane from which the field is further propagated using the conventional angular spectrum approach. The accuracy of the proposed technique is validated through comparison with Field II simulations.

5.1 Introduction

The angular spectrum approach (ASA) has been widely used to model pressure fields generated by ultrasonic transducers [78, 80, 82–84]. This method makes use of a two-dimensional Fourier transform to propagate the pressure field in-between parallel planes and is known to be highly computationally efficient and easy in implementation. For wave propagation in a homogeneous media, the ASA has been shown to be equivalent to other simulation methods such as directly solving the Rayleigh-Sommerfeld integral or ones based on the spatial impulse response method [77, 86, 95]. While the Rayleigh-Sommerfeld integral method is relatively time-consuming, the spatial impulse response method intrinsically assumes linear wave propagation in an acoustically homogeneous medium. In contrast, the ASA can be extended to include nonlinear effects and to model pressure fields in layered (i.e. inhomogeneous) media [78, 80].

In order for the ASA to be applied, knowledge of the field distribution on the source plane is required. Although this problem is straightforward for planar transducer geometries, it is not for curved transducers as used in many medical applications to improve focusing. In this chapter, we propose an extension of the angular spectrum method to a case of a cylindrically curved array transducer as commonly used in medical ultrasound imaging. This technique provides easy means for analysis and interpretation of acoustic fields radiated from such transducers and is inspired by the method that was recently proposed for a spherically curved transducer [83].

The procedure described in Ref. [83] consists of dividing the transducer surface into a set of planar concentric rings, each contained within a plane parallel to a selected intermediate plane in front of the transducer. The angular spectrum of each ring is calculated separately and propagated to this intermediate plane, where the contributions of all rings are added. Subsequently, the intermediate plane is used as the source plane for sound field estimation using the conventional ASA. The purpose of this chapter was therefore to demonstrate the
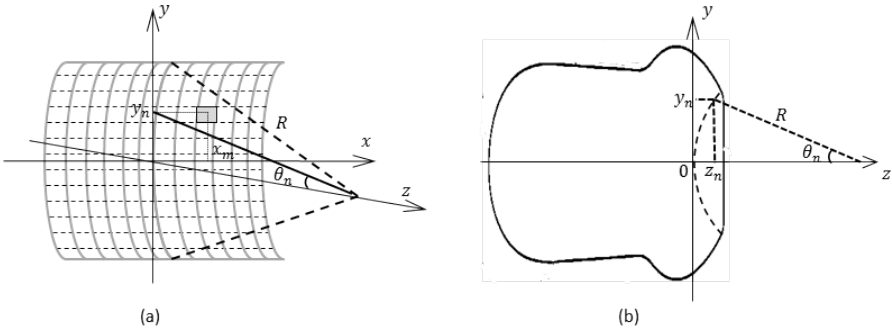
Figure 5.1: *Representation of a cylindrically-curved linear array transducer by a set of planar rectangles: 3-D view (a) and cross-sectional view (b).*

application of a similar strategy as the one proposed by Vyas & Christensen in order to compute the spectrum of a cylindrically curved array transducer. First, the calculation procedure is described, followed by the comparison of the numerical results to those obtained with Field II [86].

5.2   Method

Herein, a cylindrically curved ultrasonic array was considered with N_{el} elements (N_{el} is assumed to be even) of height H and width W, with a zero kerf and a radius of curvature R. The intermediate plane was defined as tangential to the transducer's aperture and perpendicular to the $x - z$ plane (Fig. 5.1 (a)). Next, all transducer elements were subdivided along the elevation direction into $(2N_y + 1)$ small sub-elements that can be regarded as planar rectangles of height $\Delta y = H/(2N_y+1)$. It should be noted that given dense sampling and moderate curvature of the transducer aperture, the sub-elements can be considered parallel to the $x - z$ plane. This assumption greatly simplifies the calculations, since the angular spectrum of each sub-element can be calculated in the same coordinate space.

The angular spectrum of such sub-element centered at (x_m, y_n), where $m = -N_{el}/2, ..., N_{el}/2$ and $n = -N_y, ..., N_y$, is given by:

$$A_{m,n}(k_x, k_y) = \int\limits_{x_m - \frac{W}{2}}^{x_m + \frac{W}{2}} \int\limits_{y_n - \frac{\Delta y}{2}}^{x_m + \frac{\Delta y}{2}} e^{-j(k_x x + k_y y)} dx dy, \qquad (5.1)$$

81

where k_x and k_y are the spatial frequencies.

Substituting $\tilde{x} = {(x-x_m)}/W$ and $\tilde{y} = {(y-y_n)}/{\Delta y}$ we obtain:

$$A_{m,n}(k_x, k_y) = \int\limits_{-\frac{1}{2}}^{\frac{1}{2}} \int\limits_{-\frac{1}{2}}^{\frac{1}{2}} W \Delta y e^{-j(k_x W \tilde{x} + k_y \Delta y \tilde{y})} e^{-j(k_x x_m + k_y y_n)} d\tilde{x} d\tilde{y} =$$

$$= e^{-j(k_x x_m + k_y y_n)} \frac{4 sin\left(k_x \frac{W}{2}\right) sin\left(k_y \frac{\Delta y}{2}\right)}{k_x k_y}.$$

(5.2)

As seen in Fig. 5.1b, the travel distance z_n from each sub-element to the intermediate plane depends on the sub-element's elevational coordinate. Propagation of each sub-element's angular spectrum to the intermediate plane is modelled using the following transfer function [82]:

$$H_{el,n} = \left(e^{-jk_z z_n}\right)^*,$$

(5.3)

where $k_z = \sqrt{k^2 - (k_x^2 + k_y^2)}$ and $k = {\omega}/c$ is the wave number for the angular frequency ω and speed of sound c and '$*$' indicates the complex conjugate. As can be seen from Fig. 5.1b, the travel distance is given by: $z_n = R(1 - cos\theta_n)$. The above transfer function accounts for a phase difference due to the difference in horizontal propagation distance for an element with the elevational coordinate y_n with respect to the central element.

Azimuthal focusing is accounted for by introducing a phase factor determined by the azimuthal coordinate of the sub-element:

$$H_{az,m} = e^{-j\omega t_m},$$

(5.4)

where t_m is the transmit time delay of the mth transducer element, which for a one-dimensional array is given by:

$$t_m = \frac{d_F - \sqrt{(x_m - x_F)^2 + z_F^2}}{c},$$

(5.5)

with d_F the distance from the center of the aperture to the focal point and x_F and z_F - the azimuthal and axial coordinates of the focal point.

Finally, the angular spectrum of the entire transducer aperture on the intermediate plane can be calculated by adding the contributions of all sub-elements (N_{el} in the azimuthal and $2N_y + 1$ in the elevational directions):

$$A(k_x, k_y : \omega) = \sum_{n=1}^{(2N_y+1)} \sum_{m=1}^{N_e l} A_{n,m} H_{el,n} H_{az,m}. \tag{5.6}$$

Substituting Eq. 5.2, 5.3 and 5.4 into Eq. 5.6, we get:

$$A(k_x, k_y : \omega) = \frac{4sin\left(k_x \frac{W}{2}\right) sin\left(k_y \frac{\Delta y}{2}\right)}{k_x k_y} \times$$

$$\times \sum_{n=-N_y}^{N_y} \left[e^{-jk_y y_n} \left(e^{-jk_z z_n} \right)^* \right] \sum_{m=1}^{N_{el}} \left[e^{-jk_x x_m} e^{-j\omega t_m} \right]. \tag{5.7}$$

The first summation on the right-hand side can be rewritten as follows:

$$\sum_{n=-N_y}^{N_y} \left[e^{-jk_y y_n} \left(e^{-jk_z z_n} \right)^* \right] = 1 + \sum_{n=1}^{N_y} \left[2cos(k_y n\Delta y) \left(e^{-jk_z z_n} \right)^* \right]. \tag{5.8}$$

The pressure field distribution in any plane that is parallel to the intermediate plane at distance z can be determined by multiplying the source angular spectrum in Eq. 5.7 with the following transfer function [82]:

$$H(k_x, k_y, z : \omega) = \left(\frac{je^{jzk_z}}{k_z} \right)^*, \tag{5.9}$$

and taking the 2-D inverse Fourier transform of the resulting spatial-frequency distribution.

5.3 Numerical simulation

In order to validate the above expressions, a phased array transducer with a cylindrically curved aperture was modelled using both the above approach and with Field II (based on the spatial impulse response method) [86]. The transducer aperture consisted of 64 (N_{el}) elements of 12 mm × 0.22 mm (corresponding to H and W), and a kerf of zero between the transducer elements was assumed. The radius of the elevation curvature (R) was set to 70 mm and the electronic focus was set at $[x_F, y_F, z_f] = [0, 0, 70 \text{ mm}]$. For the ASA modelling, the number of aperture sub-elements along the elevation direction
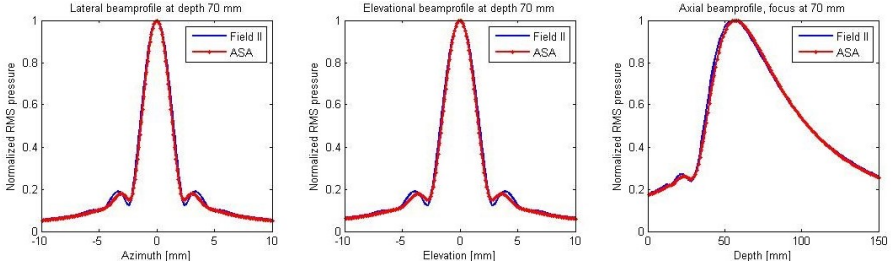
Figure 5.2: *Comparison of the simulated transmit beam profiles of a focused linear array transducer obtained with ASA and Field II: lateral (left), elevational (middle) and axial (right). Transducer element size: 0.22 mm ×4 12 mm, number of elements 64, center frequency 3.5 MHz, elevational focus 70 mm, azimuthal focus 70 mm, measurement depth of transverse plots 70 mm.*

$(2N_y + 1)$ was set to 55 ($\Delta y = \Delta x = \lambda/_2 = 0.22$ mm). In Field II, the function "xdc_focused_array" was used to model the transducer, and the transducer aperture was subdivided into 55 sub-elements in elevational and 1 in azimuthal direction (corresponding to the same sub-element size as used fo the ASA: 0.22 mm × 0.22 mm).

The pressure field propagation was modelled in a homogeneous medium with a speed of sound of 1540 m/s. A Gaussian-modulated sinusoidal pulse of 1.5 periods, 3.5 MHz center frequency and 80% relative bandwidth was generated in Field II and was used as the input for the angular spectrum simulations. For both simulators, a sampling frequency of 100 MHz was used. For the ASA simulations, a 1024-point fast Fourier transform was applied to a time-domain pulse; the pressure field was simulated for non-zero positive frequency components (70 in this case) of the spectrum. Propagation of the pressure field using the ASA was modelled in the spatial-frequency domain and a spatial frequency truncation was applied to avoid aliasing effects as described in chapter 3.

5.4 Results

Figure 5.2 compares the azimuthal and elevational transmit beam profiles at the focal depth and the axial RMS pressure profiles obtained with both simulators showing very good agreement between both simulation approaches. The comparison of the (normalized) transmit RMS pressure fields is presented in Fig. 5.4. Overall, the simulated pressure fields look very similar with a maximal percentage difference of normalized patterns below 6 %. Figure 5.4 compares the normalized transmit pressure fields in the case when the beam was steered

Figure 5.3: *Comparison of the simulated transmit pressure fields of a focused linear array transducer obtained with ASA and Field II: in the azimuthal plane (upper row) and elevational plane (lower row). Transducer element size: 0.22 mm × 12 mm, number of elements 64, center frequency 3.5 MHz, elevational focus 70 mm, azimuthal focus 70 mm, measurement range 1-150 mm.*

in the azimuthal plane (the steering angle was set to 20˚). The percentage difference of the normalized elevational patterns in this case remained below 6%. The difference of the azimuthal patterns slightly increase, but remained below 10%. This increased difference of the azimuthal patterns is probably associated with the difficulties in selecting the optimal size of the spatial grid for ASA in the case of a steered beam, which gradually moves away from the its origin with depth.

All simulations were performed on a computer with an Intel Core i7 2.7 GHz processor and 8 GB physical memory. The estimates of the computation time for both simulation methods are summarized in the Table 5.1.

5.5 Conclusion

The recently proposed method for modelling spherically curved transducer apertures with ASA was reformulated for the case of cylindrically curved arrays. The method divides the transducer aperture into a set of planar rectangular sub-elements, the angular spectrum of which is calculated separately and propagated to a preselected intermediate plane in which the contributions of all sub-

	Field II (broadband)	ASA	
		broadband, i.e. 70 frequency points	center frequency only
Lateral beam profiles	0.95 s	11.7 s	0.22 s
Axial beam profile	0.09 s	1948 s	25.6 s
Field distribution in a plane parallel to the transducer (70 mm)	545 s	59 s	2.0 s

Table 5.1: *Computation time required for the simulations in Field II and ASA.*

elements are combined. The accuracy of the derived expressions was validated through comparison with Field II simulations. As expected, Field II showed faster performance during the computation of pulsed acoustic excitation, while the ASA was more efficient during field computations in a plane parallel to the transducer surface. It should be noted, that these time estimates are purely indicative since the implementation of the proposed ASA approach was done in a MATLAB environment (The MathWorks Inc., Natick, MA, USA) while Field II executes its core calculations in C. Obviously, the proposed method can thus be further optimized using compiled computer languages and effective parallel programming using a multi-core computer or a graphical processing unit. Overall, this study demonstrates that the proposed technique provides an easy means for modelling pressure fields of commonly used transducers for clinical practice that can be extended to consider inhomogeneous media and embedded nonlinear effects.
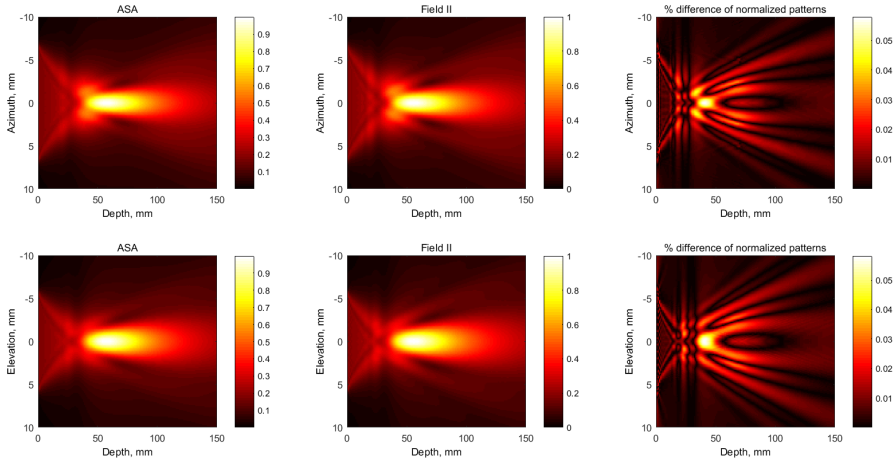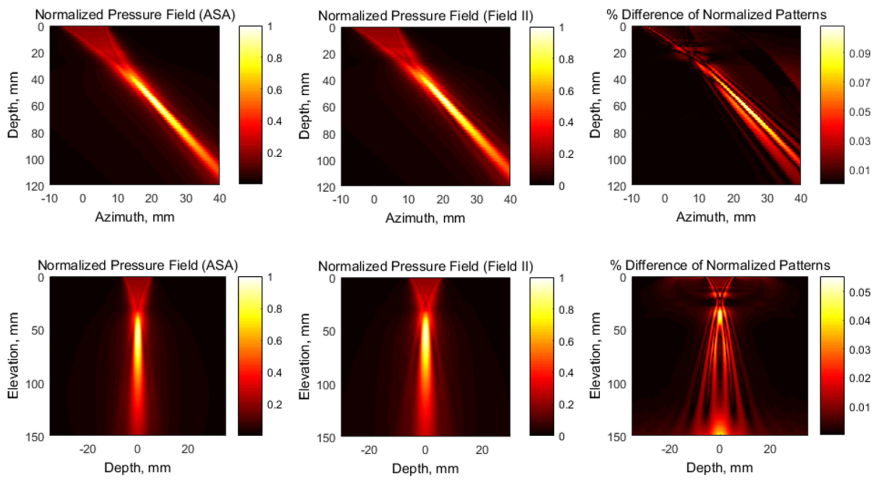
Figure 5.4: *Comparison of the simulated transmit pressure fields of a focused linear array transducer obtained with ASA and Field II for the case of a steered beam (steering angle equal to 20°. The upper row presents the pressure field in azimuthal plane, the lower row - in elevation plane.*

Chapter 6

Diffraction-independent ultrasound attenuation estimation. Part II

Abstract

Quantification of the ultrasound attenuation coefficient has shown potential to provide information on the pathological state of the tissue. However, the main difficulty in the estimation of the attenuation coefficient consists in the need for diffraction correction, that is currently done by means of a reference measurement. Previously, we proposed an alternative attenuation reconstruction technique wherein the attenuation coefficient was estimated by iteratively solving the forward wave propagation problem and matching the simulated signals to measured ones. The simulation procedure involved modelling of the diffraction effects and allowed to avoid several assumptions made by conventional methods. The proposed method showed promising results when applied to data recorded using a single-element transducer. In the present study, this methodology was extended to a clinically more relevant scenario using a phased array transducer. The proposed approach was validated on simulated data in Field II and data recorded in a tissue mimicking phantom with varying focal position. For the simulated data, the relative error of the attenuation estimates did not exceed 7%, while the relative error for the phantom data remained below 10 %.

6.1   Introduction

The potential of measuring the ultrasound attenuation coefficient for tissue characterization has been extensively discussed in literature. Various applications have been considered, including diagnosis of the liver [6–14], kidney [16,17], breast [18,20,21] and myocardium [27–30]. A number of approaches for estimating the attenuation coefficient from backscatter data has been proposed during the last three decades. Typically, these techniques assume that the tissue along the propagation path is homogeneous. However, human anatomy and therefore, the ultrasound beam path inside the body, are inherently heterogeneous. Other common assumptions include a linear frequency dependence of attenuation and a Gaussian pulse spectrum. To consider more general cases, we have previously proposed an alternative, model-based approach for attenuation reconstruction. In this technique, the attenuation coefficient is estimated by iteratively solving the forward wave propagation problem and matching the simulated signals to the measured ones. The simulation procedure includes modelling of the diffraction effects as well as propagation in layered media and allows to avoid several assumptions made by conventional methods. For instance, different frequency dependencies of both attenuation and scattering can be incorporated into the model and a transmit pulse of an arbitrary shape can be considered. Moreover, no reference medium is required to reduce the

system-dependent effects, such as diffraction.

The proposed method showed promising results when applied to data recorded using a single-element transducer. This chapter presents an extension of the proposed methodology to a case of an array transducer as clinically used. The performance of the method is evaluated using data generated in Field II [86] and experimentally acquired phantom and in-vivo liver data. The chapter is organised as follows: section 6.2 briefly describes the previously proposed methodology and its current extension. Section 6.3 presents the simulation and experimental results that illustrate the performance of the proposed new method. Finally, Section 6.4 summarizes the contributions of this chapter.

6.2 Methods and Materials

6.2.1 Theoretical model

As demonstrated in chapter 3, the backscatter power spectrum for a weakly stationary, isotropic medium with a random distribution of scatterers can be expressed as:

$$\mathcal{P}(\omega) = \gamma_0^2 \bar{n} V_s \rho^2 c^2 |S_{Tx,Rx}(\omega)|^2 \omega^6 F(\omega) \int\limits_V h_{Tx}^2(\boldsymbol{r_0}:\omega) h_{Rx}^2(\boldsymbol{r_0}:\omega) d\boldsymbol{r_0}. \quad (6.1)$$

where γ^2 is the mean-square inhomogeneity coefficient, $\bar{n}$ is the average number of scatterers per unit volume, V_s - is the effective scatterer volume, $k = \omega/c$ is the wavenumber and ρ and c are the density and speed of sound, respectively, and the form-factor $F(\omega)$ describes the frequency-dependence of the scattering process depending on the scatterer size, geometry and elastic properties. $S_{Tx,Rx}(\omega)$ is defined by Eq. 3.57 and h_{Tx} and h_{Rx} are the transmit and receive impulse response functions defined in Eq. 3.19 and Eq. 3.54, and the first integral is taken over the scattering volume V. c_γ and ϵ are the correlation coefficient and the correction factor of the scattering process, respectively. The product of the constants in Eq. 6.1 can be replaced by the factor $C = \gamma_0^2 \bar{n} V_s^2 \rho^2/c^4$.

In previous chapters, we used the expression describing scattering from point targets (Eq. 3.64). Such model seems reasonable when considering the scattering effect in phantoms containing distributions of graphite particles, as described in chapter 4. However, soft tissues consist of scatterers of finite size. When characterizing scattering in soft tissues, a Gaussian scattering model is often used, which assumes scattering to arise from continuously varying fluctuations in acoustic properties of the medium, whose spatial autocorrelation function follows a Gaussian form [1, 89, 96, 97]. The Gaussian scatterer is spherical

and has a uniform particle radius that is related to the impedance distribution of the scatterer [98]. This model has been widely used to describe scattering from variuos tissue types as it provides a better approximation of tissue sttructure than a simple linear model (i.e. Rayleigh) [36–38, 96, 98]. The form-factor for the Gaussian scatterer model is given by:

$$F_{Gauss}(\omega) = \frac{\sigma_{Gauss}}{\sigma_{Rayl}} = \frac{\mathcal{P}_{Gauss}(\omega)}{\mathcal{P}_{Rayl}(\omega)} \simeq e^{-0.827k^2 a_{eff}^2}, \qquad (6.2)$$

where a_{eff} is the effective scatterer radius.

Further, as described in chapter 4, propagation of the ultrasound wave described by the impulse response functions h_{Tx} and h_{Rx} can be modelled in the spatial-frequency domain using the angular spectrum approach. Assuming that the dimensions of the scattering medium are significantly larger than the transducer aperture (i.e. no reflections coming from edges of the scattering medium) and examining scattering contributions from thin sub-volumes parallel to the transducer surface (Fig. 4.1), we can compute the backscatter power spectrum corresponding to a gated region around depth z as:

$$\mathcal{P}(\omega, z) = C|S_{Tx,Rx}(\omega)|^2 \omega^6 F(k) \int_S \left[\mathcal{F}_{2D}^{-1} \{H_{Tx}(k_x, k_y, z : \omega)\} \right]^2 \times$$
$$\times \left[\mathcal{F}_{2D}^{-1} \{H_{Rx}(k_x, k_y, z : \omega)\} \right]^2 dx dy, \qquad (6.3)$$

where the integration is performed over a plane parallel to the transducer at depth z in the middle of a thin tissue layer and $\mathcal{F}_{2D}^{-1}\{H\}$ denotes the inverse spatial 2-D Fourier transform of H. The transfer functions H_{Tx} and H_{Rx} describe the forward and backward propagation of an ultrasound wave over a distance between the transducer and the considered tissue layer. For a homogeneous medium, the transmit and receive transfer functions are given by 4.4:

$$H_{Tx/Rx}(k_x, k_y, z : \omega) = A_{Tx/Rx}(k_x, k_y : \omega) H_{Diffr}^{v_n \to \varphi}(k_x, k_y, z : \omega) \times$$
$$\times H_{Att}^{p \to p}(k_x, k_y, z : \omega), \qquad (6.4)$$

where H_{Diffr} and H_{Att} describe the effects of diffraction and attenuation and are given by Eq. 3.24 and Eq. 3.25, respectively, while $A_{Tx/Rx}$ is the transducer's spatial function that is determined by the transducer type, geometry and focal settings. In this chapter, we are considering an elevation focused

array transducer, whose spatial transfer function can be calculated using the expression derived in chapter 5 (Eq. 5.7).

When considering multilayered media, the effects of diffraction and attenuation are computed separately in every layer and the transmission coefficient $T_{i|i+1}^{p \to p}$ at the interface between subsequent layers "i" and "i+1" is introduced as described in chapter 4 (Eq. 4.5).

Eq. 6.3 allows to compute the power spectrum of a signal scattered from a region around a certain depth assuming the input acoustic parameters required for the simulations such as density, speed of sound and thickness of each layer to be known. The attenuation coefficient in the model can be varied within acceptable bounds to match the experimentally observed signals as will be described below. If the electrical excitation of the transducer as well as its transmit and receive transfer functions are known, the temporal function $S_{Tx,Rx}$ can be simply calculated as their product. In the other case, $S_{Tx,Rx}$ can be determined experimentally through a reflector measurement as described in App. B.

6.2.2 Attenuation estimation algorithm

The comparison of the simulated and experimentally observed backscattered signals was performed using a sliding window approach, as described in chapter 4. The first window was used to equalize the energies of the simulated and measured spectra, i.e. eliminate the unknown amplitude coefficient C in Eq. 6.3. After this calibration, the similarity between the simulated and measured power spectra in all windows along the ROI was assessed using the least squares difference. The value corresponding to the highest similarity between the simulated and the measured signals in each analysis window was determined by means of an exhaustive search in the range between 0 and 2 dB/cm/MHz. The global attenuation coefficient of the sample was estimated as:

$$\bar{\alpha} = \arg\min_{\alpha} \left[\sum_{i=2}^{L} \left[\sum_{\omega} \left(\sqrt{\mathcal{P}_{meas}(\omega, z_i)} - \sqrt{\mathcal{P}_{sim}(\omega, z_i; \alpha)} \right)^2 \right] \right], \qquad (6.5)$$

where $\mathcal{P}_{meas}(\omega, z)$ is the power spectrum of the measured signal gated around depth z inside of the ROI and $\mathcal{P}_{sim}(\omega, z; \alpha)$ is the simulated power spectrum at the same depth for an input attenuation coefficient α, z_i is the distance to the ith window and L is the number of the considered windows.

The above described method was validated on both simulated and experimentally acquired radio-frequency (RF) data. In the simulation and experimental phantom study, the obtained attenuation estimates were compared to the

Type	1-D phased array
Number of elements	64
Elements width	0.22 mm
Elements height	12 mm
Kerf	0 mm
Elevation focus	70 mm
Center frequency	3.5 MHz

Table 6.1: *Characteristics of the array transducer used in simulations and experimental studies.*

"ground-truth" values. The performance of the proposed method was analysed using data recorded using different focal settings. Afterwards, attenuation estimates were obtained for in-vivo liver data of healthy volunteers.

6.2.3 Synthetic RF data generation

Synthetic RF signals backscattered from homogeneous media with different attenuation characteristics were generated using the ultrasound simulation software Field II [86]. An array transducer with characteristics as indicated in Table 6.1 was modelled using the function "xdc_focused_array". A Gaussian-modulated sinusoidal transducer impulse response w_t with a relative bandwidth of 80% was considered together with a 1.5-cycle excitation. A phantom with dimensions of 40 mm × 40 mm × 90 mm consisting of a dense distribution of point scatterers was assumed to be in direct contact with the transducer. 50 RF lines of the scattered signals were generated considering different realizations of the positions of the scattering sites, assuming acquisition at a zero degree angle. The speed of sound in the background and phantom media was set to 1540 m/s. The transmit focus was set at 30, 50 and 70 mm from the transducer along the propagation axis. For each focal position, a set of RF signals was generated with three different attenuation coefficients: 0.3, 0.5 and 0.7 dB/cm/MHz. The required input spectrum $S_{Tx,Rx}(\omega)$ for the simulation was computed according to Eq. 4.10.

6.2.4 Experimental RF data acquisition

The performance of the proposed method was further tested on experimental data acquired from a homogeneous region of a CIRS phantom (model 055, Computerized Imaging Reference Systems Inc., Norfolk, VA) and from a homogeneous home-made phantom that was built by mixing gelatin solution (13.5 %, AppliChem, Darmstadt, Germany) with graphite powder (in a concentration of

50 g/L, Acros Organics, Geel, Belgium), as described in subsection 4.3.2. The speed of sound and the attenuation coefficient of the CIRS phantom at 22˚C, as provided by the manufacturer, were 1540 m/s and 0.5 dB/cm/MHz, respectively. The phantom has a cubic shape with the dimensions of 144 mm × 138 mm × 150 mm. The acoustic properties of the home-made phantom were measured using an insert-substitution technique, as described in subsection 2.2.4. The measured speed of sound and attenuation coefficient of the phantom were 1540 m/s and 0.55 dB/cm/MHz, respectively. The phantom had a cylindrical shape with both the height and the diameter equal to 60 mm.

Pulse-echo acquisitions were performed on a high channel density programmable ultrasound platform, HD-PULSE [99]. A phased array probe was used as transmitter and receiver, whose characteristics are summarized in Table 6.1. The transducer was excited with a 1-cycle bipolar pulse with 80% relative bandwidth. The signals recorded at the transducer (i.e. RF channel data) were digitized on data acquisition card (NI 5752, 12 bit, 2 V peak to peak dynamic range, National Instruments Corporation, Austin, TX) at 50 MHz. The transmit focus was successively set at 30 and 50 mm when scanning the home-made phantom and at 30, 50 and 70 mm during the scan of the CIRS phantom. For every phantom and focal position, 50 independent RF signals were acquired under a zero degree beam angle, slightly moving the transducer above the surface of the phantom. During each acquisition, the transducer was kept in direct contact with the phantom. The speed of sound for the beamformer was set at 1540 m/s, and the receive focal settings were identical to those during the transmit event.

Further, data were acquired from normal human livers of 8 healthy volunteers. The experimental protocol for this study was approved by the Medical Ethics Committee of UZ Leuven (dossier S59755). All measurements were made in a supine subject position; the right liver lobe was scanned with the transducer plane along the intercostal spaces. For each subject, the sonographer first positioned the probe using B-mode imaging and then 50 RF frames were successively acquired, keeping the transducer fixed. Due to subject's breathing, statistically independent signals were recorded in each data set. The transmit focus and the range were set to 60 mm and 150 mm, respectively.

Finally, the required input spectrum $S_{Tx,Rx}(\omega)$ for the simulations in the reconstruction procedure was determined from the plate reflections measurements as described in App. B.

6.2.5   RF data processing

The procedure for processing of the acquired RF signals was similar to that described in section 4.3.3 except for some numerical differences. First, in every

simulated and experimental data set, the recorded RF echo lines were gated with a 42 mm long rectangular window. The gated region was selected approximately in the middle of the recorded signals. Each gated signal was further partitioned into overlapping windows of 4 mm with 50% overlap (Fig. 4.3). In this way, the ROI for the attenuation estimation consisted of 50 RF echo lines with 21 overlapping windows ($L = 21$ in Eq 6.5). In each window, the signal was gated using a Hanning window and a Fourier transform of the gated signal $S_{meas}(k, z_i)$ was evaluated. The backscatter power in every window was then calculated by averaging the squared magnitude of the computed for this window Fourier spectra from different RF lines in the ROI:

$$\mathcal{P}_{meas}(\omega, z_i) = \frac{1}{N} \sum_{n=1}^{N} |S_{meas_n}(k, z_i)|^2, \tag{6.6}$$

where N is a number of the recorded RF signals from the sample and z_i is the depth of the considered window.

Further, the backscattered power spectrum was estimated at every window position for a varying input attenuation coefficient using Eq. 6.3 and assuming a linear frequency dependence of the attenuation. Because the attenuation coefficient of soft tissue as well as of the currently studied tissue-mimicking phantoms is not expected to exceed 2 dB/cm/MHz [71], the input attenuation coefficient in the simulation was discretely changed in the interval between 0 and 2 dB/cm/MHz with a step of 0.05 dB/cm/MHz. For synthetic and experimental data, the Rayleigh scatterer model was assumed, while for in-vivo tissue data a Gaussian model was used. The value of the effective scatterer radius a_{eff} for the model was taken from a reference study [92] and was set equal to 120 μm. Further, the presence of intervening tissue layers, such as skin, fat and muscle, as well as of the conductor ultrasound gel, was accounted for in the model. The effects of diffraction and attenuation were modelled separately in every layer using corresponding transfer functions (Eq. 3.24, 3.25) and the transmission coefficient at the interfaces between subsequent layers was computed (Eq. 4.5). The acoustic parameters of the layers were taken from literature and are summarized in table 6.2 [92, 100]. The simulated power spectra were compared to those estimated from the generated and experimentally acquired data using the above outlined sliding window approach, wherein the first window was used for calibration. A -20 dB frequency range of all spectra was selected for the comparison in order to operate above the noise level. The least-squares distance between the power spectra of the windowed signals was calculated at every depth and for every attenuation input, and the global attenuation coefficient of the sample was determined using Eq. 6.5.

Layer	Layer thickness, mm	Density, kg/m^3	Sound speed, m/s	Attenuation coefficient, dB/cm/MHz
gel	1.0	993	1524	0.005
skin	2.0	1120	1613	1.57
fat	4.0	950	1478	0.48
muscle	11.0	1050	1547	1.09
liver	-	1060	1540	-

Table 6.2: *Characteristics the gel and tissue layers used in simulations. Acoustic properties of tissue layers at 37°C were taken from [100], while the average tissue layers thicknesses were taken equal to those reported in [92] for healthy subjects. The acoustic properties of conductor gel were taken equal to those of water reported in [100] at 37°C. The speed of sound in liver was set equal to that of the beamformer.*

6.3   Results

The results of the simulation study are summarized in Fig. 6.1. The attenuation estimates are presented for the three data sets with the "ground-truth" attenuation coefficient of 0.3, 0.5 and 0.7 dB/cm/MHz. The attenuation estimates were obtained from the data recorded with different focal settings. In all cases, the proposed method was able to reconstruct the exact attenuation coefficient of the data set. Fig. 6.1 compares the total attenuation estimates with the averaged local ones(obtained using Eq. 4.11). Very good agreement between the estimates and moderate variances of the local estimates can be observed. Fig. 6.3 presents the results of the attenuation estimates obtained in tissue-mimicking phantoms. Exact estimates were obtained for the CIRS phantom when the focus was set at 30 and 50 mm. The relative error of the attenuation estimate obtained when the focus was set at 70 mm was 10%. The estimates obtained for the home-made phantom were in a good agreement with the value of 0.55 dB/cm/MHz measured with the insert-substitution technique. The relative error of both estimates (corresponding to the focal depth of 30 and 50 mm) was 9%. The averaged local attenuation estimates appeared less accurate with an average error of 20%. Finally, Fig. 6.3 summarizes the results of the attenuation estimation on in-vivo liver data obtained in healthy volunteers. Under the assumption of a homogeneous medium, the measured attenuation coefficient was in the range of 0.40 - 0.75 dB/cm/MHz with a mean value of 0.57 ± 0.13 dB/cm/MHz. When intervening tissue layers were considered in the propagation model, the measured attenuation coefficient was in the range of 0.35 - 0.70 dB/cm/MHz with a mean value of 0.48 ± 0.13 dB/cm/MHz. These results are statistically different (p-value≈0.005). The averaged local
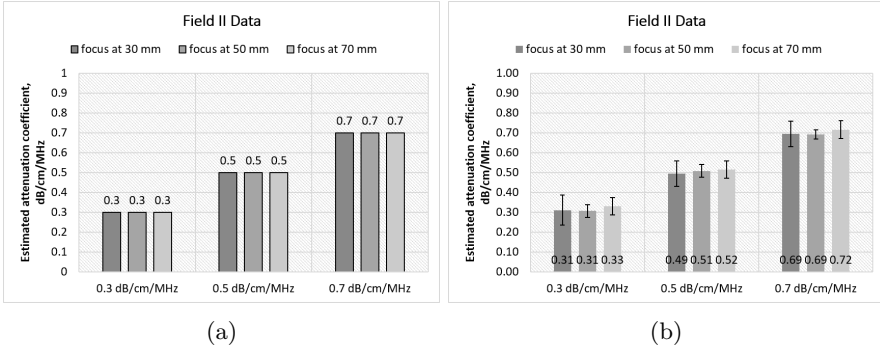
Figure 6.1: *Total (a) and averaged local (a) attenuation estimates obtained in the simulation study based on three data sets with attenuation coefficients equal acquired when the transmit focus was set at 30, 50 and 70 mm.*

estimates are in a good agreement with the total estimates, however possess a large variance.

6.4   Discussion

This chapter presents an extension of the previously proposed method for attenuation reconstruction towards a clinical application. The proposed approach is model-based, and therefore, can be modified or improved at all levels to better suit a particular application. In chapter 4, the proposed method was validated using a single-element transducer under the assumption of point scatterers (Rayleigh model). In this study, two major improvements have been demonstrated: 1) the extension of the proposed approach to a case of an array transducer and 2) the introduction of a more descriptive scattering model (i.e. Gaussian). While quantitative ultrasound techniques typically use a reference measurement to minimize the diffraction effects, the proposed approach accounts for the diffraction effects in the propagation model and requires a single transducer calibration that does need to be repeated when the system's settings are changed.

The improved algorithm was first tested on synthetic phantoms generated in Field II for different input attenuation coefficients, followed by the experimental study on two tissue mimicking phantoms. The attenuation estimates for both synthetic and real phantoms were in a good agreement with the "ground-truth" and were not influenced by varying focal settings. Next, the proposed method was used to estimate the attenuation coefficient in human liver in-vivo. For comparison, an overview of previously reported attenuation estimates in
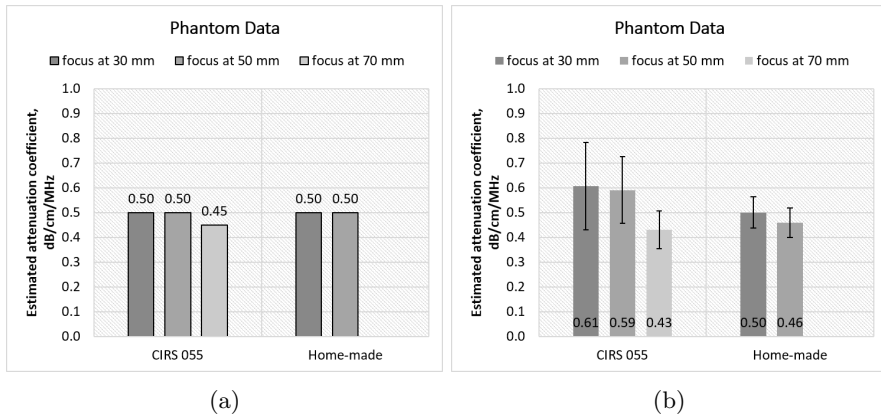
Figure 6.2: *Total (a) and averaged local (a) attenuation estimates in the experimental phantom study based on CIRS 055 and a home-made TM phantoms with "ground-truth" attenuation coefficients of 0.5 and 0.55 dB/cm/MHz, respectively, obtained at different focal settings.*

human liver is presented in Table 6.3. It should be noted that this review is demonstrative but not exhaustive. The variation among the presented estimates may be attributed to the differences in the experimental set-up used (e.g. ultrasound scanning system, transducer, scanning direction and ROI selection) [14]. The obtained results in the present study were in a good agreement with the previously reported values. Overall, the estimates obtained in multi-layer simulations are lower than those computed under an assumptions of a homogeneous medium. These result suggest that the assumption of a homogeneous tissue results in overestimation of attenuation coefficient values in-vivo.

Considering the strong correlation of the attenuation coefficient with several pathologies, such as liver steatosis and cirrhosis, future studies will investigate the potential of the proposed algorithm for liver diagnosis. Furthermore, future studies will be directed towards the simultaneous estimation of the attenuation coefficient and scatterer properties, such as acoustic concentration and scatterer radius. Of particular interest would be an extension of the proposed approach to the case of nonlinear wave propagation and nonlinear frequency dependence of the attenuation.

Reference	Estimated range, dB/cm/MHz
Kuc [101]	0.40-0.48
Maklad [8]	0.48-0.55
Garra [102]	0.20-0.85
Wilson [9]	0.38-0.63
Parker [57]	0.37-0.63
Oosterveld [65]	0.42-0.62
Zagzebski [93]	0.44-0.59
Lu [13]	0.48-0.62
Oosterveld [65]	0.42-0.62
Fujii [5]	0.49-0.69
Sasso [14]	0.47-0.70

Table 6.3: *Estimates of the attenuation coefficient in liver reported in previous in-vivo studies.*

6.5 Conclusion

Estimation of the attenuation coefficient is of a great interest in ultrasound tissue characterization. Moreover, accurate measurement of the attenuation from backscattered signals would be beneficial for a proper time-gain compensation. However, accurate attenuation estimation in-vivo remains challenging due to the need for the diffraction compensation and the complexity of the analysis of a heterogeneous human anatomy. The proposed model-based approach can potentially overcome these limitations by means of computer simulations. As such, the current simulation procedure includes modelling of the diffraction effects as well as propagation in layered media. In this study, the proposed approach was validated on both simulation and experimental data acquired with an array transducer. The error of the attenuation estimates obtained for both synthetic and real tissue-mimicking phantoms did not exceed 10%, while the estimates obtained in human liver in-vivo were in a good agreement with the values presented in the literature.
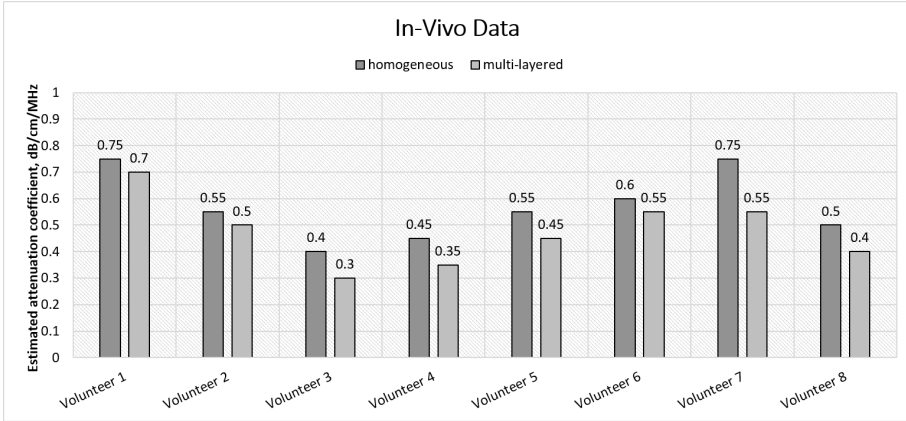
(a)
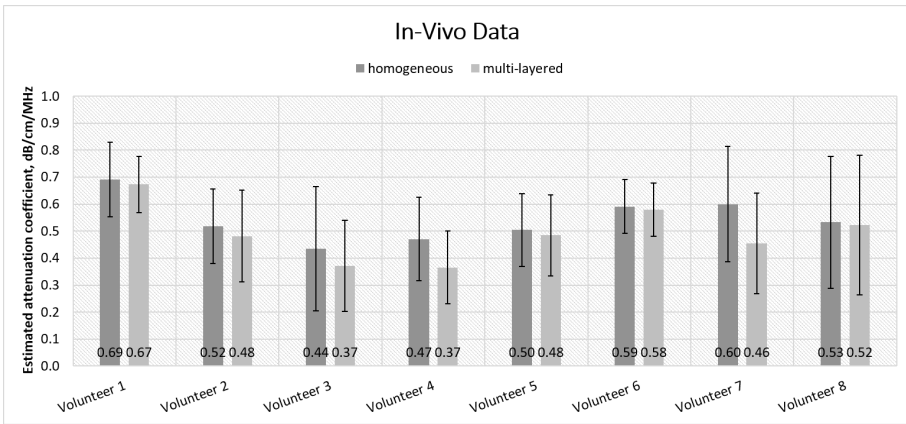
(b)

Figure 6.3: *Total (a) and averaged local (a) attenuation estimates obtained in liver of 8 healthy volunteers by means of homogeneous and multi-layered simulations*

Chapter 7

General conclusions and future perspectives

7.1   Main contributions

Ultrasound imaging is an indispensable tool in medical diagnostics and offers several advantages over other imaging techniques. During the last decades, ultrasound technology achieved significant progress leading to improved image quality. However, conventional ultrasound envelope-detected images remain qualitative in nature and lack quantitative information on the tissue state and pathology. Therefore, there has been an increased interest in developing techniques that would enhance the diagnostic capabilities of ultrasound imaging. Typically, quantitative ultrasound techniques investigate the spectral properties of the unprocessed scattered signals recorded by an ultrasound system and attempt to relate these to tissue structural properties. The main challenge in the analysis of scattered signals is the complexity of ultrasound-tissue interactions and their interpretation. Moreover, the scattered signals detected by the system scattered signals are not entirely defined by tissue properties, but are also influenced by system-dependent factors (such as focusing), that have to be properly corrected for prior to analysis. Current state-of-the-art methods for ultrasound tissue characterization focus on one particular type of ultrasound interaction with tissue and try to estimate the associated parameters directly from the backscattered signals. The correction for system dependencies is done by means of a reference measurement assuming constant propagation speed of ultrasound in tissue. These simplifying assumptions limit the applicability of the existing techniques in practice. Therefore, there is a great necessity to develop tools that would allow the controlled analysis of the

combined effect of various ultrasound-tissue interactions, as well as system-dependent effects.

Better understanding of the underlying physical mechanisms can be achieved by modelling ultrasound propagation in tissue, wherein various interactions as well as their combined effect can be studied in a controlled manner. With the help of such a model we can attempt to solve the so-called "inverse scattering problem", where the acoustic parameters are estimated by comparing experimentally measured backscattered signals with the theoretically modelled ones. Therefore, in the context of this thesis, an alternative, model-based methodology for ultrasound tissue characterization was developed. Application of the proposed methodology for the reconstruction of tissue attenuation was presented and thoroughly investigated.

The main contributions of this work can be summarized as follows:

- **Investigation of the feasibility of the proposed approach** through its experimental validation and comparison with the conventional methods. This preliminary study showed the potential of the proposed approach to provide accurate attenuation estimates in a simplified case of plane wave propagation. When compared to existing methods, the developed approach appeared to be less sensitive to measurement noise and weak scattering variations throughout the medium and substantially outperformed the reference methods in the experimental study.

- **Development of an ultrasound simulation tool** enabling modelling ultrasound wave propagation in a layered medium as well as estimation of the spectrum of the signal backscattered from the medium. This simulation tool, based on the angular spectrum approach, allowed extension of the proposed methodology to a case of 3-D ultrasound wave propagation. The forward propagation model was in excellent agreement with the simulation software Field II, when propagation was modelled in a homogeneous medium (intrinsic limitation of Field II). Moreover, a theoretical framework has been presented for the estimation of the spectrum of a scattered signal detected by the transducer.

- **Validation of the extended approach** and its ability to produce estimates **independent of diffraction**. This validation was performed on data generated in Field II and experimentally acquired phantom data, wherein the proposed approach yielded accurate results for different phantom positions in front of the transducer, i.e. independent of the effects of diffraction.

- **Extension of the angular spectrum approach for a case of a cylindrically-curved array transducer**. The angular spectrum approach (employed in ultrasound simulations) can be readily applied to model fields generated by the transducers with planar geometries. How-

104

ever, its application to predict fields of transducer with curved apertures requires additional procedures. Therefore, an algorithm was developed to compute the angular spectrum of a cylindrically curved array transducer, as often used in clinics to improve the elevation focusing. The proposed extension was validated through comparison with Field II and yielded excellent agreement between the simulators.

- **Validation of the proposed approach on linear array data** acquired in phantoms and in-vivo. The proposed approach was validated on synthetic and experimental phantom data, that were acquired using an array transducer. Furthermore, an improved scattering model was introduced to perform in-vivo validation. Once again, the proposed approach provided accurate attenuation estimates in phantoms, that were independent of the system focal settings. Moreover, the attenuation estimates obtained in liver in-vivo were in a good agreement with the previously reported values for healthy subjects.

In conclusion, this work demonstrates the applicability of the proposed model-based approach in the field of ultrasound tissue characterization and its ability to provide accurate attenuation estimates in various settings. The conducted studies demonstrate how by gradually increasing the complexity of the underlying model, the proposed method can be adapted for more realistic applications. Furthermore, the ultrasound simulation tool developed in the scope of this thesis can be used for other applications than tissue characterization, e.g. prediction of the pressure fields of ultrasound transducers, while the considered approach can certainly be extended for the estimation of the parameters describing other than attenuation acoustic phenomena.

7.2 Future perspectives

The developed algorithm for attenuation estimation has already been tested extensively at increasing level of complexity of the considered problem. However, a more thorough in-vivo validation is highly desirable. Namely, it would be interesting to investigate the ability of the described approach to differentiate between healthy and diseased liver tissue. For this purpose, the attenuation estimates could be obtained in patients with liver steatosis or cirrhosis and compared with the estimates that were already obtained for healthy subjects. Previous studies showed that these pathologies are associated with increased tissue attenuation, which also depends on the pathological grade [14]. The applicability of the proposed approach for early disease diagnosis (i.e. low grade of the pathology) should also be investigated. Furthermore, characterization of other soft tissue organs would be of a great interest. The most straightforward seems the transition to the analysis of solid tissue organs in acoustically

accessible parts of the body, such as kidney, breast or spleen.

It should be noticed that the accuracy of the proposed method in its current implementation seems sufficient for the diagnosis of these organs pathologies. For example in kidney, Turnbull [16] observed increased by 35% attenuation in patients with renal carcinoma, and an approximately same decrease in the presence of oncocytoma. In breast, Landini [21] measured an increase in attenuation by a factor of 2 for malignant tumours and an increase by a factor of 3 in the presence of fibrosis. In liver, an increase of attenuation by approximately 30% has been observed in patients with liver steatosis [5, 9, 14]. Recalling that the error of total attenuation estimates did not exceed 15% for the majority of samples in the experimental phantom study, and that the standard deviation of the estimates obtained in the in-vivo study was about 25%, we can presume that the proposed method would be capable of detecting these pathologies. However, when considering more miniature organs (e.g. eye, aorta, myocardium) a reduction in the size of an estimation block will be required. Furthermore, consideration of highly heterogeneous and complex organs, such as myocardium, may be problematic due to violation of the assumptions made during the derivation of the scattering equation.

In the in-vivo liver study, we could observe an apparent frequency dependence of the backscatter power spectrum on the effective scatterer radius introduce in the model (which was expected from the theoretical considerations [89]). Therefore, we believe that the effective scatterer radius can be estimated simultaneously with the attenuation coefficient using the proposed approach in its current form. Other scattering properties of the tissue such as acoustic concentration and backscatter coefficient can also be potentially estimated. However, some modifications of the reconstruction algorithm and specifically, of the similarity measure, would be required for this purpose. While currently, for simplicity, a least squares estimation was used in combination with an exhaustive search, for the simultaneous estimation of several acoustic parameters, an optimization scheme is preferable. To investigate this point, a small simulation study was performed that is described in App. C. Finally, tissue pathology is often associated with increased concentration of fat, which results in more apparent effect of nonlinearity. Therefore, incorporation of nonlinear effects in the propagation model and consequent estimation of the nonlinear parameter would certainly be of a great interest. In the scope of this thesis, linear wave propagation was considered to avoid the computational burden introduced when modeling of nonlinear effects. However, the possibility of extending the angular spectrum approach to model nonlinear wave propagation has been previously discussed in the literature [79–81] and is therefore conceptually highly feasible.

Speaking of the computation time, it should be noted that the attenuation reconstruction technique, currently implemented in MATLAB (The MathWorks Inc., Natick, MA), is relatively slow. It takes roughly 1.5 hours to estimate the

attenuation coefficient of a sample under the conditions described in chapters 4 and 6. Significant reduction in computation time could be achieved by further parallelizing the reconstruction algorithm and improving the optimization method. Moreover, the angular spectrum method is particularly well suited for computation on a graphic processing unit (GPU) [103]. Reduction in computation time is critical from the point of view of translating the proposed methodology into commercial systems.

Another important aspect that should be discussed concerns the resolution of the reconstruction method. The ultimate goal of quantitative ultrasound methods is to provide the additional quantitative information in a form of a color-coded parametric image overlaid on the conventional B-mode image. However, the resolution of quantitative methods is limited by the size of the spectrum estimation block and the size of the ROI required for obtaining realistic parametric estimates. In the proposed method, a ROI of about 40 mm × 10 mm was used for attenuation reconstruction, wherein the attenuation estimates obtained in small overlapping blocks of 4 mm × 10 mm were averaged along the depth of the ROI. In chapter 2, we demonstrated that the reduction of the lateral ROI size does not significantly hamper the performance of the proposed method up to a certain limit. However, the reduction of the axial ROI size remains challenging, since the majority of the acoustic effects are cumulative in nature and therefore, become more apparent after a certain propagation path.

Finally, throughout this thesis reference acoustic characteristics of various media were taken from literature when modelling propagation in heterogeneous (layered) media. However, some of these parameters could potentially be deduced from analysis of the RF signals. Specifically, the thickness of different tissue layers could be determined from strong reflections in RF signals assuming a certain speed of sound in those tissues or vice versa. The attenuation coefficient could be estimated in every tissue layer, unless the necessary for the estimation block size exceeds the layer thickness. However, the scattering properties cannot be altered throughout the layers, which can be considered a limitation of the proposed approach.

Appendices

Appendix A

Plane - wave propagation

For a plane wave travelling in the z-direction, the particle velocity and pressure are related by a simple expression:

$$p(z, \omega) = c\rho v(z, \omega), \tag{A.1}$$

and the normal velocity to pressure conversion reduces to a multiplication with a constant factor. Moreover, since the plane wave propagates in the direction z, k_z reduces to k, and the transmit and receive transfer functions in Eq. 4.4 of the chapter 4 can be rewritten as:

$$H_{Tx/Rx}(z, \omega) = A_{Tx/Rx}(\omega) H_{Prop}^{p \to p}(z, \omega) H_{Att}^{p \to p}(z, \omega), \tag{A.2}$$

where the propagation and attenuation sub-functions are defined as:

$$H_{Prop}^{p \to p}(z, \omega) = e^{jzk}, \tag{A.3}$$

$$H_{Att}^{p \to p}(z, \omega) = e^{-\alpha \omega z / 2\pi}, \tag{A.4}$$

and the pressure transmission coefficient at the interface between the layers takes the following form:

$$T_{i|i+1}^{p \to p} = \frac{2Z_{i+1}}{Z_i + Z_{i+1}}. \tag{A.5}$$

The rest of the procedure for the estimation of the spectrum of the received signal remains unchanged.

Appendix B

Reflector - based transducer calibration

The input spectrum $S_{Tx,Rx}(\omega)$ specified in Eq. 4.3 of the chapter 4 can be experimentally determined through a single measurement procedure. For this purpose, reflections of the transmitted signal from a planar reflector, submerged in water and positioned perpendicularly to the transducer beam axis have to be recorded. In such a setup, the spectrum of the reflected signal detected by the transducer can be expressed as:

$$S_{Rx}(z,\omega) = j\omega\rho S_{Tx,Rx} \iint_T h_{Tx,Rx}(x,y,z:\omega)dxdy, \qquad (B.1)$$

where the integration can equally be performed in the spatial-frequency domain (using the Parseval equality):

$$S_{Rx}(z,\omega) = j\omega\rho S_{Tx,Rx} \iint H_{Tx,Rx}(k_x,k_y,z:\omega)dk_x dk_y, \qquad (B.2)$$

Here, $H_{Tx,Rx}$ is the transfer function which models the forward and backward wave propagation in water between the transducer and the reflector and which accounts for the effects of diffraction, attenuation, reflection as well as for the transducer geometry and focusing factors:

$$\begin{aligned} H_{Tx,Rx}(k_x,k_y,z:\omega) &= A_{Tx}(k_x,k_y:\omega)H_{Diffr}^{v_n\to\varphi}(k_x,k_y,2z:\omega)\times \\ &\times H_{Att}^{p\to p}(k_x,k_y,2z:\omega)R_{w|r}^{p\to p}(k_x,k_y:\omega)A_{Rx}(k_x,k_y:\omega), \end{aligned} \qquad (B.3)$$

In Eq. B.3, $R_{w|r}^{p\to p}$ is the reflection coefficient for the pressure at normal incidence on the interface "water-reflector", which is given by::

$$R_{w|r}^{p\to p} = T_{w|r}^{p\to p} - 1 = \frac{Z_r - Z_w}{Z_r + Z_w}. \tag{B.4}$$

The reflection measurements for the present study were performed in distilled water at 22 °C using the same electrical excitation as in the phantom experiments. A 10 mm thick acrylic glass (PMMA) plate was used as a reflector. The water tank used in this experiment had a number of slots for accurate positioning of the reflecting plate at different depths from the transducer, equally spaced at 20 mm. In this way, 15 reflections from different depths were recorded and the signals were primarily used to estimate the speed of sound in water by fitting the arrival times of the reflections recorded at different depths. The estimated speed of sound was $c_w = 1485 m/s$ Other acoustic characteristics of distilled water and of the PMMA plastic required for the simulations were taken from the literature: $\rho_w = 1000 kg/m^3, \alpha_w = 0.0022 dB/(cm \cdot MHz), c_r = 2750 m/s, \rho_r = 1192 kg/m^3$.

Next, the transfer function in Eq. B.2 was calculated at every measurement depth. Finally, the amplitude and phase of the input spectrum were determined using a least squares fitting of the simulated received spectrum to the measured one in time-domain.

Appendix C

Simultaneous estimation of the speed of sound and attenuation coefficient

A short simulation study was performed with Field II to study the feasibility of the simultaneous determination of several acoustic parameters with the proposed method. For this purpose, three simulated data sets described in chapter 6 were used. These data sets were generated in Field II for three different attenuation coefficients (0.3, 0.5 and 0.7 dB/cm/MHz) using an array transducer model with the characteristics listed in Table 6.1. The speed of sound in the medium was set to 1540 m/s, the focal position was set at the depth of 50 mm in front of the transducer. Each data set contained 50 RF lines, and the power spectra of the signals were determined according to Eq. 6.6.

The procedure for the attenuation coefficient estimation remained the same as outlined in chapter 6. However, now the input speed of sound in the simulations was varied together with the input attenuation coefficient, and the exhaustive search was performed over two variables. As previously, the input attenuation coefficient was varied in the interval $[0 : 0.5 : 2]$ dB/cm/MHz, while the interval for the speed of sound variation was defined as $[1450:10:1650]$ m/s. The power spectrum in the simulations was determined using Eq. 6.1 with $F(\omega) = 1$ under the assumption of Rayleigh scattering. Both the attenuation coefficient and the speed of sound were estimated by comparing the simulated power spectra with those obtained for the generated data sets using the distance measure given by:
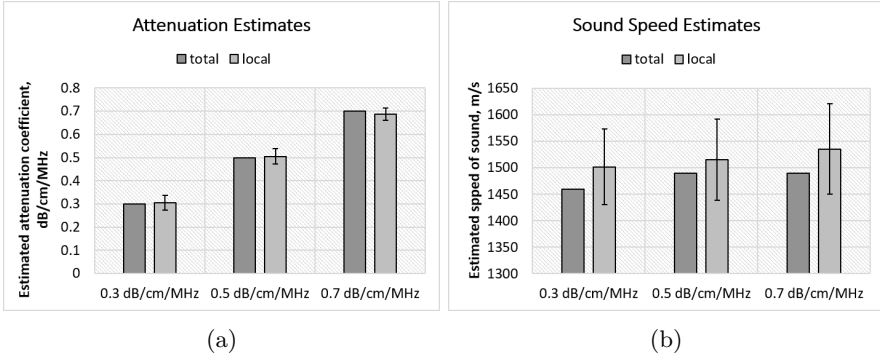
Figure C.1: *Total and averaged local estimates of the attenuation coefficient (a) and the speed of sound (b) which were obtained simultaneously in the simulation study based on three data sets with attenuation coefficients equal to 0.3, 0.5 and 0.7 dB/cm/MHz acquired in the focal zone of the transducer.*

$$D(z, [\alpha, c]) = \sum_{\omega} \left(\sqrt{\mathcal{P}_{meas}(z, \omega)} - \sqrt{\mathcal{P}_{sim}(z, \omega; [\alpha, c])} \right)^2, \qquad \text{(C.1)}$$

whereupon the total estimates of the acoustic parameters were determined as:

$$[\bar{\alpha}, \bar{c}] = \arg\min_{\alpha, c} \left(\sum_{i=2}^{L} D(z_i, [\alpha, c]) \right), \qquad \text{(C.2)}$$

where L was equal 39, while the local estimates of both parameters were obtained using a modified expression:

$$[\alpha(z), c(z)] = \arg\min_{\alpha, c} \left(D(z, [\alpha, c]) \right). \qquad \text{(C.3)}$$

Fig. C.1 presents the estimated total and averaged local values of the attenuation coefficient (a) and sound speed (b). It can be seen, that while the sound speed estimation failed, the estimates of the attenuation coefficient are in excellent agreement with the "ground-truth" values. In Fig. C.2 we can appreciate the uniformity of local attenuation estimates with depth. Finally, Fig. C.3 presents the 2-D maps of the spectral distance $D(z, [\alpha, c])$ for varying attenuation and sound speed values. It can be noticed that the optimization process was driven by the attenuation coefficient, while the speed of sound did not have considerable impact on the distance function. Indeed, the considered
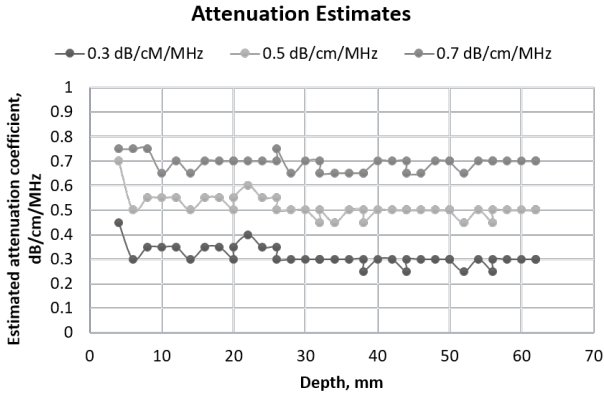
Figure C.2: *Local attenuation results in the simulation study when the speed of sound was varied. The estimates were obtained at different depths for three data sets with attenuation coefficients equal to 0.3, 0.5 and 0.7 dB/cm/MHz generated in focal zone of the transducer.*

variations in the speed of sound do not cause apparent changes in the spectral shape. This conclusion suggests that the accuracy of the attenuation estimation algorithm would not be strongly affected by some small deviations of the input speed of sound in the simulations from its true value. However, in the future, it would be interesting to investigate the feasibility of estimating the attenuation coefficient in a combination with other acoustic parameters, which we expect to have more effect on the spectral shape (e.g. scatterer size). Since Field II is limited to a point scatterer model, other simulation tools or proper test objects would be required for such analysis.
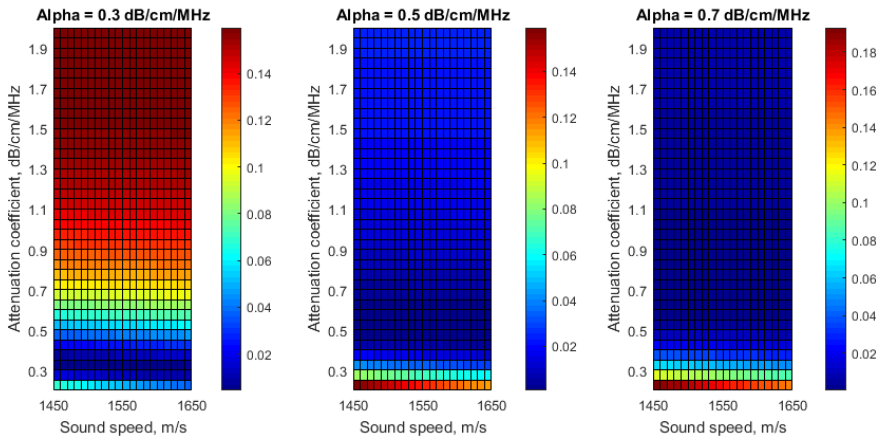
Figure C.3: *Maps of spectral distance values computed in the simulation study for three data sets with attenuation coefficients equal to 0.3, 0.5 and 0.7 dB/cm/MHz generated in the focal zone of the transducer. The maps were computed by simultaneously varying the input attenuation coefficient and the speed of sound values in the simulation.*

Bibliography

[1] K. Kirk Shung and G. A. Thieme. *Ultrasound scattering in biological tissue.* CRC Press, USA, 1992.

[2] L. Tong. *Novel beam forming methods for fast cardiac imaging using ultrasound.* PhD thesis, 2013.

[3] C. M. Seghal, G. M. Brown, R. C. Bahn, and J. F. Greenleaf. Measurement and use of acoustic nonlinearity and sound speed to estimate composition of excised livers. *Ultrasound Med. Biol.*, 12(11):865–874, 1986.

[4] H. Hachiya, O. Shigeo, and M. Tanaka. Relationship Between Speed of Sound in and Density of Normal and Diseased Rat Livers. *Jpn. J. Phys.*, 33:3130–3133, 1994.

[5] Y. Fujii, N. Taniguchi, K. Itoh, K. Shigeta, Y. Wang, J. Tsao, K. Kumasaki, and T. Itoh. A new method for attenuation coefficient measurement in the liver. Comparison with the spectral shift central frequency methods. *J. Ultrasound Med.*, 21:783–788, 2002.

[6] G. Ghoshal, R. J. Lavarello, J. P. Kemmerer, R. J. Miller, and M. L. Oelze. Ex-vivo study of quantitative ultrasound parameters in fatty rabbit livers. *Ultrasound Med. Biol.*, 38(12):2238–2248, 2012.

[7] P. A. Narayana and J. Ophir. On the frequency dependence of attenuation in normal and fatty liver. *IEEE Trans. Son. Ultrason.*, 30:379–383, 1983.

[8] N. F. Maklad, J. Ophir, and V. Balsara. Attenuation of ultrasound in normal liver and diffuse liver disease in vivo. *Ultrason. Imag.*, 6:117–125, 1984.

[9] L. S. Wilson, D. E. Robinson, K. A. Griffiths, A. Manoharan, and B. D. Doust. Evaluation of ultrasonic attenuation in diffuse diseases of spleen and liver. *Ultrason. Imag.*, 9:236–247, 1987.

[10] M. Afschrift, C. Cuvelier, S. Ringoir, and F. Barbier. Influence of patho-logical state on the acoustic attenuation coefficient slope of liver. *Ultra-sound Med. & Biol.*, 13(3):135–139, 1987.

[11] D. L. King, F. L. Lizzi, E. J. Feleppa, P. M. Wai, M. M. Yaremko, M. C. Rorke, and J. Herbst. Focal and diffuse liver disease studied by quantitative microstructural sonography. *Radiology*, 155(2), 1985.

[12] T. Lin, J. Ophir, and G. Potter. Correlation of ultrasonic attenuation with pathologic fat and fibrosis in liver disease. *Ultrasound Med. Biol.*, 14(8):729–734, 1988.

[13] Z. F. Lu, J. A. Zagzebski, and F. T. Lee. Ultrasound backscatter and attenuation in human liver with diffuse disease. *Ultrasound Med. Biol.*, 25(7):1047–1054, 1999.

[14] M. Sasso, M. Beaugrand, V. de Ledinghen, C. Douvin, P. Marcellin, R. Poupon, L. Sandrin, and V. Miette. Controlled attenuation param-eter (CAP): a novel VCTE guided ultrasonic attenuation measurement for the evaluation of hepatic steatosis: preliminary study and validation in a cohort of patients with chronic liver disease from various causes. *Ultrasound Med. Biol.*, 36(11):1825–1835, 2010.

[15] D. Zhang and X. F. Gong. Experimental investigation of the acous-tic nonlinearity parameter tomography for excised pathological biological tissues. *Ultrasound Med. Biol.*, 25(4):593–599, 1999.

[16] D. H. Turnbull, S. R. Wilson, A. L. Hine, and F. S. Foster. Ultra-sonic characterization of selected renal tissues. *Ultrasound Med. Biol.*, 15(3):241–253, 1989.

[17] B. S. Garra, M. F. Insana, I. A. Sesterhenn, T. J. Hall, R. F. Wagner, C. Rotellar, J. Winchester, and R. K. Zeman. Quantitative ultrasonic detection of parenchymal structural change in diffuse renal disease. *In-vestigat. Radiol.*, 29(2), 1994.

[18] S. A. Johnson, T. Abbott, R. Bell, M. Berggren, D. Borup, D. Robinson, J. Wiskin, S. Olsen, and B. Hanover. Non-invasive breast tissue char-acteriation using ultrasound speed and attenuation. In vivo validation. *Acoust. Imag.*, 28:147–154, 2007.

[19] C. Li, N. Duric, L. Peter, and L. Huang. In vivo breast sound-speed imag-ing with ultrasound tomography. *Ultrasound Med. Biol.*, 35(10):1615–1628, 2009.

[20] F. T. D'Astous and F. S. Foster. Frequency dependence of ultrasound attenuation and backscatter in breast tissue. *Ultrasound Med. Biol.*, 12(10):795–808, 1986.

[21] L. Landini and R. Sarnelli. Evaluation of the attenuation coefficients in normal and pathological breast tissue. *Med. Biol. Eng. Comput.*, 24:243–247, 1986.

[22] L. Landini, R. Sarnetti, M. Salvadori, and F. Squartini. Orientation and frequency dependence of backscatter coefficient in normal and pathological breast tissues. *Ultrasound Med. Biol.Biol.*, 13(2):77–83, 1987.

[23] M. L. Oelze and J. F. Zachary. Examination of cancer in mouse models using quantitative ultrasound. *Ultrasound Med. Biol.*, 32(11):1639–1648, 2006.

[24] H. Masugata, K. Mizushige, S. Senda, A. Kinoshita, H. Sakamoto, S. Sakamoto, and H. Matsuo. Relationship between myocardial tissue density measured by microgravimetry and sound speed measured by acoustic microscopy. *Ultrasound Med. Biol.*, 25(9):1459–1463, 1999.

[25] Y. Saijo, M. Tanaka, H. Okawai, H. Sasaki, S. Nitta, and F. Dunn. Ultrasonic tissue characterization of infarcted myocardium by scanningacoustic microscopy. *Ultrasound Med. Biol.*, 23(1):77–85, 1997.

[26] Y. Saijo, E. S. Filho, H. Sasaki, T. Yambe, M. Tanaka, N. Hozumi, K. Kobayashi, and N. Okada. Ultrasonic tissue characterization of atherosclerosis by a speed-of-sound microscanning system. *IEEE Trans. Ultrason. Ferroel. Freq. Contr.*, 54(8):1571–1577, 2007.

[27] J. Namery and P. Lele. Ultrasonic detection of myocardial infarction in dog. In *IEEE Ultrason. Symp.*, pages 491–494, 1972.

[28] J. G. Miller, E. Yuhas, J. W. Mimbs, B. Dierker, L. J. Busse, J J Laterra, A . N. Weiss, and B. E. Sobel. Ultrasonic tissue characterization: correlation between biochemical and ultrasonic indices of myocardial injury. In *Ultrason. Symp.*, pages 33–43, 1976.

[29] J. W. Mimbs, D. E. Yuhas, J. G. Miller, A. N. Weiss, and B. E. Sobel. Detection of myocardial infarction in vitro based on altered attenuation of ultrasound. *Circ. Res.*, 41:192–198, 1977.

[30] R. D. Cohen, J. G. Mollley, J. G. Miller, P. B. Kurnik, and B. E. Sobel. Detection of ischemic myocardium in vivo through the chest wall by quantitative ultrasonic tissue characterization. *Am. J. Cardiol.*, 50(4):838–43, 1982.

[31] M. O'Donnell, J. W. Mimbs, and J. G. Miller. Relationship between collagen and ultrasonic backscatter in myocardial tissue. *J. Acoust. Soc. Am.*, 69(2):580–588, 1981.

[32] Y. Saijo, S. Hidehiko, H. Okawai, S. Nitta, and M. Tanaka. Acoustic properties of atherosclerosis of human aorta obtained with high-frequency ultrasound. *Ultrasound Med. Biol.*, 24(7):1061–1064, 1998.

[33] L. Landini, R. Sarnelli, E. Picano, and M. Salvadori. Evaluation of frequency dependence of backscatter coefficient in normal and atherosclerotic aortic walls. *Ultrasound Med. Biol.*, 12(5):397–401, 1986.

[34] C. Huang, C. Ruimin, P. Tsui, Q. Zhou, M. S. Humayun, and K. Kirk Shung. Measurements of attenuation coefficient for evaluating the hardness of a cataract lens by a high-frequency ultrasonic needle transducer. *Phys. Med. Biol.*, 54:5981–5994, 2009.

[35] H. Tabandeh, M. Wilkins, G. Thompson, D. Nassiri, and A. Karim. Hardness and ultrasonic characteristics of the human crystalline lens. *J. Cataract Refract. Surg.*, 26:838–841, 2000.

[36] E. J. Feleppa, F. L. Lizzi, and M. M. Yaremko. Diagnostic spectrum analysis in ophthalmology: A physical perspective. *Ultrasound Med. Biol.*, 12:623–31, 1986.

[37] J. Mamou, A. Coron, M. Hata, J. Machi, E. Yanagihara, P. Laugier, and E. J. Feleppa. Three-dimensional high-frequency characterization of cancerous lymph nodes. *Ultrasound Med. Biol.*, 36(3):361–375, 2010.

[38] E. J. Feleppa, T. Liu, A. Kalisz, M. C. Shao, N. Fleshner, V. Reuter, and W. R. Fair. Ultrasonic Spectral-Parameter Imaging of the Prostate. *Int. J. Imag. Sys. Tech.*, 8(1):11–25, 1997.

[39] M. Linzer and S. J. Norton. Ultrasonic tissue characterization. *Ann. Rev. Biophys. Bioeng.*, 11:303–329, 1982.

[40] F. L. Lizzi, S. K. Alam, S. Mikaelian, P. Lee, and E. J. Feleppa. On the statistics of ultrasonic spectral parameters. *Ultrasound Med. Biol.*, 32(11):1671–85, 2006.

[41] L. X. Yao, J. A. Zagzebski, and E. L. Madsen. Backscatter coefficient measurements using a reference phantom to extract depth-dependent instrumentation factors. *Ultrason. Imag.*, 12(1):58–70, 1990.

[42] K. Nam, I. M. Rosado-Mendez, N. C. Rubert, E.L. Madsen, J. A. Zagzebski, and T. J. Hall. Ultrasound attenuation measurements using a reference phantom with sound speed mismatch. *Ultrason. Imag.*, 33(2011):251–263, 2011.

[43] D. I. Hughes and F. A. Duck. Automatic attenuation compensation for ultrasonic imaging. *Ultrasound Med. Biol.*, 23(5):651–664, 1997.

[44] G. Treece, R. Prager, and A. Gee. Ultrasound attenuation measurement in the presence of scatterer variation for reduction of shadowing and enhancement. *IEEE Trans. Ultrason. Ferroel. Freq. Contr.*, 52(12):2346–2360, 2005.

[45] V. Roberjot, L. Bridal, P. Laugier, and G. Berger. Absolute backscatter coefficient over a wide range of frequencies in a tissue-mimicking phantom

containing two populations of scatterers. *IEEE Trans. Ultrason. Ferroel. Freq. Contr.*, 43(5):970–978, 1996.

[46] F. Dunn, W. K. Law, and L. A. Frizzell. Nonlinear ultrasonic wave propagation in biological materials. In *Ultrason. Symp.*, pages 527–532, 1981.

[47] F. A. Duck. Nonlinear acoustics in diagnostic ultrasound. *Ultrasound Med. Biol.*, 28(1):1–18, 2002.

[48] P. He and J. F. Greenleaf. Application of stochastic analysis to ultrasonic echoes - Estimation of attenuation and tissue heterogeneity from peaks of echo envelope. *J. Acoust. Soc. Am.*, 79(2):526–534, 1986.

[49] H. S. Jang, T. K. Song, and S. B. Park. Ultrasound attenuation estimation in soft tissue using entropy difference of pulsed echoes between two adjacent envelope segments. *Ultrason. Imag.*, 10:248–264, 1988.

[50] B. S. Knipp, T. A. Zagzebski, T. A. Wilson, F. Dong, and E. L. Madsen. Attenuation and backscatter estimation using video signal analysis applied to B-mode images. *Ultrason. Imag.*, 19:221–233, 1997.

[51] R. Kuc, M. Schwartz, and L. Von Micsky. Parametric estimation of the acoustic attenuation coefficient slope for soft tissue. In *Ultrason. Symp.*, pages 44–47, 1976.

[52] M. Fink, F. Hottier, and J. F. Cardoso. Ultrasonic signal processing for in vivo attenuation measurement: short time Fourier analysis. *Ultrason*, 5(2):117–135, 1983.

[53] T. Baldeweck, P. Laugier, A. Herment, and G. Berger. Application of autoregressive spectral analysis for ultrasound attenuation estimation: interest in highly attenuating medium. *IEEE Trans. Ultrason. Ferroel. Freq. Contr.*, 42(1):99–110, 1995.

[54] H. Kim and T. Varghese. Attenuation estimation using spectral cross-correlation. *IEEE Trans. Ultrason. Ferroel. Freq. Contr.*, 54(3):510–519, 2007.

[55] S. W. Flax, N. J. Pelc, G. H. Glover, F. D. Gutmann, and M. McLachlan. Spectral characterization and attenuation measurements in ultrasound. *Ultrason. Imag.*, 5(2):95–116, 1983.

[56] K. J. Parker and R. C. Waag. Measurement of ultrasonic attenuation within regions selected from B-scan images. *IEEE Trans. Biomed. Eng.*, 30(8):431–437, 1983.

[57] K. J. Parker, M. S. Asztely, R. M. Lerner, E. A. Schenk, and R. C. Waag. In-vivo measurement of ultrasound attenuation in normal or diseased liver. *Ultrasound Med. Biol.*, 14(2):127–136, 1988.

[58] R. Kuc and M. Schwartz. Estimating the acoustic attenuation coefficient slope for liver from reflected ultrasound signals. *IEEE Trans. Son. Ultrason.*, 26(5):353–361, 1979.

[59] R. Kuc. Bounds on estimating the acoustic attenuation of small tissue regions from reflected ultrasound. In *IEEE*, volume 73, pages 1159–1168, 1985.

[60] R. Kuc. Estimating acoustic attenuation from reflected ultrasound signals: Comparison of spectral-shift and spectral-difference approaches. *IEEE Trans. Acoust. Speech Sign. Process.*, 32(1):1–6, 1984.

[61] M. Insana, J. Zagzebski, and E. Madsen. Improvements in the spectral difference method for measuring ultrasonic attenuation. *Ultrason. Imag.*, 5(4):331–345, 1983.

[62] H. Kim and T. Varghese. Hybrid spectral domain method for attenuation slope estimation. *Ultrasound Med. Biol.*, 34(11):1808–1819, 2008.

[63] Yassin Labyed and Timothy A. Bigelow. A theoretical comparison of attenuation measurement techniques from backscattered ultrasound echoes. *J. Acoust. Soc. Am.*, 129(4):2316, 2011.

[64] N. Ilyina, J. Hermans, E. Verboven, K. Van Den Abeele, E. D'Agostino, and J. D'hooge. Iterative reconstruction of the ultrasound attenuation coefficient from the backscattered radio-frequency signal. In *EEE Ultrason. Symp.*, pages 2406–2409, 2014.

[65] B. J. Oosterveld, J. M. Thijssen, P. C. Hartman, R. L. Romijn, and G. J. E. Rosenbusch. Ultrasound attenuation and texture analysis of diffuse liver disease: methods and preliminary results. *Phys. Med. Biol.*, 36(8):1039–1064, 1991.

[66] E. L. Madsen, J. A. Zagzebski, R. A. Banjavic, and R. E. Jutila. Tissue mimicking materials for ultrasound phantoms. *Med. Phys.*, 5(5):391–394, 1978.

[67] M. M. Burlew, E. L. Madsen, J. A. Zagzebski, R. A. Banjavic, and S. W. Sum. A new ultrasound tissue-equivalent material. *Radiology*, 194:517–520, 1980.

[68] A. Kharine, S. Manohar, R. Seeton, R. G. M. Kolkman, R. A. Bolt, W. Steenbergen, and F. F. M. de Mul. Poly (vinyl alcohol) gels for use as tissue phantoms in photoacoustic mammography. *Phys. Med. Biol.*, 48:357–370, 2003.

[69] M. F. Hamilton and D. T. Blackstock. *Nonlinear acoustics*. Academic Press, San Diego, California, 1998.

[70] J. Tavakkoli, D. Cathignol, R. Souchon, and O. A. Sapozhnikov. Modeling of pulsed finite-amplitude focused sound beams in time domain. *J. Acoust. Soc. Am.*, 104(4):2061–2072, 1998.

[71] R. S. C. Cobbold. *Foundations of biomedical ultrasound*. Oxford University Press, USA, 2006.

[72] Y. Labyed and T. A. Bigelow. Estimating the total ultrasound attenuation along the path by using a reference phantom. *J. Acoust. Soc. Am.*, 128(5):3232–3238, 2010.

[73] P. Welch. The use of fast Fourier transform for the estimation of power spectra: A method based on time averaging over short, modified periodograms. *IEEE Trans. Aud. Electroacoust.*, 15(2):70–73, 1967.

[74] M. K. Hasan, M. A. Hussain, S. R. Ara, S. Y. Lee, and S .K. Alam. Using nearest neighbors for accurate estimation of ultrasonic attenuation in the spectral domain. *IEEE Trans. Ultrason. Ferroel. Freq. Contr.*, 60(6):1098–114, 2013.

[75] P. M. Morse and K. U. Ingard. *Theoretical acoustics*. Princeton University Press, Princetin, New Jersey, 1968.

[76] N. V. Sushilov, J. Tavakkoli, and R. S. C. Cobbold. Propagation of limited-diffraction X-waves in dissipative media. *IEEE Trans. Ultrason. Ferroel. Freq. Contr.*, 49(6):675–682, 2002.

[77] P. Stepanishen, M. Forbed, and S. Letcher. The relationship between the impulse response and angular spectrum method to evaluate acoustic transient fileds. *J. Acoust. Soc. Am.*, 90(5):2794–2798, 1991.

[78] P. T. Christopher and K. J. Parker. New approaches to the linear propagation of acoustic fields. *J. Acoust. Soc. Am.*, 90(1):507–521, 1991.

[79] P. T. Christopher and K. J. Parker. New approaches to nonlinear diffractive field propagation. *J. Acoust. Soc. Am.*, 90(1):488–499, 1991.

[80] R. J. Zemp, J. Tavakkoli, and R. S. C. Cobbold. Modeling of nonlinear ultrasound propagation in tissue from array transducers. *J. Acoust. Soc. Am.*, 113(1):139–152, 2003.

[81] F. Varray, A. Ramalli, C. Cachard, P. Tortoli, and O. Basset. Fundamental and second-harmonic ultrasound field computation of inhomogeneous nonlinear medium with a generalized angular spectrum method. *IEEE Trans. Ultrason. Ferroel. Freq. Contr.*, 58(7):1366–1376, 2011.

[82] W. J. Goodman. *Introduction to Fourier optics*. McGraw-Hill, New York, 1968.

[83] U. Vyas and D. A. Christensen. Extension of the angular spectrum method to calculate pressure from a spherically curved acoustic source. *J. Acoust. Soc. Am.*, 130(5):2687, 2011.

[84] P. Wu, R. Kazys, and T. Stepinski. Optimal selection of parameters for the angular spectrum approach to numerically evaluate acoustic fields. *J. Acoust. Soc. Am.*, 101(1):125–134, 1996.

[85] X. Zeng and R. J. McGough. Evaluation of the angular spectrum approach for simulations of near-field pressures. *J. Acoust. Soc. Am*, 123(1):68–76, 2008.

[86] J. A. Jensen and N. B. Svendsen. Calculation of pressure fields from arbitrarily shaped, apodized, and excited ultrasound transducers. *IEEE Trans. Ultrason. Ferroel. Freq. Contr.*, 39(2):262–267, 1992.

[87] J. A. Jensen, D. Gandhi, and W. D. O'Brien. Ultrasound fields in an attenuating medium. In *Ultrason. Symp.*, pages 943–946, 1993.

[88] M. Ueda and Y. Ozawa. Spectral analysis of echoes for backscattering coefficient measurement. *J. Acoust. Soc. Am.*, 77(1):38–47, 1985.

[89] M. F. Insana, R. F. Wagner, D. G. Brown, and T. J. Hall. Describing small-scale structure in random media using pulse-echo ultrasound. *J. Acoust. Soc. Am.*, 87(1):179–192, 1990.

[90] M. O'Donnell, J. W. Mimbs, and J. G. Miller. The relationship between collagen and ultrasonic attenuation in myocardial tissue. *J. Acoust. Soc. Am.*, 65(2):512–517, 1979.

[91] M. Meziri, W. C. A. Pereira, A. Abdelwahab, C. Degott, and P. Laugier. In vitro chronic hepatic disease characterization with a multiparametric ultrasonic approach. *Ultrasonics*, 43:305–313, 2005.

[92] K. A. Wear, B. S. Garra, and T. J. Hall. Measurements of ultrasonic backscatter coefficients in human liver and kidney in vivo. *J. Acoust. Soc. Am.*, 98(4):1852–1857, 1995.

[93] J. A. Zagzebski, Z. F. Lu, and L. X. Yao. Quantitative ultrasound imaging: in vivo results in normal liver. *Ultrason. Imag.*, 15:335–51, 1993.

[94] E. Omari, H. Lee, and T. Varghese. Theoretical and phantom based investigation of the impact of sound speed and backscatter variations on attenuation slope estimation. *Ultrasonics*, 51:758–767, 2011.

[95] E. S. Ebbini and C. A. Cain. Multiple-focus ultrasound phased-prray pattern synthesis: optimal driving-signal distributions for hyperthermia. *IEEE Trans. Ultrason. Ferroel. Freq. Contr.*, 36(5):540–548, 1989.

[96] Michael L. Oelze, James F. Zachary, and William D. O'Brien, Jr. Characterization of tissue microstructure using ultrasonic backscatter: theory and technique for optimization using a Gaussian form factor. *J. Acoust. Soc. Am.*, 112(3 Pt 1):1202–11, 2002.

[97] J. Mamou, M. L. Oelze, W. D. O'Brien, and J. F. Zachary. Extended three-dimensional impedance map methods for identifying ultrasonic scattering sites. *J. Acoust. Soc. Am.*, 123(2):1195–1208, 2008.

[98] E. Franceschini and R. Guillermin. Experimental assessment of four ultrasound scattering models for characterizing concentrated tissue-mimicking phantoms. *J. Acoust. Soc. Am.*, 132(6):3735–3747, 2012.

[99] A. Ortega, D. Lines, B. Chakraborty, V. Komini, and H. Gassert. HD-PULSE : High channel Density Programmable ULtrasound System based on. In *IEEE Ultrason. Symp.*, pages 31–33, 2015.

[100] T. D. Mast, L. M. Hinkelman, M. J. Orr, V. W. Sparrow, and R. Waag. Simulation of ultrasonic pulse propagation through the abdominal wall. *J. Acoust. Soc. Am.*, 102(2):1177–1190, 1997.

[101] R. Kuc. Clinical application of an ultrasound attenuation coefficient estimation technique for liver pathology characterization. *IEEE Trans. Biomed. Eng.*, 27(6):312–319, 1980.

[102] B. S. Garra, T. H. Shawker, M. Nassi, and M. A. Russel. Ultrasound attenuation measurements of the liver in vivo using a commercial sector scanner. *Ultrason. Imag.*, 6:396–407, 1984.

[103] F. Varray, C. Cachard, A. Ramalli, P. Tortoli, and O. Basset. Simulation of ultrasound nonlinear propagation on GPU using a generalized angular spectrum method. *EURASIP J. Imag. Vid. Process.*, 2011(1):17, 2011.

List of publications

Papers in peer-reviewed journals

N. Ilyina, J. Hermans, E. Verboven, K. Van Den Abeele, E. D'Agostino and J. D'hooge, "Attenuation estimation by repeatedly solving the forward scattering problem", *revision submitted*.

N. Ilyina, J. Hermans, K. Van Den Abeele and J. D'hooge, "Diffraction-independent ultrasound attenuation estimation", *submitted*.

N. Ilyina, J. Hermans, K. Van Den Abeele, and J. D'hooge, "Extension of the angular spectrum method to model the pressure field of a cylindrically curved array transducer." *J. Acoust. Soc. Am.*, 141(3):262-266, 2017.

K. Fuzesi, **N. Ilyina**, E. Verboven, K. Van Den Abeele, M. Gyongy and J. D'hooge, "Temperature dependence of speed of sound and attenuation of porcine left ventricular myocardium", *submitted*.

International conference proceedings

N. Ilyina, J. Hermans, E. Verboven, K. Van Den Abeele, E. D'Agostino and J. D'hooge, " Iterative reconstruction of the ultrasound attenuation coefficient from the backscattered radio-frequency signal", *IEEE Ultrasonics Symp.*, 2014, pp.2406-2409.

Abstracts at international conferences

N. Ilyina, J. Hermans, E. Verboven, K. Van Den Abeele, E. D'Agostino and J. D'hooge, "Iterative reconstruction of the ultrasound attenuation coefficient from backscattered signals", *J. Acoust.Soc. Am.*, 137(4):2424, 2015.

N. Ilyina, J. Hermans, E. Verboven, K. Van Den Abeele, E. D'Agostino and J. D'hooge, "Diffraction independent estimation of the ultrasound attenuation coefficient", *IEEE Ultrasonics Symp.*, 2015.

N. Ilyina and J. D'hooge, "Model-based ultrasound attenuation estimation algorithm", *J. Acoust.Soc. Am.*, 141:3956, 2017.

FACULTY OF MEDICINE
DEPARTMENT OF CARDIOVASCULAR SCIENCES
CARDIOVASCULAR IMAGING AND DYNAMICS
Herestraat 49 box 7003 50
B-3000 LEUVEN, BELGIUM
natalia.ilyina@kuleuven.be